Summer 8-15-2018

An NMR Study of CO2 Dynamics and Structural Characterization of Porous Materials

Robert M. Marti
Washington University in St. Louis

WASHINGTON UNIVERSITY IN ST. LOUIS

Department of Chemistry

Dissertation Examination Committee:
Sophia E. Hayes, Chair
Richard Axelbaum
Alexander Barnes
Julio D'Arcy
Erik Henriksen

An NMR Study of CO_2 Dynamics and Structural Characterization of Porous Materials

by
Robert M. Marti

A dissertation presented to
The Graduate School
of Washington University in
partial fulfillment of the
requirements for the degree
of Doctor of Philosophy

August 2018
Saint Louis, Missouri

Table of Contents

List of Figures

List of Tables

Acknowledgments

There are many people who have helped me get to this point in my life, and it has definitely been a journey. I went from being a child who almost flunked Kindergarten and not being able to read until the 1st grade to a man capable of becoming a Doctor of Philosophy in Chemistry. I will forever be in debt to my 1st grade teacher who pulled me out of class every day to teach me how to read at Robert Frost Elementary School. Without her, I would not have developed an essential tool that enabled me to go further than I had ever imagined. Words cannot aptly describe my gratitude for her patience and her belief in me.

Of course, without the support of my family and friends, I would not have been able to make it through the times where I struggled, and I would not have been able to enjoy the good times where we celebrated the small victories. My wife, Whitney, has been a tremendous help to push me forward and keep me going through thick and thin. She cared for me when I felt like I there was no time to care for myself. I would truly be lost without her. My mom, dad, and brother have always been very supportive in my pursuit of higher education, and that constant support has always been a driving force for me to strive for more in life.

Throughout high school and still to this day, I have had many people who help guide me to the life I wanted. However, two people in particular changed my life, Ginny Quincy and Justin Greenfield. Ginny always believed in me, which was exceptionally important when she encouraged me to switch schools between my sophomore and junior years of high school. This change challenged me academically, but ultimately prepared me to be a person who learned how to learn. This is also how I met Justin, who taught me many different life skills and how to get out of my shell. I had no idea how important it was to effectively communicate until I met Justin.

Without the guidance and support from Prof. Sophia E. Hayes, this would not have been possible. Sophia sent me all over the world, visiting different labs and learning different “tricks of the trade.” Sophia has been instrumental in my development as not only a scientist, but also as a person. I’ve also had the great opportunity to learn and have different discussions about science with my coworkers. I really enjoyed the time I spend with Erika while building a new gas manifold for a flow-through system and learning about using Swaglok. Blake started me on my NMR path, teaching me the ways of quadrupolar nuclei and how to carefully setup experiments. Chia-Hsin was an absolute amazing co-worker to work with. We both entered the lab in 2014 and got to grow together. I could always count on Chia-Hsin to do anything and she made my life in lab much easier. Zayd was helpful in every way imaginable and having the perspective from a physicist was good food for thought. Zayd was a fantastic teacher, especially when it came to electronics and I will always appreciate the times we worked together. Daphna Shimon entered the lab during the middle of my graduate career and was always willing to lend a helping hand or discuss intellectual ideas related to my research. I owe many thanks to other members of the lab, both past and present, Dustin Wheeler, Katie Wentz, Matt Willmering, Michael “Ike” West, Jinlei Cui, Yvonne Afiyie, He “Jason” Sun. In starting my Sam, Hongyang, Conradi.)

Collaborators (Colton and Jay, Josh, Cody, Sholl, Walton)

I would also like to thank the national labs that enabled us to pursue science that we would not have been able to do otherwise. My first two visits to a national lab were at the Pacific Northwest National Laboratory (PNNL) and we worked in the Environmental Molecular Sciences Laboratory (EMSL) user facility in Richland, WA. We were allotted time on a high and low field magnet to work on two separate problems, and we really appreciate the time there. There were also a number of really interesting sights, such as the decommissioned U.S. Navy nuclear

submarine, *Triton*. I also had the chance to visit the National High Magnetic Field Laboratory in Tallahassee, FL where I had an opportunity to take a measurement on the 1.5 GHz series-connected hybrid (SCH) magnet. I even had an opportunity to travel to France twice to work on some projects. I was able to perform some work in both Lyon and Orléans while in France, where I learned some important experimental details for quadrupolar nuclei. In Lyon, I was able to work on the 400 MHz DNP setup and got to see in person, the 1 GHz magnet they have in the facility. In Orléans I had an opportunity to work on a couple of different magnets and perform special 2-dimensional experiments that significantly contributed to my Ph. D. work. Financial support from the TGIR-RMN-THC Fr3050 CNRS for conducting quantitative 1D, HMQC, and MQ-MAS experiments is also gratefully acknowledged. Also, while in Orléans, I was able to see the Jeanne d'Arc (Joan of Arc) statue, which was an incredibly beautiful site to see.

Lastly, I must acknowledge the agency which provided my financial support to conduct the research for these projects. This work was supported as a part of the Center for Understanding and Control of Acid Gas-Induced Evolution of Materials for Energy (UNCAGE-ME), an Energy Frontier Research Center funded by the U.S. Department of Energy, Office of Science, Basic Energy Sciences under Award No. DE-SC0012577.

Robert M. Marti

Washington University in St. Louis

August 2018

Dedicated to the pursuit of knowledge.

ABSTRACT OF THE DISSERTATION

An NMR Study of CO_2 Dynamics and Structural Characterization of Porous Materials

by

Robert M. Marti

Doctor of Philosophy in Inorganic Chemistry

Washington University in St. Louis, 2018

Professor Sophia E. Hayes, Chair

Nuclear magnetic resonance (NMR) has proven to be a versatile and powerful analytical tool to study many areas of interest to the scientific community, such as molecular dynamics and structural characterization. In this dissertation, NMR was used as a probe for CO_2 dynamics in metal-organic frameworks. Variable temperature (VT) NMR was used to determine molecular dynamics of CO_2, going as low as 8 K. In the fast motion regime, where the CO_2 hopping rate is fast compared to the NMR experiment time, $^{13}CO_2$ inside of Mg-MOF-74 still exhibits a chemical shift anisotropy (CSA) powder pattern. However, there is a certain loading of CO_2 inside the framework (~ 1 CO_2 molecule per 1 open metal site) the results in a symmetric Gaussian lineshape where it *appears* that the CSA is motionally averaged. This is not the case though, the CO_2 molecules adopt an *average* orientation inside the channels of the framework as a function of CO_2 loading. This average orientation manifests itself in the CSA lineshape and can be explained using the Legendre polynomial, P_2.

Additionally, ^{27}Al magic-angle spinning (MAS) NMR was performed to characterize aluminum carbide (Al_4C_3) and its related derivatives. Multiple-quantum magic-angle spinning of Al_4C_3 revealed accurate values for the quadrupolar tensor, and elucidated the presence of additional sites likely to be from an oxycarbide unit ($Al_4(C,O)_3$). Extracting accurate values for the

quadrupolar tensor was critical in the understanding and deconvolution of MIL-53(Al) derived from aluminum carbide. ^{27}Al NMR is uniquely qualified to identify the presence of [4]-, [5]-, and [6]-coordinate amorphous aluminum oxide species that would otherwise be unseen in techniques such as powder X-ray diffraction (PXRD). The formation of this aluminum oxide layer appears to be a necessary step to the formation of MIL-53(Al).

Chapter 1: Introduction to Greenhouse Gases, CO_2 Adsorption, and NMR

For several decades now, CO_2 capture and sequestration has been a topic of intense study due to its potential impact on the means to remove CO_2 from flue gas. Over 400,000 years ago, the atmospheric concentration of CO_2 fluctuated between 180 and 300 ppm (Figure 1.1 [1]). Since this time, the amount of atmospheric CO_2 globally has increased to approximately 409 ppm

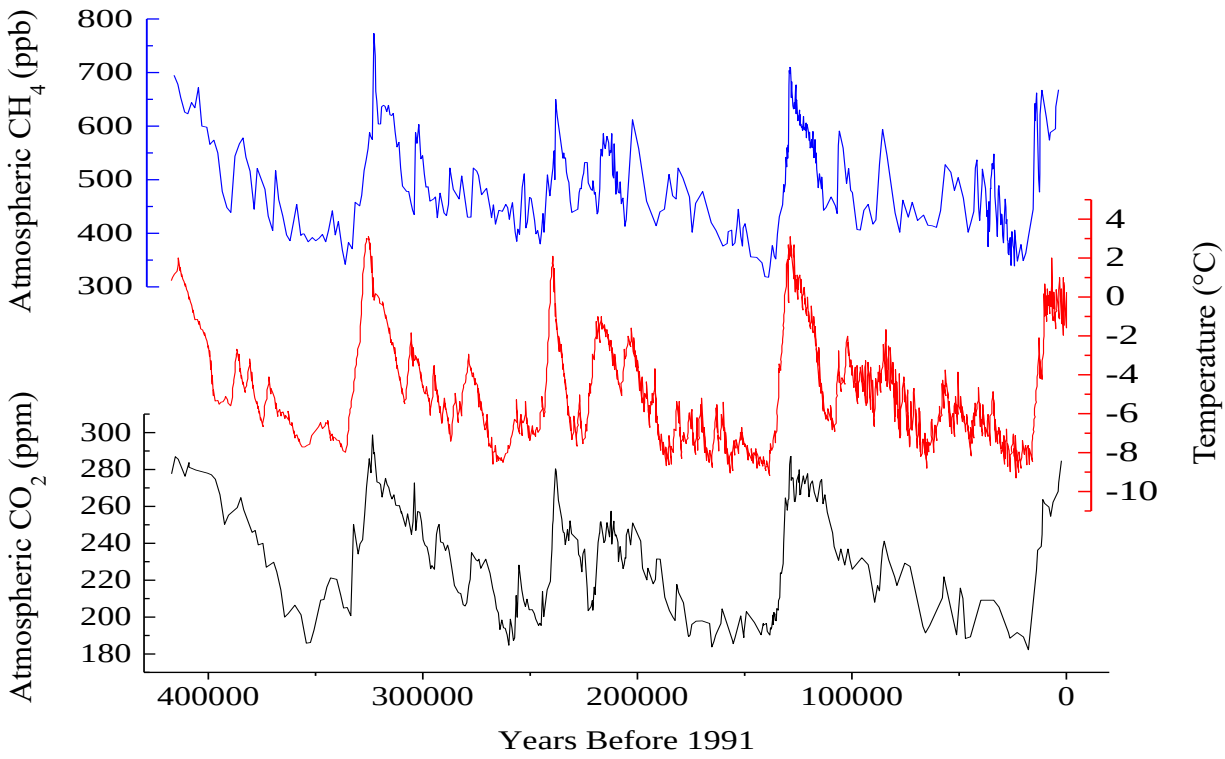

Figure 1.1. Atmospheric concentrations of CH_4 (top, blue curve) and CO_2 (bottom, black curve) from 420,000 years ago until 1991, where 1991 = 0 on the x-axis. The average temperature variation (middle, red curve) is also shown for the past 420,000 years.

according to the Earth System Research Laboratory (ESRL) of the National Oceanic and Atmospheric Administration (NOAA) in March 2018[2]. Multiple studies state that fluctuations in the thermal structure of the atmosphere are not supported by natural variation in the climate

system and attribute increased levels of greenhouse gases to anthropogenic influences[3–8]. The 2013 Intergovernmental Panel on Climate Change (IPCC) report states, “It is *extremely likely* that human influence has been the dominant cause of the observed warming since the mid-20th century[9].” Humans utilize tools/equipment to aid in everyday life activities such as transportation as well as the manufacturing of goods, almost all of which use fuel that produce CO_2 as byproduct when combustion occurs. Thus, the increased use of fossil fuels translates into the increased production of CO_2. Scientists have tried to mitigate and decrease the amount of atmospheric CO_2 by implementing technologies such as liquid- and solid-state adsorbents that preferentially bind CO_2. The liquid-state technologies generally consist of liquid amine solutions or ionic liquids, and solid-state technologies can consist of a variety of materials, such as metal-organic frameworks (MOFs) and activated carbons. The aspiration is to capture CO_2 from large stationary point sources[10], such as a power plant, and subsequently release it in order to sequester it in a way that traps it in the solid state, such as geosequestration[11]. There are numerous ways in which these methods and materials are studied, including NMR spectroscopy.

1.1 Chemisorption

Liquid sorbents, such as monoethanolamine (MEA), have been implemented as a chemisorption technology to adsorb CO_2 at high concentration sources[12]. These types of liquid sorbents have large CO_2 capacities, which make them an attractive solution for CO_2 capture. Chemisorption is a process where an adsorbate interacts with an adsorbent forming a chemical bond between the two species, resulting in a product with a different chemical makeup than the starting materials. In many cases, amines adsorb CO_2 by chemically reacting and forming a number of different species, such as carbamates and bicarbonates[13,14]. However, many of these amine sorbents, such as MEA, have high regeneration costs and, experience chemical degradation and amine

leaching[12]. These drawbacks have fueled the inspiration to make stronger adsorbents with high CO_2 capacities, lower regeneration costs, and more robustness.

1.2 Physisorption

Physisorption is an adsorption process between an adsorbate and an adsorbent, where the adsorption process occurs via a van der Waals interaction. Typically, there exists an electron-poor site on the adsorbent that attracts the electron-rich oxygen on CO_2 through an electrostatic interaction. These types of bonding interactions are weaker than chemisorption interactions, because a chemical bond is not formed. Physisorption interactions of CO_2 have been evident in materials such as ionic liquids[15,16], metal-organic frameworks (MOFs)[17–19], activated carbons[20], and polymers of intrinsic microporosity (PIMs)[21,22] to name just a few examples. Ionic liquids can have high adsorption capacities as well, but can suffer from its viscosity, resulting in slow kinetics because of mass transfer rates[23]. Even though some of these ionic liquids can adsorb large amounts of CO_2, the rate of uptake can be slow.

1.3 NMR Spectroscopy

Magnetic resonance has proven to be an incredibly powerful tool to elucidate chemical structure, dynamics, imaging, and has many other applications. Nuclear magnetic resonance (NMR) is a non-destructive element-specific technique that involves a magnetic field and radio frequency waves/pulses. NMR-active nuclei (nuclear spin quantum number $I \neq 0$) possess spin states that are degenerate in energy when there is no magnetic field. In the presence of a magnetic field, the spin states split into higher and lower energy levels, where the number of energy levels is $(2I + 1)$. For example, a $I = 1/2$ system will split into two energetically different spin states according to the time-independent Hamiltonian, $\mathcal{H}\Psi = E\Psi$. For the purposes of this example, we will

assume that the +1/2 state is lower in energy and that the -1/2 state is higher in energy. For Zeeman energy of the +1/2 state, we have the following:

$$\frac{-\gamma\hbar B_o I_z}{2}\left|+\frac{1}{2}\right\rangle = E_+\left|+\frac{1}{2}\right\rangle, \tag{1.1}$$

where γ is the gyromagnetic ratio of the nucleus, ħ is Plank's constant divided by 2π, B_o is the strength of the external magnetic field, I_z is the operator, and E_+ is the energy of the +1/2 state. After applying the operator, the resulting energy for the +1/2 spin state is $E_+ = -\gamma\hbar B_o/2$. Applying the same operator on the -1/2 spin state results in $E_- = +\gamma\hbar B_o/2$. Thus, the resulting Zeeman energy splitting is,

$$\Delta E = E_- - E_+ = \gamma\hbar B_o, \tag{1.2}$$

where ΔE is the energy difference between the -1/2 and +1/2 states. The effect without and with an external magnetic field on the nuclear spin states is shown in Figure 1.2.

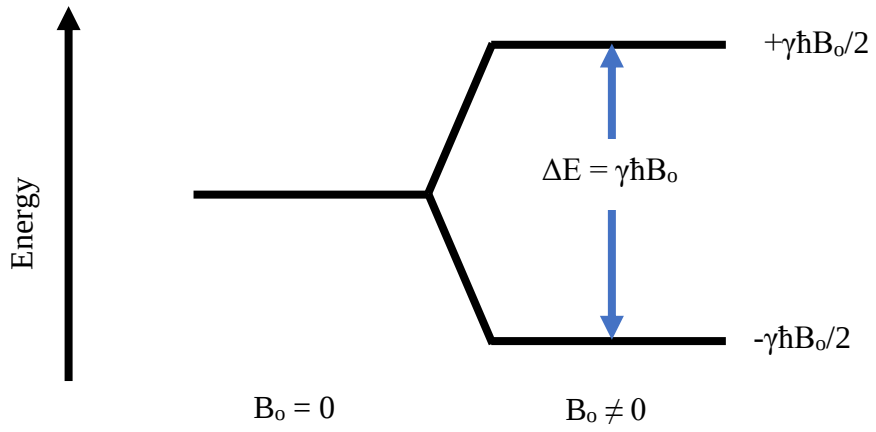

Figure 1.2: Energy level diagram for a spin-½ (I = ½) species in the absence of a magnetic field ($B_o = 0$) and in the presence of a magnetic field ($B_o \neq 0$).

Another aspect related to the energy difference is the sensitivity of the NMR measurement. The sensitivity of the NMR experiment is dictated by the difference in spin populations between the upper and lower state. This relates to polarization, where polarization (P) for a spin-1/2 system is

defined as $P = \frac{n_+ - n_-}{n_+ + n_-}$, where n_+ represents the number of spins in the lower energy state (here, E_+) and n_- represents the number of spins in the upper energy state. Typically, at room temperature and without enhancements from techniques such as dynamic nuclear polarization (DNP), spin polarization is on the order of 10^{-6}. These populations follow Boltzmann statistics, and because the energy difference between the two states is small, the populations are nearly equal. Hence, the resulting polarization is also small. The derivation of polarization uses the following as a premise: $p_+ + p_- = 1$, $p_+ - p_- = \varepsilon$, and the thermal equilibrium ratio $p_-/p_+ = \exp(-\Delta E/kT)$, where p_+ and p_- are the relative number of spins in the lower and upper spin states (the two Zeeman levels), respectively, ΔE is the difference in energy between the two spin states, k is the Boltzmann constant, and T is the temperature[24]. Using these equations, we can show that the difference in relative populations, ε, is equal to $\Delta E/(2kT)$, in the high temperature limit[24]. Using the relationship between the sum and difference of the relative populations we get,

$$p_- = 0.5 - \frac{\varepsilon}{2} \text{ and } p_+ = 0.5 + \frac{\varepsilon}{2}. \tag{1.3}$$

Substituting Eqs. 1.3 into the thermal equilibrium ratio yields the following,

$$\frac{0.5-\frac{\varepsilon}{2}}{0.5+\frac{\varepsilon}{2}} = \frac{0.5(1-\varepsilon)}{0.5(1+\varepsilon)} = \frac{(1-\varepsilon)}{(1+\varepsilon)} = e^{-\frac{\Delta E}{kT}}. \tag{1.4}$$

Utilizing a Taylor series expansion for $1/(1+\varepsilon)$ and the exponential turns the equation into,

$$(1-\varepsilon)(1-\varepsilon+\varepsilon^2-\varepsilon^3+\cdots) = 1 + \left(-\frac{\Delta E}{kT}\right) + \frac{1}{2}\left(-\frac{\Delta E}{kT}\right)^2 + \frac{1}{6}\left(-\frac{\Delta E}{kT}\right)^3 + \cdots \tag{1.5}$$

$$(1-\varepsilon+\varepsilon^2-\varepsilon^3+\cdots) + (-\varepsilon+\varepsilon^2-\varepsilon^3+\cdots) = 1 - \frac{\Delta E}{kT} + \left(\frac{1}{2}\right)\left(\frac{\Delta E}{kT}\right)^2 - \left(\frac{1}{6}\right)\left(\frac{\Delta E}{kT}\right)^3 + \cdots \tag{1.6}$$

Eliminating second-order and higher terms as part of the high temperature approximation and simplifying results in,

$$1 - 2\varepsilon = 1 - \frac{\Delta E}{kT}. \tag{1.7}$$

Finally, solving for ε gives the relative population difference of,

$$\varepsilon = \frac{\Delta E}{2kT} = \frac{\gamma \hbar B_o}{2kT}. \tag{1.8}$$

At a moderate magnetic field strength of 7.05 T and at 300 K, the relative population difference for ^{1}H would be $\varepsilon = 3.8 \times 10^{-6}$. Despite this lack of polarization, NMR is still a powerful tool used to solve various problems in the scientific community.

1.3.1 Static ^{13}C NMR of CO_2 in Physisorbing Solids

Static ^{13}C NMR of CO_2 can exhibit chemical shift anisotropy (CSA), where depending on the orientation of the CO_2 molecule with respect to the external magnetic field (B_o), the resonance frequency of the CO_2 molecule will change (Figure 1.3). This type of lineshape is observed when CO_2 molecules do not possess isotropic motion[25]. When CO_2 has isotropic motion, the resulting lineshape is Lorentzian in shape and is centered at its isotropic value, approximately 124.5 ppm. The CSA lineshape also has an isotropic value, and it is the average of the three tensor components describing the lineshape. A ^{13}C CSA lineshape with an isotropic chemical shift similar to CO_2 alone (124.5 ppm) is an indication of a physisorbing material. Physisorbing materials do not significantly alter the electronic structure of CO_2 and thus, do not alter the isotropic chemical shift either.

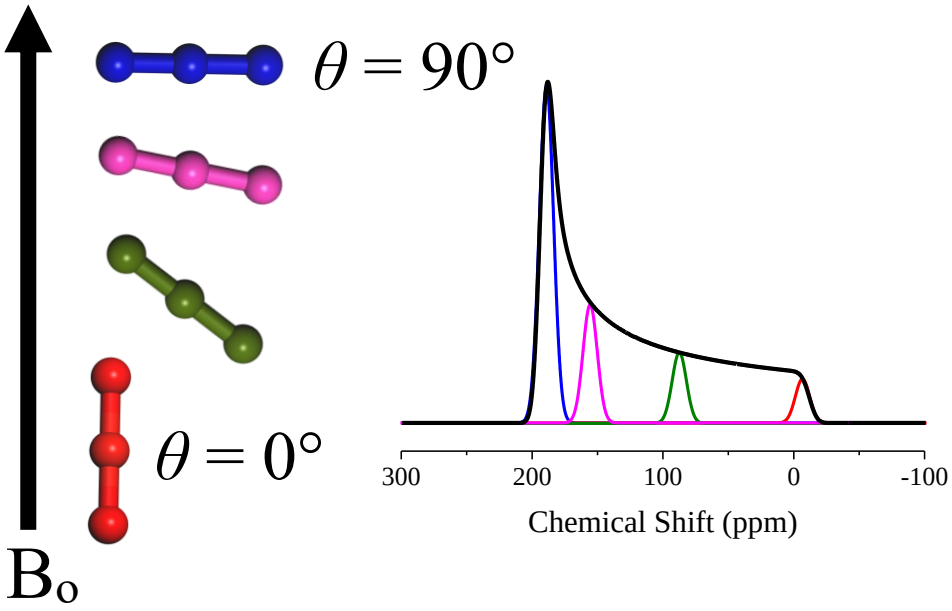

Figure 1.3: Multiple orientations of CO_2 with respect to the external magnetic field (left) and how the orientations translate to the CSA powder pattern observed in NMR (right). The colors of CO_2 molecules are coordinated with the colors of the Gaussian resonances under the CSA envelope. The black lineshape (right) is the sum of all the individual resonances (all orientations of the CO_2 molecules).

1.3.2 Second-Order Broadened Quadrupolar Nuclei

Quadrupolar nuclei have $I > 1/2$ and represent over 70% of NMR active isotopes in the periodic table[26]. Quadrupolar nuclei have a quadrupole moment, Q, which can interact with the electric field gradient (EFG) created by local surroundings. This additional interaction in the Hamiltonian usually causes lineshapes to be broadened, with there being a high degree of variability in the range of broadening. Unlike a $I = 1/2$ spin system, ultra-fast spinning rates (> 100kHz) cannot always narrow resonances into Gaussian lineshapes for quadrupolar nuclei (Figure 1.4). Magic-angle spinning partially averages out first-order quadrupolar interactions when the MAS rotor is spinning at the magic-angle (54.7°). However, the second-order quadrupolar interaction has a different orientational dependence and is only partially averaged when spinning at the magic-angle. Fortunately, higher magnetic fields can help overcome broadening from the relative amount of the second-order interaction. The second-order

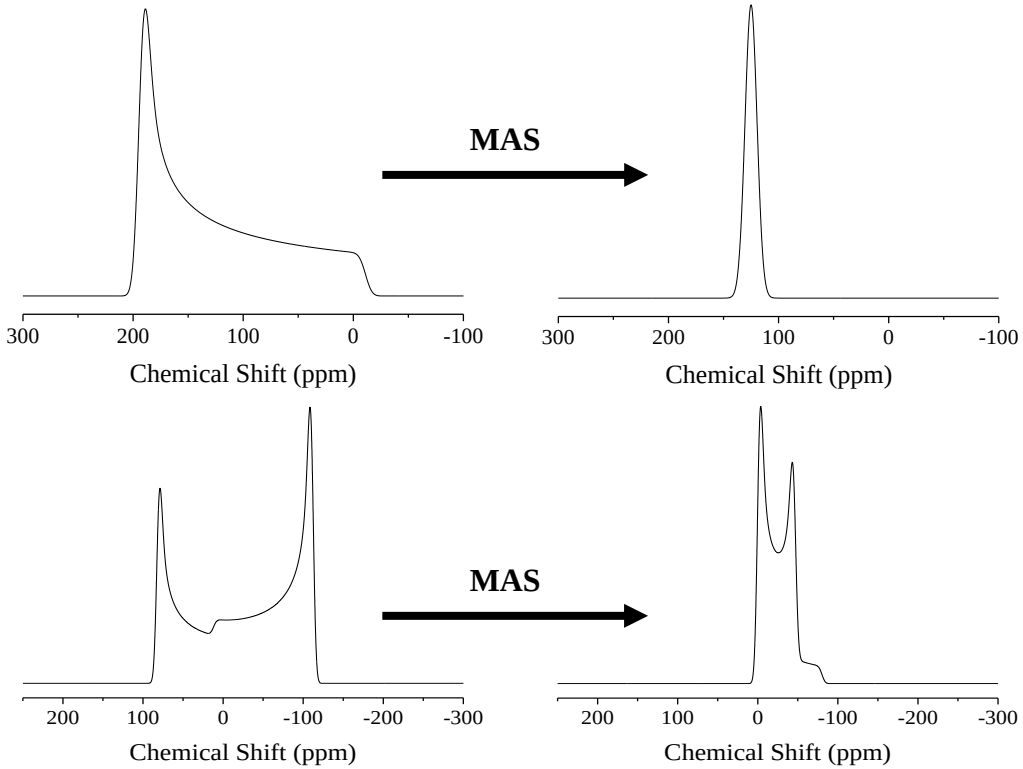

Figure 1.4: Simulated lineshapes: Static NMR lineshapes and the effect of magic-angle spinning (MAS) for $I = 1/2$ (top) and the central-transition for $I = 5/2$ with second-order quadrupolar effects dominating the lineshape (bottom).

quadrupolar term contains an important parameter that is often reported on in the literature, which is the quadrupolar coupling constant, C_Q. The C_Q value is a constant; thus, the value does not scale with magnetic field strength. For example, if a sample with one site is reported to have a C_Q = 10 MHz at a magnetic field strength of 7.05T, that sample measured at a magnetic field strength of 14.1T will also have C_Q = 10 MHz. However, the resonance will have a narrowed spectrum by a factor of four in ppm units (and a factor of two in frequency units) at the higher magnetic field strength, because the second-order quadrupolar interaction is inversely proportional to the magnetic field strength, as shown in Figure 1.5. This difference in linewidth for second-order broadened resonances for the central-transition is one of the many reasons that high magnetic field strengths are in such high demand, especially for sites with large C_Q values. In addition to the line narrowing at higher fields, the resonance also approaches its isotropic chemical shift value the higher the field goes. When a resonance has a large enough C_Q, the resonance is shifted from its isotropic value. This shift is called the isotropic second-order quadrupolar shift (or sometimes the quadrupolar induced shift, QIS), $\Delta\nu_{iso}^{(2)}$, and is defined as the following[26],

$$\Delta\nu_{iso}^{(2)} = -\frac{1}{30}\left[I(I+1)-\frac{3}{4}\right]\frac{\nu_Q^2}{\nu_o}\left(1+\frac{1}{3}\eta_Q^2\right), \quad (1.9)$$

where ν_Q is the quadrupolar frequency, ν_o is the Larmor frequency, and η_Q is the quadrupolar asymmetry parameter. In Figure 1.5, the quadrupolar asymmetry parameter, η_Q, is 0.0 and the isotropic chemical shift, δ_{iso}, is 0.0 ppm for both simulations. However, neither simulation has intensity at 0.0 ppm because of $\Delta\nu_{iso}^{(2)}$. Notice that the resonance at the higher magnetic field (the solid red curve) is approaching 0.0 ppm.

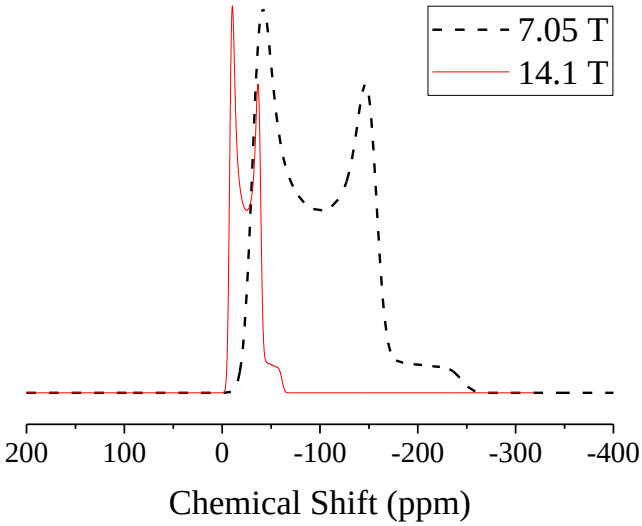

Figure 1.5: Simulations of $I = 5/2$ second-ordered broadened central-transition MAS NMR lineshapes with $\delta_{iso} = 0.0$ ppm, $\eta_Q = 0.0$, and $C_Q = 10$ MHz at a magnetic field strength of 7.05 T (dashed black curve) and 14.1 T (solid red curve). Simulations were executed using the Dmfit program. The simulation assumes infinite spinning frequency.

1.3.3 The Czjzek Distribution for Quadrupolar Nuclei

Some second-order broadened resonances do not possess the same lineshapes as those discussed in section 1.3.2. There exist resonances that have a distribution of second-order broadened lineshapes, resulting in a resonance that resembles a skewed Gaussian with the tail of the skew going to lower frequency. These types of lineshapes fit to what has been called a "Czjzek Distribution" and was discovered when G. Czjzek et al. solved the statistical problem of representing disorder to a distribution of EFGs in the early eighties[27]. This distribution is a result of structural disorder from the coordination environments around the probe nucleus (approximately 4 coordination spheres outwards) and causes variations in the EFG. A distribution of the quadrupolar interactions, resulting in the low frequency feature in the Czjzek model is present, even for nuclei with a high degree of local symmetry[28]. This type of resonance is often seen in glasses and aluminum oxides[29]. The C_Q value has a strong effect on the "tail" of the spectrum to the lower frequency side (seen in both spectra of Figure 1.6), whereas the higher frequency side is affected more by the full width at half max of the chemical

shift (FWHM) because of the degree of disorder and random orientations, which results in a distribution of resonances because of the isotropic second-order quadrupolar shift.

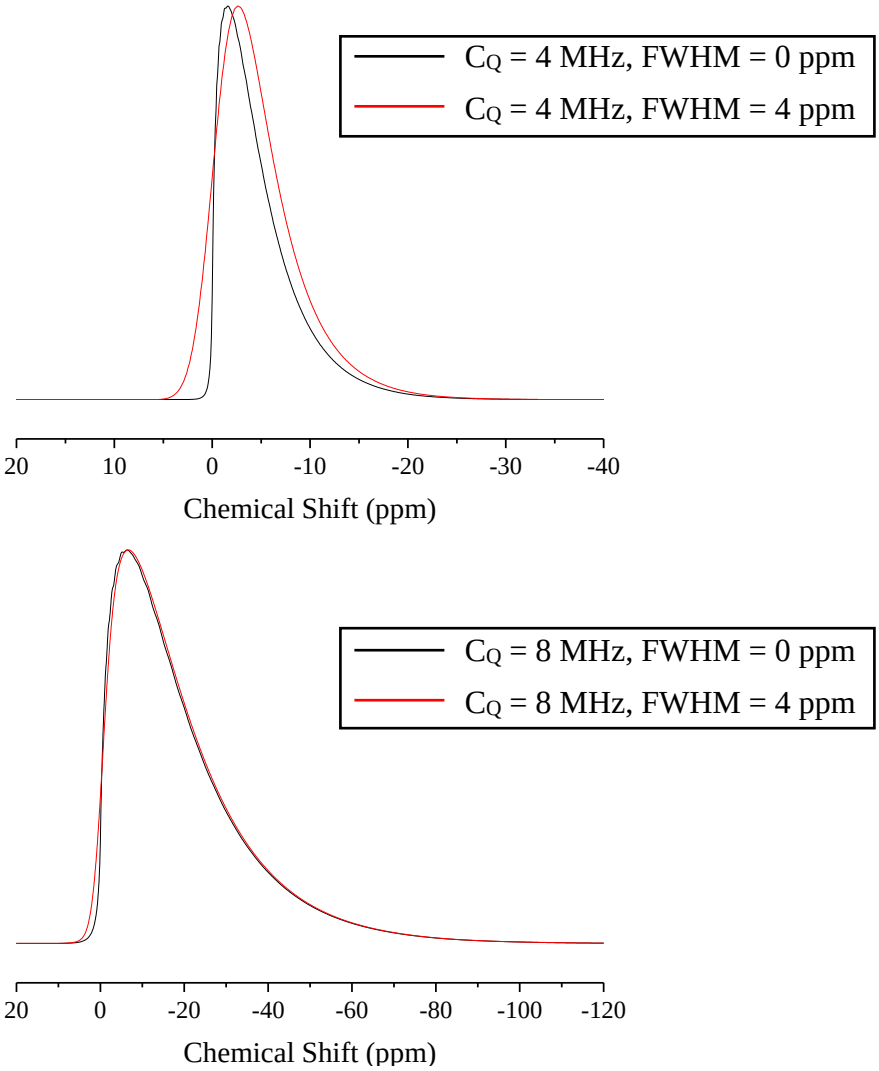

Figure 1.6: Simulations of $I = 5/2$ central-transition MAS NMR using the Czjzek model with δ_{iso} = 0.0 ppm, and MAS rate = 25 kHz at a magnetic field strength of 14.1 T. Simulations were executed using the Dmfit program. Top spectra have C_Q values of 4 MHz with the full width at half max variation in chemical shift (FWHM) of 0 ppm (black curve) and 4 ppm (red curve). Bottom spectra have C_Q values of 8 MHz with FWHM values of 0 ppm (black curve) and 4 ppm (red curve). Note the difference between the chemical shift scales between the top and bottom spectra.

1.3.4 Quantitative NMR of Quadrupolar Nuclei

Quadrupolar nuclei with multiple sites having different C_Q values need special consideration.

Despite having an appropriate excitation bandwidth for spectra, it is still possible to have

distortions in the intensities because not all sites nutate identically. This means a π/2 pulse for one site might be a π/4 pulse for another site, which makes it impossible to quantitatively acquire spectra using pulses that are too long. To quantitatively acquire NMR data for quadrupolar nuclei with less than 5% error[30], the following equation 1.10 must be used to determine an appropriate pulse width:

$$\left(I + \frac{1}{2}\right)\omega_{rf} t_1 \leq \frac{\pi}{6}, \tag{1.10}$$

where I is the nuclear spin quantum number, ω_{rf} is the radio frequency strength, and t_1 is the pulse duration. For I = 5/2, this means a π/18 (or a 10°) flip angle, with respect to the liquid standard, is necessary to acquire quantitative NMR spectra. Calculated values for NMR intensities of the central transition for I = 5/2 have shown a large dependence on the quadrupolar frequency, ν_Q, which is related to the quadrupolar splitting, ν'_Q, by,

$$\nu_{\mathrm{Q}} = \frac{3(\mathrm{e}^2 qQ)}{2I(2I-1)\mathrm{h}} \tag{1.11}$$

$$\nu'_{\mathrm{Q}} = \omega'_{\mathrm{Q}}/(2\pi) = \frac{\omega_{\mathrm{Q}}}{2\pi}\left[\frac{3}{2}(\cos^2\theta - 1) + \frac{1}{2}\eta\sin^2\theta\cos 2\Psi\right], \tag{1.12}$$

where the e is the elementary charge, q is the largest tensor component of the EFG, Q is the quadrupole moment, h is Planck's constant, η is the quadrupolar asymmetry parameter, and θ and Ψ are the Euler angles between the laboratory frame and the principal axes of the EFG tensor[26,31]. These intensities are also, affected by η, but to a much lesser extent than the quadrupolar splitting.

1.3.5 Baseline Correction

Acquiring time-domain NMR data using a pulse-acquire experiment (Bloch decay) results in the loss of some initial time-domain data because of the time it takes the electronics to switch from

muting the receiver and waiting an appropriate amount of time for ring down in the RF coil to subside, before acquiring the data. If the resulting spectrum has spinning sidebands, they could exhibit a phase twist. This phase twist can be fixed with a first-order phase correction, which is a phase correction that varies linearly with an offset, described in detail by James Keeler[32]. Using this first-order phase correction can result in a wavy baseline in the Fourier Transformed spectrum depending on the amount of correction needed, Figure 1.7. To fix the baseline, we utilize a program written by Maxime Yon while at CNRS-CEMHTI in Orléans, France. To begin the baseline correction, the "Sinus cardinal Fit: Frequency Guess" boxed in red in Figure 1.9 was used. This is done using a "guess and check" method for initial values. This spectrum in the figure used an initial guess of 0.0002, which captured most of the wavy baseline (see inset of Figure 1.8). From here there are a couple of options to finish the baseline correction. There is an autocorrect fitting that works well if the S/N ratio is very good, otherwise the autocorrection can

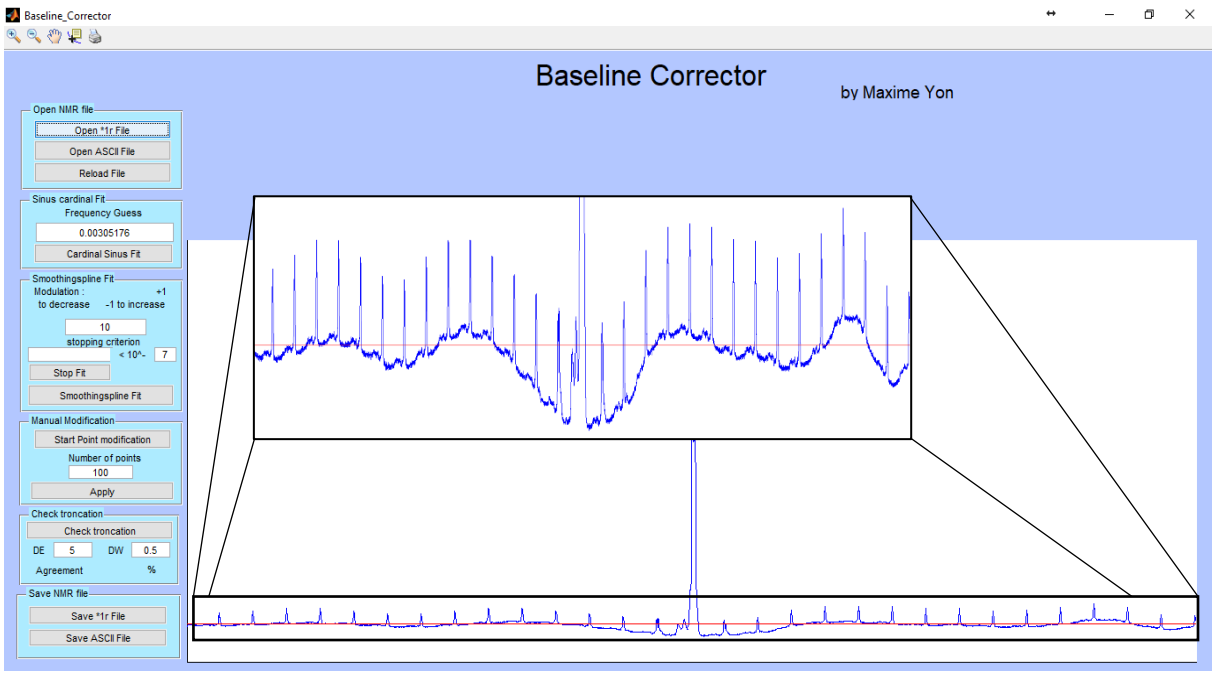

Figure 1.7: ^{27}Al NMR spectrum imported from TopSpin (Bruker). The inset is a zoomed in version of the baseline to make the wavy baseline easier to see. No correction has been implemented yet, so the red baseline correcting line is straight.

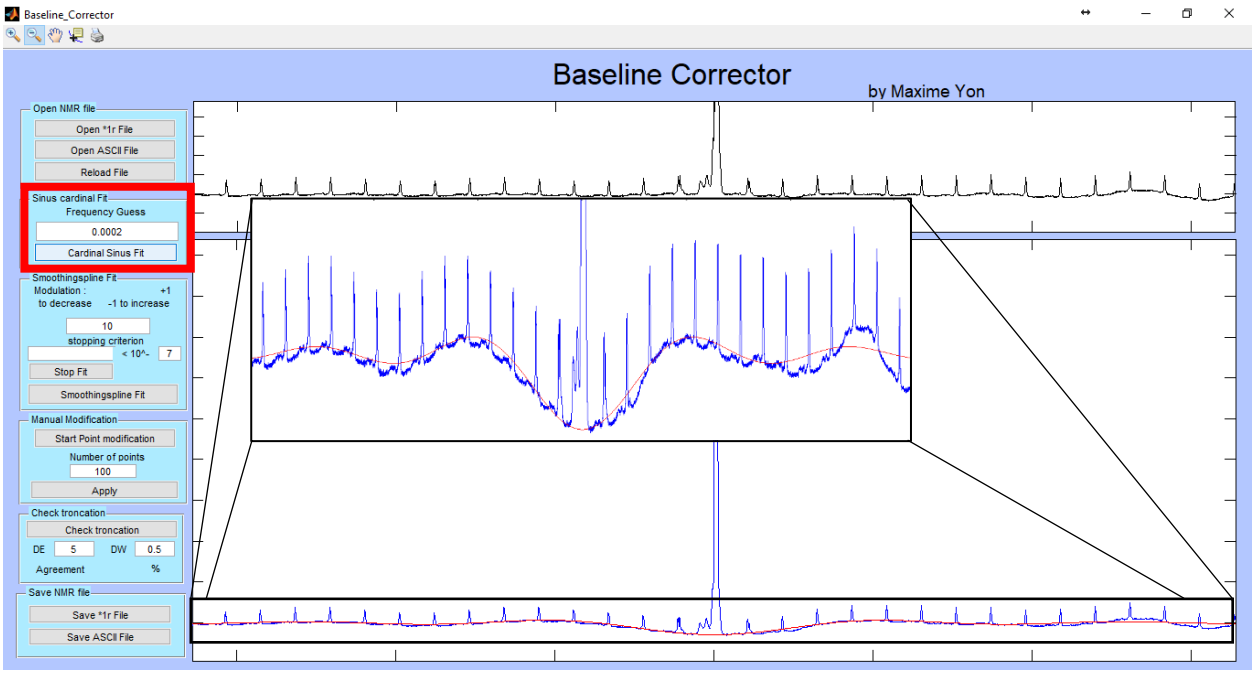

Figure 1.8: An initial guess of 0.0002 for the "sinus cardinal fit," which gives approximately the correct modulation. Notice here how the red line is no longer straight compared to Figure 1.7.

mistake low-intensity spinning sidebands as noise. The other option is to manually perform the final correction, which can introduce some error, but can also work well. TopSpin files have an option to check the accuracy of a baseline correction. This is done by comparing the original wavy baseline to what should be expected in the full FID (receiver on immediately) had initial points zeroed-out and then Fourier transformed.

The baseline corrector program now has a spectrum that is "corrected" and can be transformed back into time-domain data, which is similar to a linear back prediction of the time-domain data. This "corrected" time-domain data is what would be expected if there was no loss time in the initial part of the FID because of electronics. Then the program will take the "corrected" time-domain data and zero out the appropriate amount of points based on the dwell time and number of points to account for the amount of time in between the end of the pulse and the start of the

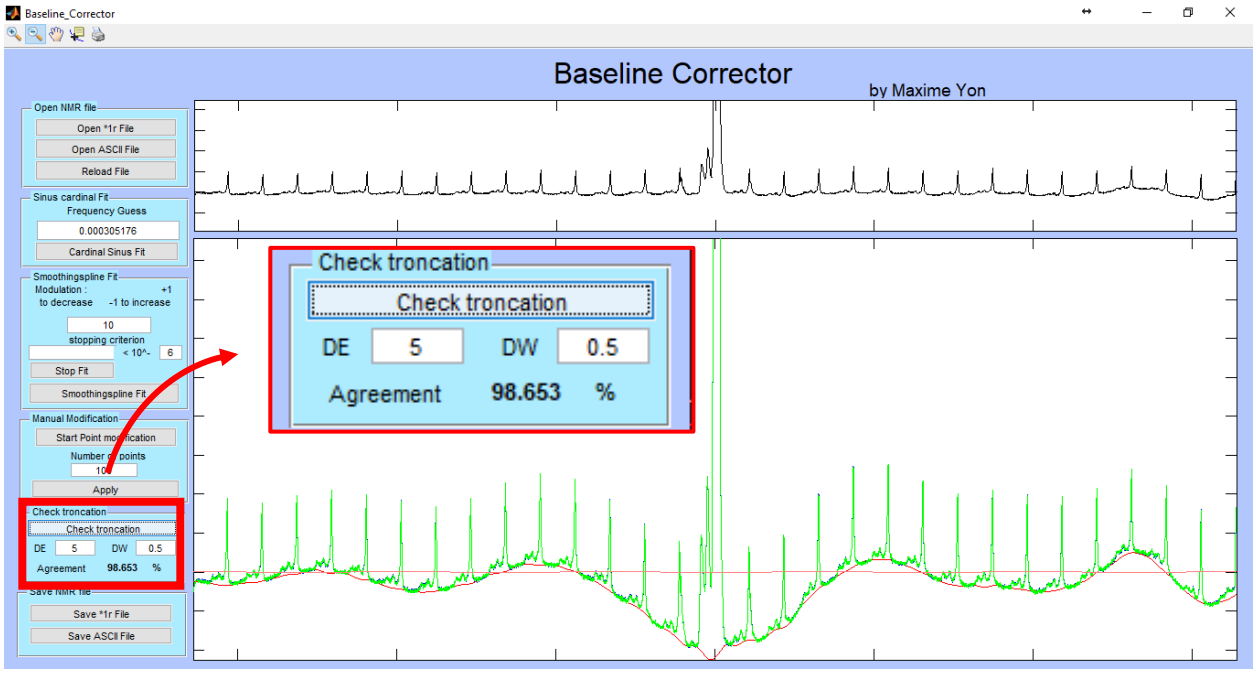

Figure 1.9: Checking the quality of the baseline correction. The green "expected" wavy baseline is overlaid on top of the actual wavy baseline, which is blue and cannot be seen because of the excellent agreement between the expected and actual spectra.

receiver. Fourier transforming the time-domain data with the zeroed-out points should look like the actual Fourier transformed data. Now the two can be compared to determine the quality of the baseline correction, Figure 1.9.

References

[1] J.R. Petit, J. Jouzel, D. Raynaud, N.I. Barkov, J.M. Barnola, I. Basile, M. Bender, J. Chappellaz, M. Davis, G. Delaygue, M. Delmotte, V.M. Kotiyakov, M. Legrand, V.Y. Lipenkov, C. Lorius, L. Pépin, C. Ritz, E. Saltzman, M. Stievenard, Climate and atmospheric history of the past 420,000 years from the Vostok ice core, Antarctica, Nature. 399 (1999) 429–436. doi:10.1038/20859.

[2] National Oceanic and Atmospheric Administration: Earth System Research Laboratory - Global Monitoring Division, Trends in Atmospheric Carbon Dioxide, (2018).

[3] R.A. Rasmussen, M.A.K. Khalil, Atmospheric Methane (CH_4): Trends and Seasonal Cycles, J. Geophys. Res. 86 (1981) 9826–9832.

[4] C. Lorius, J. Jouzel, D. Raynaud, J. Hansen, H. Le Treut, The ice-core record: climate sensitivity and future greenhouse warming, Nature. 347 (1990) 139–145.

[5] W. Wang, G. Molnar, M.K.W. Ko, S. Goldenberg, N.D. Sze, Atmospheric trace gases and global climate : a seasonal model study, Tellus B Chem. Phys. Meteorol. 42B (1990) 149–161. doi:10.3402/tellusb.v42i2.15200.

[6] B.D. Santer, K.E. Taylor, T.M. Wigley, T.C. Johns, P.D. Jones, D.J. Karoly, J.F.B. Mitchell, A.H. Oort, J.E. Penner, V. Ramaswamy, M.D. Schwarzkopf, R.J. Stouffer, S. Tett, A Search for Human Influence on the Thermal Structure of Atmosphere, Nature. 382 (1996) 39–46.

[7] J. Perez-Garcia, L.A. Joyce, A.D. McGuire, X. Xiao, Impacts of Climate Change on the

Global Forest Sector, Clim. Change. 54 (2002) 439–461. doi:10.1023/A:1016124517309.

[8] E.A.G. Schuur, A.D. McGuire, C. Schädel, G. Grosse, J.W. Harden, D.J. Hayes, G. Hugelius, C.D. Koven, P. Kuhry, D.M. Lawrence, S.M. Natali, D. Olefeldt, V.E. Romanovsky, K. Schaefer, M.R. Turetsky, C.C. Treat, J.E. Vonk, Climate change and the permafrost carbon feedback, Nature. 520 (2015) 171–179. doi:10.1038/nature14338.

[9] E. By:, T.F. Stocker, D. Qin, G.-K. Plattner, M.M.B. Tignor, S.K. Allen, J. Boschung, A. Nauels, Y. Xia, V. Bex, P.M. Midgley, IPCC in Climate Change 2013: The Physcial Science Basis. Working Group I Contribution ot the Fifth Assesment Report of the Intergovernmental Panel on Climate Change, (2013).

[10] C.W. Jones, CO_2 Capture from Dilute Gases as a Component of Modern Global Carbon Management, Annu. Rev. Chem. Biomol. Eng. 2 (2011) 31–52. doi:10.1146/annurev-chembioeng-061010-114252.

[11] Y.S. Jun, D.E. Giammar, C.J. Werth, C.W. Jones, Impacts of geochemical reactions on geologic carbon sequestration, Environ. Sci. Technol. 47 (2013) 3–8. doi:10.1021/es3027133.

[12] A.S. Bhown, B.C. Freeman, Analysis and Status of Post-Combustion Carbon Dioxide Capture Technologies, Environ. Sci. Technol. 45 (2011) 8624–8632. doi:10.1021/es104291d.

[13] C.-H. Chen, D. Shimon, J.J. Lee, S.A. Didas, A.K. Mehta, C. Sievers, C.W. Jones, S.E. Hayes, Spectroscopic Characterization of Adsorbed $^{13}CO_2$ on 3-Aminopropylsilyl-Modified SBA15 Mesoporous Silica, Environ. Sci. Technol. 51 (2017) 6553–6559.

doi:10.1021/acs.est.6b06605.

[14] D. Shimon, C.-H. Chen, J.J. Lee, S.A. Didas, C. Sievers, C.W. Jones, S.E. Hayes, ^{15}N Solid State NMR Spectroscopic Study of Surface Amine Groups for Carbon Capture: 3-Aminopropylsilyl Grafted to SBA-15 Mesoporous Silica, Environ. Sci. Technol. 52 (2018) 1488–1495. doi:10.1021/acs.est.7b04555.

[15] C. Cadena, J.L. Anthony, J.K. Shah, T.I. Morrow, J.F. Brennecke, E.J. Maginn, Why is CO2 so Soluble in Imidazolium-Based Ionic Liquids?, J. Am. Chem. Soc. 126 (2004) 5300–5308. doi:10.1021/ja039615x.

[16] X. Zhang, X. Zhang, H. Dong, Z. Zhao, S. Zhang, Y. Huang, Carbon capture with ionic liquids: overview and progress, Energy Environ. Sci. 5 (2012) 6668–6681. doi:10.1039/c2ee21152a.

[17] X. Kong, E. Scott, W. Ding, J.A. Mason, J.R. Long, J.A. Reimer, CO_2 Dynamics in a Metal − Organic Framework with Open Metal Sites, J. Am. Chem. Soc. 134 (2012) 14341−14344. doi:10.1021/ja306822p.

[18] L.-C. Lin, J. Kim, X. Kong, E. Scott, T.M. McDonald, J.R. Long, J. a. Reimer, B. Smit, Understanding CO_2 Dynamics in Metal-Organic Frameworks with Open Metal Sites, Angew. Chemie. 125 (2013) 4506–4509. doi:10.1002/ange.201300446.

[19] R.M. Marti, J.D. Howe, C.R. Morelock, M.S. Conradi, K.S. Walton, D.S. Sholl, S.E. Hayes, CO_2 Dynamics in Pure and Mixed-Metal MOFs with Open Metal Sites, J. Phys. Chem. C. 121 (2017) 25778–25787. doi:10.1021/acs.jpcc.7b07179.

[20] C.M. Moran, R.M. Marti, S.E. Hayes, K.S. Walton, Synthesis and characterization of

aluminum carbide-derived carbon with residual aluminum-based nanoparticles, Carbon N. Y. 114 (2017) 482–495. doi:10.1016/j.carbon.2016.11.083.

[21] J.K. Moore, M.D. Guiver, N. Du, S.E. Hayes, M.S. Conradi, Molecular Motions of Adsorbed CO_2 on a Tetrazole-Functionalized PIM Polymer Studied with ^{13}C NMR, J. Phys. Chem. C. 117 (2013) 22995–22999.

[22] J.K. Moore, R.M. Marti, M.D. Guiver, N. Du, M.S. Conradi, S.E. Hayes, CO_2 Adsorption on PIMs Studied with ^{13}C NMR Spectroscopy, J. Phys. Chem. C. 122 (2018) 4403–4408. doi:10.1021/acs.jpcc.7b12312.

[23] J.L. Anthony, E.J. Maginn, J.F. Brennecke, Solubilities and thermodynamic properties of gases in the ionic liquid 1-n-butyl-3-methylimidazolium hexafluorophosphate, J. Phys. Chem. B. 106 (2002) 7315–7320. doi:10.1021/jp020631a.

[24] A. Abragam, The Principles of Nuclear Magnetism, Oxford Univeristy Press, London, 1961.

[25] M.H. Levitt, Spin Dynamics: Basics of Nucear Magnetic Resonance, 2nd ed., John Wiley and Sons, Ltd, 2008.

[26] R.E. Wasylishen, S.E. Ashbrook, S. Wimperis, eds., NMR of Quadrupolar Nuclei in Solid Materials, John Wiley and Sons, Ltd, West Sussex, 2012.

[27] G. Czjzek, J. Fink, F. Götz, H. Schmidt, Atomic coordination and the distribution of electric field gradients in amorphous solids, Phys. Rev. B. 23 (1981) 2513–2530.

[28] J. Espinose, D. Lacaillerie, C. Fretigny, D. Massiot, MAS NMR spectra of quadrupolar nuclei in disordered solids : The Czjzek model, J. Magn. Reson. 192 (2008) 244–251.

doi:10.1016/j.jmr.2008.03.001.

[29] D. Massiot, F. Fayon, M. Capron, I. King, S. Le Calvé, B. Alonso, J.O. Durand, B. Bujoli, Z. Gan, G. Hoatson, Modelling one- and two-dimensional solid-state NMR spectra, Magn. Reson. Chem. 40 (2002) 70–76. doi:10.1002/mrc.984.

[30] E. Lippmaa, A. Samoson, M. Magi, High-Resolution 27Al NMR of Aluminosilicates, J. Am. Chem. Soc. 108 (1986) 1730–1735.

[31] D. Fenzke, D. Freude, T. Fröhlich, J. Haase, NMR Intensity Measurements of Half-Integer Quadrupole Nuclei, Chem. Phys. Lett. 111 (1984) 171–175.

[32] J. Keeler, Understanding NMR Spectroscopy, 1st ed., Cambridge, 2002.

Chapter 2: CO_2 Dynamics in MOF-74

2.1 Metal-Organic Frameworks (MOFs)

Metal-organic frameworks (MOFs) are ordered porous materials that can be used for a wide range of applications such as adsorbents, molecular sieves, hosts for drug delivery, and many others[1–10]. Many MOFs are synthesized from a solvothermal reaction that requires a metal source, solvent, organic linker, and heat (Figure 2.1). Each MOF has characteristic motifs (i.e., pore size, channel structure, etc.) that distinguish one from another; these distinct features are dictated by the linker and metal, typically. The opportunities for synthesizing these highly

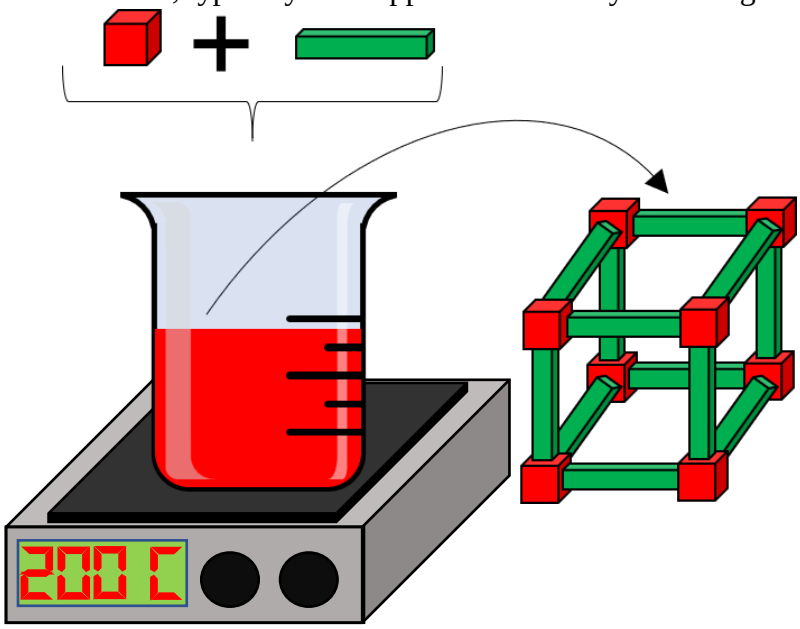

Figure 2.1: Generic MOF synthesis, where the red cube is the metal, the green rectangular prism is the organic linker, and the beaker is filled with solvent on top of a heating plate. Note, the heating plate setting of 200 °C was arbitrarily chosen.

tailorable porous materials has been an area of intense study due to the flexible synthesis with diverse organic linkers and metals[11–14], that exploits metals as catalysts and gives them a tailored structure in which to reside (unlike Pd-doped carbons or similar materials).

2.1.1 M-MOF-74 Structure and CO_2 Adsorption

M-MOF-74 is the name of a specific class of MOF that can be synthesized with a number of divalent metals (M = Mg, Ni, Zn, Co, etc.)[15,16]. Figure 2.2a depicts the honeycomb-like structure of M-MOF-74. The five metal-oxygen bonds at the open metal site that form a nearly square-planar polyhedron is highlighted in Figure 2.2b. These polyhedra are connected together by linkers leading to 1-dimensional hexagonal channels (perpendicular to the page, Figure 2.2a) lined with open metal sites. The open metal sites are partially responsible for the reason why

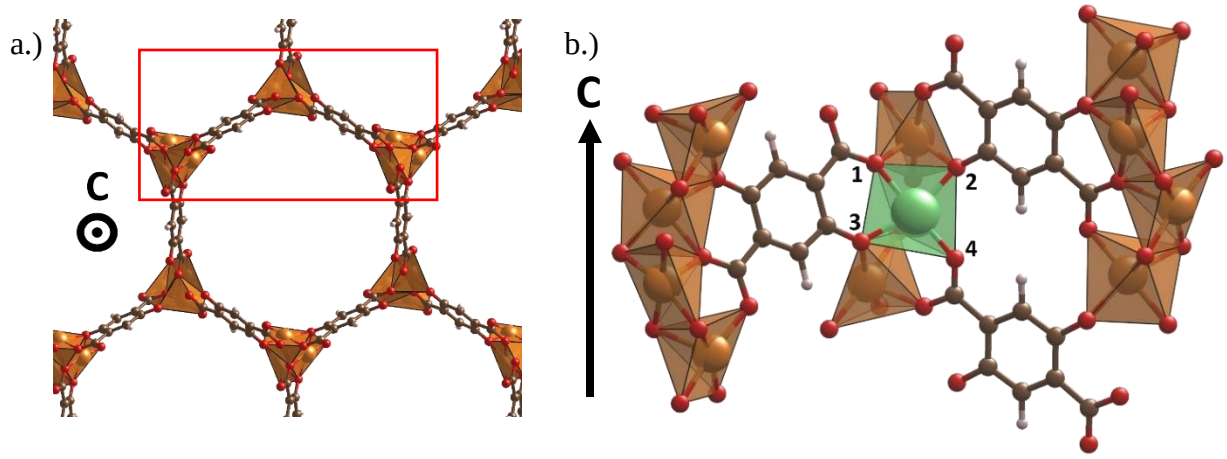

Figure 2.2: a.) The hexagonal honeycomb structure of M-MOF-74 shown with the c-axis along the channel, normal to the page and b.) depiction of the handedness of the metal backbone (boxed in red in a.)) in addition to the four most likely binding positions of CO_2 to the open metal site, with position 4 being the most favorable.

Mg-MOF-74 is such a good adsorbent for CO_2. The electron deficient metal site interacts with the electron rich lone pair on the oxygen of CO_2 through a van der Waals interaction, resulting in Mg-MOF-74 concentrating CO_2 inside its channels. In this study, we focus on Mg-MOF-74 and mixed metal $Mg_{0.77}$—$Cd_{0.23}$-MOF-74, wherein Cd ions are substituted for some of the Mg ions in the MOF-74 topology. Interest in mixed-metal MOF-74 materials has been motivated by a previous study[7] that showed the substitution of even 16% of the Mg sites in Mg-MOF-74 with Ni is enough to stabilize the structure under humid conditions. Mixed-metal MOFs are explored

in an effort to evaluate how different metals are taken up in the final MOF structure in binary mixtures with Mg.

2.1.2 Synthesis of Mg-MOF-74 and "Mixed Metal" MOF-74

The MOFs investigated in this study were Mg-MOF-74 and Mg_{1-x}—Cd_x-MOF-74, where x is the fraction of metal sites that are Cd. These materials were synthesized as part of a collaborative project with Dr. Cody Morelock from Prof. Krista Walton's group (Georgia Institute of Technology). The materials used to synthesize these MOFs were purchased from commercial entities, without further purification. The metal sources are $Mg(NO_3)_2 \cdot 6H_2O$ from Sigma-Aldrich and $Cd(CH_3COO)_2 \cdot 2H_2O$ from ACROS Organics; the organic linker, 2,5-dihydroxy-1,4-benzenedicarboxylic acid (DOBDC) from TCI America; and *N*, *N*-dimethylformamide (DMF), ethanol, and methanol from VWR. The synthesis of Mg-MOF-74 was based on previous work from Glover et al[17]. To a mixture of 360 mL of DMF, 24 mL of ethanol, and 24 mL of deionized H_2O in an Erlenmeyer flask, 14.81 mmol ($Mg(NO_3)_2 \cdot 6H_2O$ and 4.8 mmol DOBDC were added under continuous stirring. Approximately 10 mL portions of the resulting mixture were transferred to 20 mL scintillation vials, which were tightly sealed and placed in a sand bath. The reaction mixture was heated in a preheated oven at 120 °C for 24 h. After cooling to room temperature, the mother liquor was decanted from each vial and replaced with fresh DMF, which was subsequently exchanged five times over 2 days with methanol. The products in each vial were combined into one larger vessel and stored under methanol at room temperature until subsequent characterizations were performed. The "mixed-metal" MOF-74 sample containing 77% Mg and 23% Cd was prepared in a similar manner as the parent Mg-MOF-74, except now using 10.39 mmol $Mg(NO_3)_2 \cdot 6H_2O$ and 4.44 mmol $Cd(CH_3COO)_2 \cdot 2H_2O$, rather than $Mg(NO_3)_2 \cdot 6H_2O$ alone.

2.1.3 Characterization Methods

Powder X-ray diffraction (PXRD) was employed by Dr. Cody Morelock to verify the crystallinity and phase purity of as-synthesized samples by comparing simulated PXRD patterns of the parent MOF-74 structure and those collected at room temperature on a PANalytic X'Pert X-ray diffractometer equipped with an X'Celerator detector module and using Cu Kα (λ = 1.5418 Å) radiation. Inductively coupled plasma optical emission spectrometry (ICP-OES) was used for elemental analysis of Mg and Cd in Mg_{1-x}—Cd_x-MOF-74. ICP-OES was performed on a PerkinElmer 7300DV ICP-OES instrument to determine the amount of each metal present. Prior to analysis, 15−20 mg of as-synthesized $Mg_{0.77}$−$Cd_{0.23}$-MOF-74 was activated at 250 °C for 12 h under vacuum.

2.1.4 Computational Methods

As part of this collaborative project, Dr. Joshua Howe from Prof. David Sholl's group (Georgia Institute of Technology) performed computational studies of MOF structures. Fully periodic density functional theory (DFT) with a planewave basis set within the Vienna Ab initio Simulation Package (VASP)[18] was used to study Mg-MOF-74, and adsorption of CO_2 therein. Projector augmented wave (PAW) pseudopotentials[19] and the generalized gradient approximation of Perdew, Burke, and Ernzerhof (PBE)[20] with the third version of the dispersion correction by Grimme et al. (DFT-D3)[21] was used to study all systems in order to account for dispersion interactions, which are important to consider for intermolecular interactions. A planewave basis set cutoff energy of 600 eV with k-point sampling at the Γ-point was used to optimize unit cell lattice vectors and ionic positions until interionic forces were <0.01 eV/Å.

To study the Mg-MOF-74 structure loaded with CO_2, initial atomic coordinates were based on structural information from Cu-MOF-74 loaded with CO_2, which was determined by powder neutron diffraction data at 10K and showed the presence of three unique adsorption sites for CO_2 in the 1-dimensional channel[22]. We note that, because all of these sites can be simultaneously populated in the DFT calculations (even though as a practical, physical detail they are not simultaneously all populated in the experiment), this aspect of computational studies allowed us to probe CO_2 loadings greater than 1 molecule per metal site (up to 2.17 molecules per metal site). Mg ions were isostructurally substituted into the Cu-MOF-74 structure at the Cu sites, which was used as the starting point for optimizing the CO_2-loaded Mg-MOF-74 structure. This optimized structure was used as the starting point for all CO_2 loadings, except in calculations with only one CO_2 per unit cell (0.17 CO_2 per open metal site or 1 CO_2 per 6 Mg sites), which started from a previously reported structure of CO_2 adsorbed in Mg-MOF-74 at the vdW-DF2 level of theory[23]. For the reference energy of the isolated CO_2 molecule, CO_2 was optimized in a box of side length 20 Å.

2.1.5 Activation of MOF-74

Mg-MOF-74 and $Mg_{0.77}$–$Cd_{0.23}$-MOF-74 samples were stored in methanol after synthesis and were activated after decanting and drying under vacuum to avoid water adsorption. This detail is crucial, because even though water can be desorbed from the MOF, it diminishes both the CO_2 adsorption capacity[24] and the BET surface area of the MOF without changing the crystal structure and unit cell dimensions (evidenced by its PXRD pattern)[25]. When activating a MOF sample for the first time, a small amount of sample was loaded into a 10 mm test tube with a visible layer of methanol just above the material. Activation of the MOF was achieved by continuously applying vacuum to the sample for 2 h, followed by heating the sample under

vacuum to 65 °C for 2 h, and then to 250 °C for 12 h, and subsequently cooled to room temperature. Once activated, CO_2 was loaded into the MOF-74 materials (on the same manifold without disturbing the sample container) and allowed to equilibrate to a final pressure of 1 atm at room temperature (295 K). Subsequently, the 10 mm test tube was flame-sealed to ensure a water-free environment.

A second configuration with a valved sample space (Figure 2.3) was used for variable CO_2 loadings in Mg-MOF-74. Sample was loaded into the chamber (indicated in Figure 2.3), and all activation was executed on the sample in this apparatus. To reactivate a previously activated and CO_2-exposed MOF, the sample was heated to approximately 160 °C for 3 h while under vacuum (< 35 mTorr). The sample was cooled to room temperature while under vacuum before loading with different amounts of CO_2.

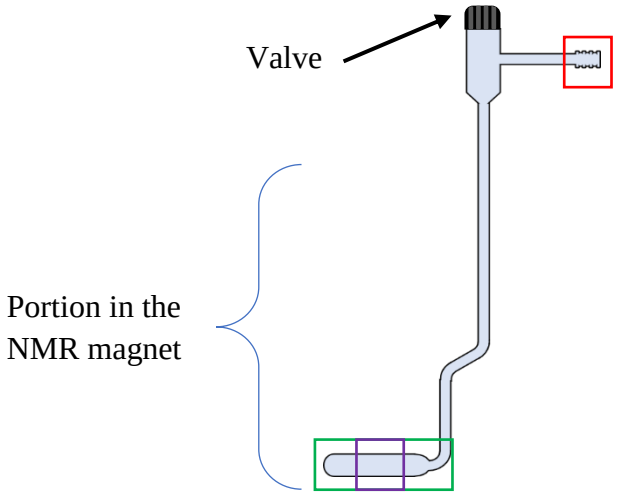

Figure 2.3: Valved glassware that allows for variable loading of CO_2. This configuration can connect to a gas manifold via a Chemglass fitting (boxed in red). The sample space is boxed in green and the NMR coil region is boxed in purple.

2.1.6 Static ^{13}C NMR Studies

Static ^{13}C variable temperature (VT) NMR was performed from temperatures ranging from 8.5 to 295 K for Mg-MOF-74 and $Mg_{0.77}$–$Cd_{0.23}$-MOF-74. Each sample was loaded with 1 atm $^{13}CO_2$ at room temperature, yielding loadings of 1.1 and 1.0 CO_2 molecules per metal site, respectively (loading levels for Mg-MOF-74 was determined using isotherm data from Queen et al.[22] and isotherm data in Figure 2.4 was used to determine the loading level for $Mg_{0.77}$–$Cd_{0.23}$-MOF-74).

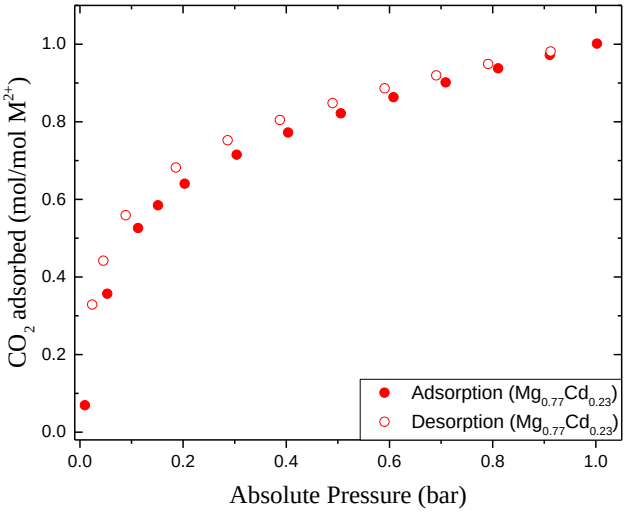

Figure 2.4: CO_2 isotherm data for $Mg_{0.77}$—$Cd_{0.23}$-MOF-74 measured at 25 °C.

Measurements were recorded on a 202 MHz (4.74 T) magnet at a ^{13}C Larmor frequency of 50.827 MHz using two different home-built static single-channel NMR probes. A combination of single-pulse (Bloch decay) and Hahn echo[26] experiments was used to acquire static ^{13}C VT NMR data. All ^{13}C spectra were referenced to $^{13}CO_2$ gas at 124.5 ppm. For low temperatures from 8.5 to 100 K, a Kadel liquid helium dewar[27] (Figure 2.5a) was utilized, which has a carbon-glass resistance temperature sensor (CGR) for low temperature measurements. For

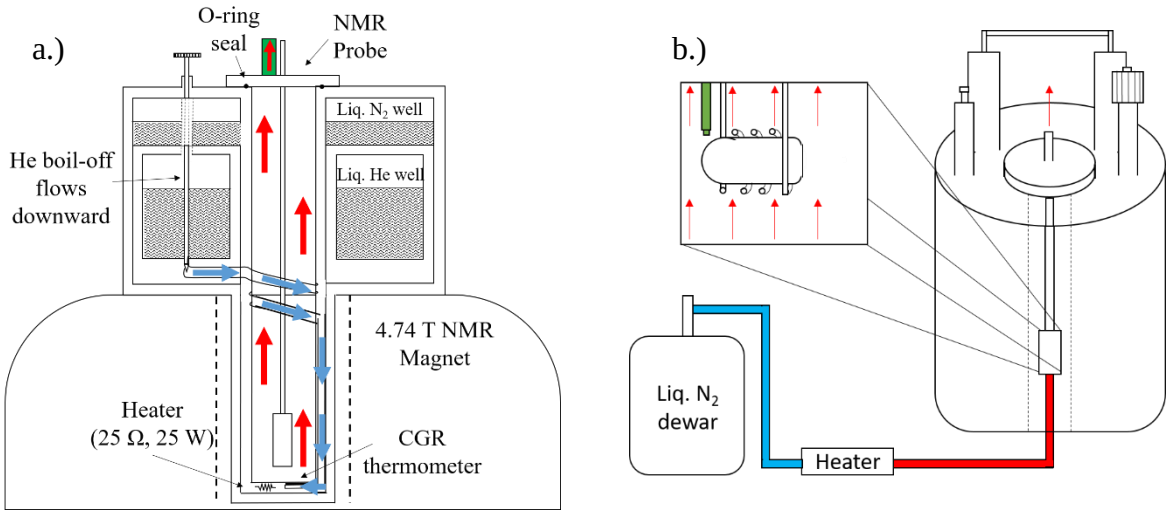

Figure 2.5: a.) NMR static cryogenic probe and dewar used for temperatures of 8 – 100 K. A Kadel cryogenic dewar is coupled with a single-channel homebuilt NMR probe. Helium boil-off (blue arrows) travels through piping to a heater which warms the helium gas to the desired temperature (red arrows), delivering a temperature regulated stream of helium gas to the sample space. Helium gas temperature is regulated using a Lake Shore Cryogenic temperature controller. Helium gas exits the dewar through additional piping (highlighted in green), which is connected to a helium recovery system. Figure adapted from Dr. Eun-Kee Jeong's thesis[27]. b.) Static NMR cryogenic probe and dewar used for temperatures of 125K – room temperature. Power resistors inside the liquid N_2 dewar create boil-off to ensure a continuous flow of N_2 gas. The cold N_2 gas then travels through a heater, controlled by an Omega temperature controller. Sample temperature is monitored with a type-T thermocouple (highlighted in green in inset). For the variable-loading experiments, the sample has a glass stem that is valved off.

temperatures from 124 K to just below room temperature, a home-built NMR probe coupled to a liquid nitrogen dewar (Figure 2.5b) was used to deliver a temperature regulated stream of N_2 gas to the sample space, where temperature control was measured with a type T thermocouple placed next to the sample.

2.1.7 Using the Kadel Cryogenic Dewar (8 – 100 K): Practical Aspects and Instructions

Before making use of the Kadel cryogenic dewar (from now on referred to as "dewar"), the variable capacitor on the NMR probe was unsoldered from the LC circuit of the probe and baked out. The variable capacitor was placed in an oven heated to 100 °C for at least 30 minutes for the

bake out procedure. The variable capacitor was then re-soldered to the LC circuit just before the probe was ready to be placed in the dewar, to avoid any moisture that might come in contact with the variable capacitor. Note, if this step is skipped and the cryogens are already in the dewar, there is potential for the variable capacitor to freeze and become immovable.

The vacuum jacket of the dewar was pumped down before use in NMR experiments. On the side of the dewar, there is a fitting where an actuator valve can connect to. This allows the vacuum jacket to get pumped down, without needing to open the vacuum jacket to atmosphere. A roughing pump is typically good enough for the purpose of this setup.

Before filling with any cryogens, the helium well is purged with ultra high purity (UHP) helium gas to "clean out" anything that can become solid at liquid helium temperatures, and the nitrogen well is purged with nitrogen gas. After the purging gases are in place, the variable capacitor is reconnected to the LC circuit and quickly placed inside the dewar. After purging the helium well for at least two hours, the nitrogen well is filled with liquid nitrogen to start the cooling process. Initially, only a partial fill the nitrogen well is done. This is because the nitrogen well is very hot compared to the liquid nitrogen, which results in a large flux of nitrogen gas boil-off. The nitrogen well is filled several times over the course of a day or two, until the temperature near the sample space is approximately 80K (measured with the CGR temperature sensor). Next, the helium well is filled with liquid helium.

The first fill of liquid helium is done while the transfer line is "hot" and purging from the helium boil-off created in the supply dewar. This is because there is no liquid helium inside the dewar yet and it allows for an additional stream of high purity helium gas to help purge the helium well. If it is not the first time filling liquid helium and there is still liquid helium in the well, then the

fill was done in a similar fashion to magnet fills. Depending on the amount of helium boil-off, the dewar was re-filled every 3-4 days. The helium level was measured using a dipstick and a calibrated Wheatstone bridge.

Temperature regulation was achieve using a Lake Shore Cryogenics, Inc. "Cryogenic Temperature Controller – Model 520." Knowing the He boil-off flow rate out of the center bore (see red arrows in Figure 2.5a) is essential to temperature regulation. Table 2.1 is a list of settings and flow rates that aided in temperature regulation. Note that the "Mix" control knob has outer and inner knobs. The outer black control knob is set to "Mix," and the red inner control knob setting is determined by the desired temperature. The setting for the red inner control knob is determined from the Mix column of Table 2.1. The red control knob does not have a 360^{o} rotation to it, but the values in the Mix column are recorded as if the knob did have the full 360^{o} rotation. For example, while facing the temperature controller, a value of ¼ mix means that the knob is pointing to the left, and a value of ½ mix means the knob is pointing up, and a value of ¾ mix means the knob is pointing right. The Res (-) and Res (+) settings are for the different

Table 2.1: Temperature controller settings and gas flow rates.

Target Temp. (K)	Sensor Current µA	Diode Res (-) Res (+)	HTR Current Range mA	Set Point	Mix	He Flow (Center Bore) (SCFH)	He Flow (Boil off) (SCFH)
20	100	(-)	30	07400	1/4	1.1	1.1
30	100	(-)	30	03780	1/2	0.85	0.8
40	100	(-)	100	02910	1/2	0.6	0.5
50	100	(-)	100	02498	1/6	0.5	0.8
60	100	(-)	300	02180	1/4	0.7	0.6
75	100	(-)	300	01922	1/3	0.9	0.65
80	100	(-)	300	01800	1/3	0.65	0.65
100	100	(-)	300	01630	2/3	0.6	1.0
120	100	(+)	300	03892	3/4	0.7	1.1
125	100	(+)	300	04150	3/4	0.5	1.2
146	100	(+)	1000	04920	1/3	1.15	1.3
160	100	(+)	1000	05690	1/3	1.35	1.5

type of thermometers (CGR or PRT, respectively) that can be used on the probe. For the experiments performed here, the setting was always Res(-), because only temperatures below 100 K were measured with this setup.

Temperature measurements are measured using a ratio of voltages. There is a two-prong "banana plug" that connects to a home-built piece of equipment that connects to a voltmeter (set to read on an AC mV scale). These readings are based on the following relationship: V = IR, where V is voltage, I is current, and R is resistance. The voltage is measured twice while keeping the same current setting. The voltage measurement is done once with the setting on "R_x" and again with the setting on 100Ω. Dividing one V = IR equation by the other (because two measurements are done) and solving for R_x allows one to translate the unknown resistance into a temperature reading based on tabulated values relating resistance and temperature for the CGR. Temperature measurements are performed with a current setting that gives a voltage less than 10 mV. Too much voltage results in self-heating (I^2R Joule heating) and too little voltage results in inaccurate readings. Measurements were taken using as large of a current as available, provided V_x was below 10 mV.

A full manual detailing the experimental setup, including reference documentation, can be found in the Hayes Group laboratory.

2.2 Results and Discussion

Lineshapes observed in ^{13}C NMR spectroscopy of CO_2 gas adsorbed by the MOF structure are indicative of complex molecular motion, including hopping between metal sites and along the 1-dimensional channels of the Mg-MOF-74 structure[9,10]. In this study, we use the ^{13}C NMR line shape, which changes dramatically as a function of loading, temperature, and MOF composition,

as an indicator of the CO_2 behavior. NMR spectroscopy coupled with DFT computations reveal the different types of binding sites of CO_2 that are present under these conditions.

2.2.1 Static Variable CO_2 Loading ^{13}C NMR Studies

Figure 2.6 shows the ^{13}C NMR spectra recorded for $^{13}CO_2$-filled Mg-MOF-74 with gas loadings from 0.88 to 1.15 CO_2 molecules per metal site at 295 K. Low loadings of CO_2 at room temperature (0.88 and 0.91 CO_2 molecules per metal) show a ^{13}C lineshape that exhibits a positive chemical shift anisotropy (CSA) pattern, with the most intense feature on the right side. At intermediate loadings, a symmetric lineshape is found (~0.93 and 1.01 CO_2 molecules per metal, respectively). At higher loadings, the lineshape exhibits a CSA with the most intense feature now on the left (or high frequency) side (~1.06 and 1.15 CO_2 molecules per metal,

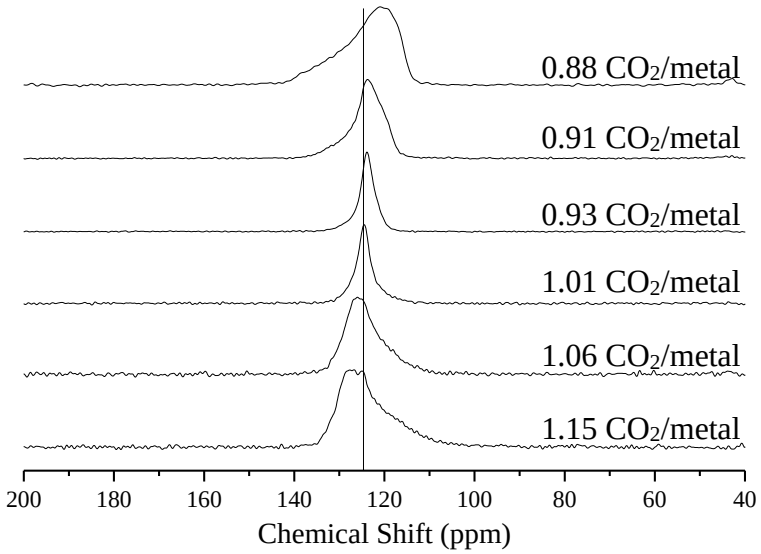

Figure 2.6: Static ^{13}C NMR of Mg-MOF-74 loaded with variable amounts of CO_2 at 295 K; the number of molecules of CO_2 per metal are given on the right side of the diagram. A vertical line is placed at 124.5 ppm to reference the isotropic chemical shift of free CO_2.

respectively). The change in the appearance or "flip" of the lineshape is referred to as an alteration of the sign of the CSA from "positive" to "negative", respectively. This change with respect to loading level is notable, which we will address below. Related lineshapes have been

observed previously for low loading of CO_2. This regime was explored by an NMR study of Mg-MOF-74[9] and found spectra similar to that shown in the top of Figure 2.6 (at 0.88 CO_2/metal loading), whereas we have found no similar study of a highly-loaded Mg-MOF-74.

In order to understand these NMR lineshapes, we must first define several factors related to the NMR chemical shift tensor of ^{13}C (in particular the chemical shift anisotropy or "CSA") that govern their appearance.[28] The MOF-74 samples are powders with the 1-dimensional channels randomly oriented and possessing approximately 6-fold symmetry about the c-axis of the channel. Adsorbed CO_2 molecules can undergo motion that consists of site-to-site hopping around the 6-fold-symmetry metal sites and along the 1-dimensional channel, leading to reorientation of the molecule. The CO_2 molecule stays in the channel for the duration of the acquisition of each NMR signal transient. On the timescale of an NMR experiment (approximately milliseconds), *the motion of CO_2 is not isotropic*. As a result, the ^{13}C NMR spectra in nearly all cases exhibit an "axially-symmetric" chemical shift anisotropy pattern—an asymmetric lineshape that is peaked on one side—found for molecules possessing a 3-fold (or higher) symmetry axis. These lineshapes are important because they add additional detail to the NMR spectroscopy of such gas-phase molecules, and components of the chemical shift tensor can be extracted from lineshapes.

The lineshape permits assignment (using the Haeberlen convention[29]) of three elements of the diagonalized chemical shift tensor. The familiar isotropic chemical shift, δ_{iso}, which is often reported in solid-state magic-angle spinning, and solution-phase NMR comes from the average of all three tensor elements, δ_{xx}, δ_{yy}, and δ_{zz}. Significant for our purposes here, the **sign** of the CSA lineshape is determined from the "reduced anisotropy" $\delta = \delta_{zz} - \delta_{iso}$, where δ_{zz} is the principal component of the tensor furthest away from the isotropic chemical shift, δ_{iso}.

As an aside, in NMR two values are often reported interchangeably[30]: σ, chemical shielding (a tensor) and δ, the chemical shift (which also can be expressed as a tensor). They are related to one another by using a chemical reference scale, where $\delta=(\sigma_{ref}-\sigma_{sample})$. We are using the IUPAC convention[31,32] here: chemical shifts (δ) are positive to high frequency, whereas, absolute shieldings (σ) are positive to low frequency. Computational programs that predict NMR parameters (such as Gaussian,[33] CASTEP[34]-NMR) typically give values for σ, whereas experimental data report δ values. Here, we use δ but refer to some aspects of theory that invoke shielding (σ).

Central to this analysis for comparison to NMR lineshapes is the use of the angle θ between the long (C_∞) axis of the CO_2 molecule and the c-axis of the MOF channel. The NMR lineshape measured is an integral over all orientations of CO_2 present, where the spectrum of each CO_2 molecule also has an angular orientation with respect to the external magnetic field (B_o) used for recording NMR spectra. A symmetric Lorentzian NMR resonance arises from isotropic motion among a random distribution of sites, but the symmetry of the MOF structure and CO_2 molecules binding to it encodes the ^{13}C spectra with reduced symmetry of motion along and around the 1-dimensional channels. This lineshape can best be expressed as a modulation of the chemical shielding arising from this θ angular dependence:

$$\Delta\sigma_{eff} = \Delta\sigma \cdot P_2[\cos\theta] = \Delta\sigma \cdot \frac{1}{2}\left(3\overline{cos^2\theta} - 1\right) \quad (2.1)$$

where P_2 is the second-order Legendre polynomial. Equation 2.1 (Ref. [35]) describes the angular dependence of the shielding that governs the spectrum's linewidth and sign (positive or negative). From Equation 2.1, it can be seen when θ is greater than 54.7°, the value of P_2 is

negative and when less than 54.7°, P_2 is positive. Hence, computation of the multiple CO_2 binding sites and their relative orientations can be compared via the NMR lineshapes.

The linewidth of the axially-symmetric spectrum in the rigid lattice limit (|325| ppm,[36] cf. Figure 2.12) is given by the range of chemical shielding $\Delta\sigma$ scaled by P_2 to obtain the effective linewidth, $\Delta\sigma_{\text{eff}}$. Here we express it as an absolute value in order to avoid confusion between its expression as shielding, $\Delta\sigma$, or as chemical shift, $\Delta\delta$. Based on the IUPAC convention (Ref. [31], [32]), these are linearly related and opposite in sign to one another, $\Delta\delta = -\Delta\sigma$.

As discussed above, the ^{13}C lineshapes depend on CO_2 loading (Figure 2.6) and can be interpreted in terms of the site occupancy at each loading level. In the next section, we describe the use of DFT calculations to determine the angle between the instantaneous CO_2 axis and the channel axis, θ, depending on site occupany. We use these calculations to understand the Figure 2.6 ^{13}C NMR lineshapes.

DFT calculations were performed to study the conformations and adsorption energetics of adsorbed CO_2 molecules and the multiple types of adsorption sites that exist for CO_2 as a function of loading in Mg-MOF-74. A multiple-site model of CO_2 loading into MOF-74 has been previously reported by Queen *et al.*, which found existence of primary, secondary, and even tertiary adsorption sites for CO_2 in Cu-MOF-74.[22] This model transferred to Mg-MOF-74 is the starting point for our analysis. In addition, a similar description of CO_2 also based on the data from Queen *et al.*[22] has recently been used by Sillar *et al.*[37] to simulate CO_2 adsorption isotherms in Mg-MOF-74 using first principles calculations; their results are consistent with our findings in this work. Previous studies[9,10] have also addressed Monte Carlo simulations of low

loading of CO_2 at less than one gas molecule per metal to determine equilibrium configurations, and the resulting effect on ^{13}C NMR resonances.

Calculated binding energies with several CO_2 loading levels from 0.17 to 2.17 CO_2 molecules per open metal site are given in Table 2.2. Binding energies were computed using equation 2.2:

$$-BE_{CO_2} = E_{MOF+\mathrm{N}\times CO_2} - E_{MOF+(\mathrm{N}-1)\times CO_2} - E_{CO_2} \quad (2.2)$$

$E_{MOF+\mathrm{N}\times CO_2}$ is the energy of the system when N CO_2 molecules are bound in the MOF, $E_{MOF+(\mathrm{N}-1)\times CO_2}$ is the energy of the MOF with one fewer CO_2 molecule bound within it, and E_{CO_2} is the energy of the isolated CO_2 molecule. We differentiate between CO_2 molecules at primary, secondary, and tertiary sites and consider the energy per molecule, treating all molecules at each type of site as equivalent for purposes of deducing the binding energy of a single CO_2 molecule. These binding energies assume pairwise interactions between adsorbed CO_2 molecules. As expected, the data indicate that once all primary adsorption sites are occupied, successive occupation of secondary and tertiary sites show progressively decreasing strengths of adsorption as CO_2 loads into the Mg-MOF-74 pore channel. We discuss more about the energetics of successive loading of binding sites with our discussion of the geometry of the adsorbed molecules in the following sections.

Table 2.2: Calculated (DFT, PBE-D3) binding energies (kJ/mol) for the different positions of CO_2 at the primary and secondary binding sites, and binding energies for all three sites as a function of CO_2 loading. The loading level assumes CO_2 occupies the most energetically favorable sites before populating less energetically favorable sites and uses as a reference the 6 CO_2 case for the energy of fully occupied primary adsorption sites and 12 CO_2 for the energy of fully occupied secondary adsorption sites.

	Total BE (kJ/mol)	Primary BE per CO_2	Secondary BE per CO_2	Tertiary BE
Mg-MOF-74 + CO_2 – Position 1	35.7	35.7	-	-
Mg-MOF-74 + CO_2 – Position 2	40.0	40.0	-	-
Mg-MOF-74 + CO_2 – Position 3	35.5	35.5	-	-
Mg-MOF-74 + CO_2 – Position 4	40.8	40.8	-	-
Mg-MOF-74 + $2CO_2$	82.7	41.3	-	-
Mg-MOF-74 + $3CO_2$	125.7	41.9	-	-
Mg-MOF-74 + $6CO_2$	255.0	42.5	-	-
Mg-MOF-74 + $7CO_2$	289.6	42.5	34.5	-
Mg-MOF-74 + $9CO_2$	355.5	42.5	33.5	-
Mg-MOF-74 + $12CO_2$	376.0	42.5	20.2	-
Mg-MOF-74 + $13CO_2$	391.9	42.5	20.2	15.9

At low loadings, CO_2 is likely to spend the most time at the open metal binding site, referred to as the "primary" binding site and depicted in Figure 2.7, based on its calculated binding energy. Figure 2.7 shows the most favorable binding position of CO_2 (superimposed onto the figure) at

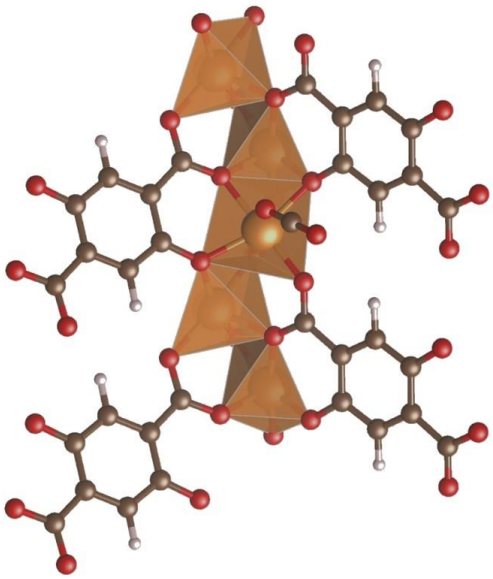

Figure 2.7: CO_2 binding at the most favorable primary binding site (position 4) in Mg-MOF-74 in the low loading limit.

the open metal site at low loadings of CO_2. The four most favorable binding positions at the open metal site, with the corresponding binding energies, can be found below in Figure 2.8.

Notably, a favorable lateral neighbor interaction of about 1 kJ/mol is observed between CO_2 molecules in neighboring primary adsorption sites, meaning that neighboring sites are slightly favored to fill first. This is consistent with the observation of a favorable lateral CO_2—CO_2 interaction by Sillar *et al*.[37] We note that the lower magnitude of our estimate can be attributed

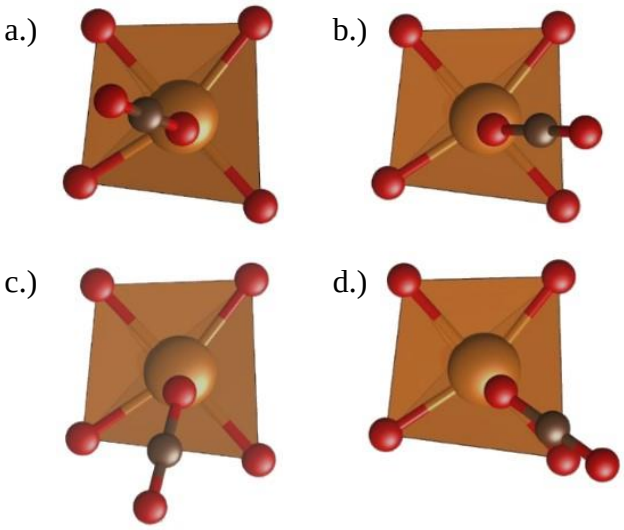

Figure 2.8: A depiction of the four most likely (based on energy) positions for CO_2 to adopt when it binds to the open metal site with the following binding energies a.) BE = 35.7 kJ/mol, position 1 b.) BE = 40.0 kJ/mol, position 2 c.) BE = 35.5 kJ/mol, position 3 d.) BE = 40.8 kJ/mol, position 4. Position labels are the same as in Figure 2.2b.

to our model implicitly including neighbors along the c-axis of the channel as a result of using the primitive unit cell in our simulations, making it impossible for us to fully eliminate interactions from nearest-neighbor CO_2 molecules.

At higher loadings, the sites sampled are similar to those shown in Figure 2.9. These include "secondary" sites at which CO_2 coordinates predominantly to other molecules of already-adsorbed CO_2 at primary sites, as well as to the organic DOBDC linker. In contrast to primary sites, secondary sites do not exhibit a significant nearest-neighbor interaction, the result of reduced intermolecular distance, and therefore secondary sites are favored to fill in a disperse fashion. At the highest loading levels, tertiary sites are found to exist at the pore center aligned with the channel axis. The energetics of binding at these sites are given in Table 2.2.

What we find is a dynamic situation where the CO_2 molecules are moving from site to site on the NMR timescale, the reciprocal of the linewidth (on the order of 1 ms). The P_2 value obtained

from NMR reflects an averaging process; separate spectra are not observed for each kind of site (primary, secondary, or tertiary), rather a single time-averaged value of P_2 results.

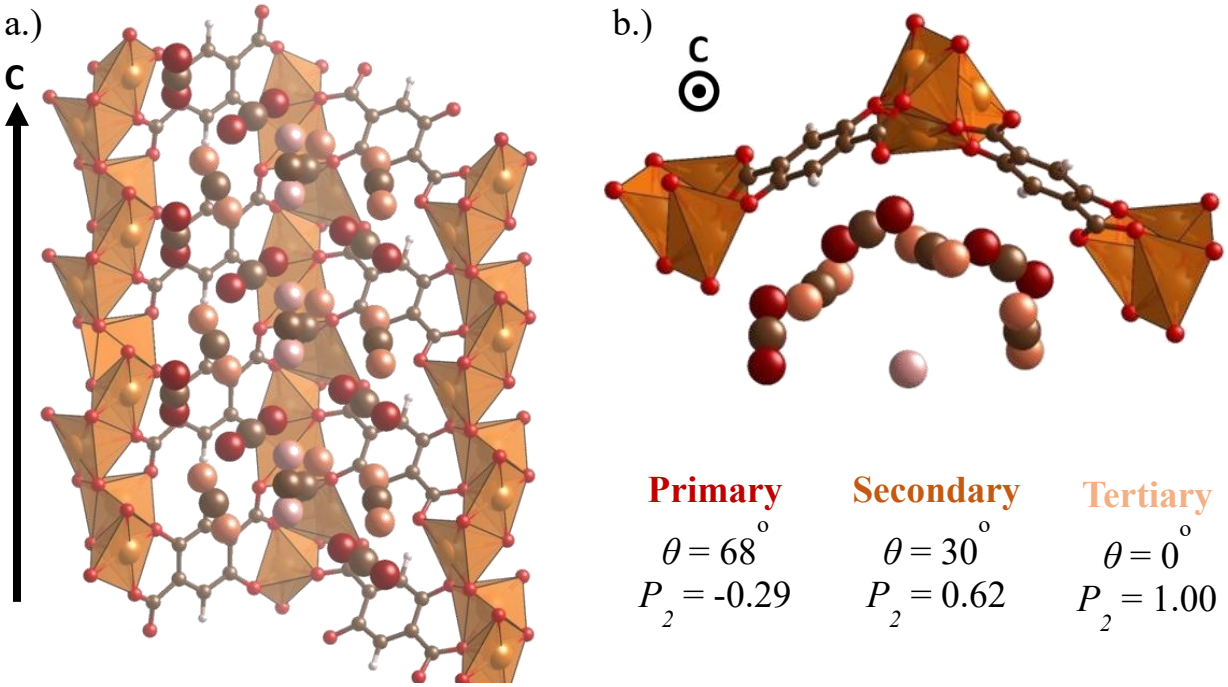

Figure 2.9: a.) Cross section along the c-axis of Mg-MOF-74 loaded with CO_2, showing primary (metal-associated), secondary (CO_2- and linker-associated), and tertiary (channel-center CO_2-associated) sites b.) Cross section looking down the c-axis of Mg-MOF-74 loaded with CO_2. θ designates the orientation of the long axis of the CO_2 species with respect to the c-axis of the channel. P_2 is the calculated value from the orientation (that affect the measured ^{13}C CSA) from the different sites. These individual molecule contributions to P_2 are used to calculate weighted P_2 values.

DFT is able to predict a weighted P_2 value based on the occupancy and orientation of primary, secondary, and tertiary sites as a function of CO_2 loading. This value is expressed in terms of the "number of CO_2 molecules per metal", which is graphed in Figure 2.10a. The manifestation of P_2 in the NMR spectra in Figure 2.6 are in agreement with the trend for P_2 predicted by DFT calculations shown in Figure 2.10a, where a weighted P_2 was calculated based on the number of CO_2 molecules at each site and their orientations relative to the c-axis of the unit cell. As CO_2 loads into the MOF-74 unit cell, initially the open metal sites serve as the primary adsorption

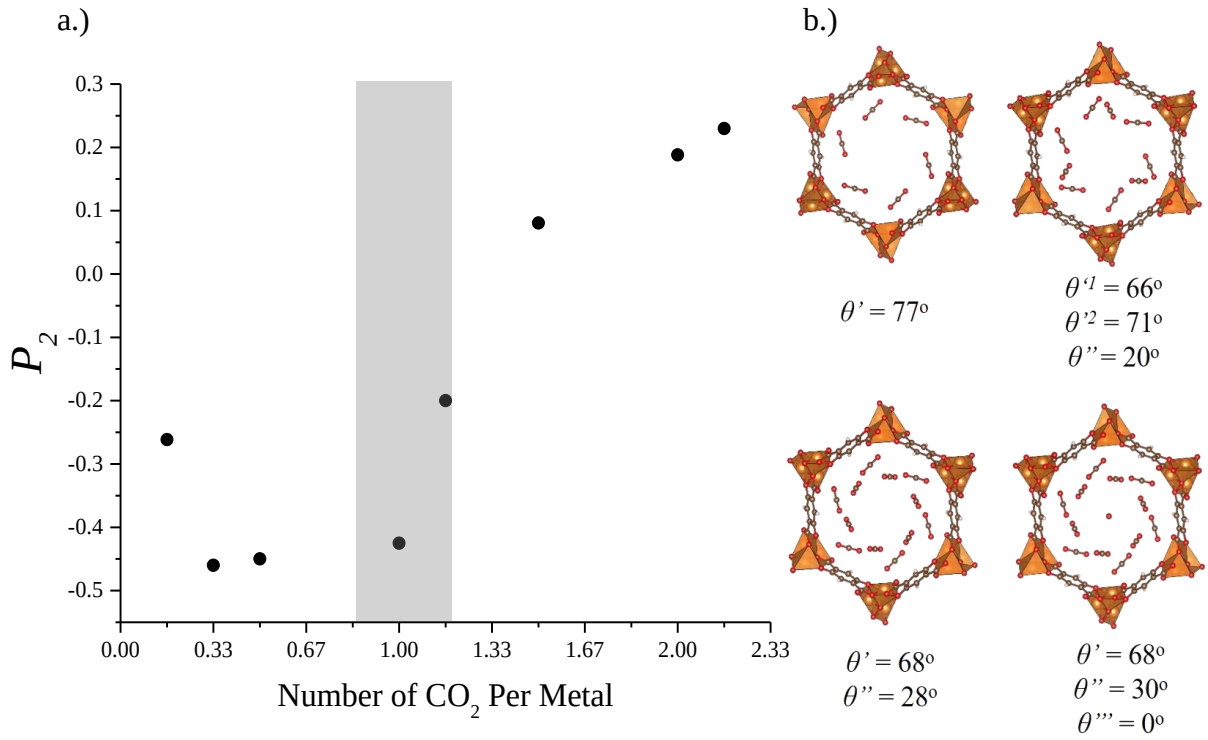

Figure 2.10: a.) Weighted average of CO_2 loading dependence on the second order Legendre polynomial, P_2. The shaded region shows the CO_2 loading levels measured in Figure 2. b.) CO_2 loadings in Mg-MOF-74 unit cell, corresponding to the calculated P_2 values in part a.). θ' is the Primary site, θ'' is the Secondary site, θ''' is the Tertiary site, and θ'^1 and θ'^2 are to distinguish two orientations observed at the Primary site when some Secondary sites occupied.

site–up to 1 CO_2 molecules per metal occupy such sites, shown in Figure 2.10b (upper left image). These primary sites exhibit a negative P_2 and are consistent with the low loading spectra in Figure 2.3 (θ' = 67° to 77° is predicted). This change from 67° to 77° (a tilting of CO_2 away from aligning with the c-axis) is a result of the introduction of a favorable lateral CO_2—CO_2 interaction which has also been noted by Sillar *et al.*[37] Shown in Figure 2.10a, negative P_2 values are predicted up through 1.17 CO_2 molecules per metal.

Once the primary adsorption sites (the open metal sites) are occupied, the secondary binding sites that exist through coordination to the DOBDC linker and the bound CO_2 molecules will become occupied with increasing CO_2 loading. These sites may break the symmetry of the primary sites when they are partially occupied as in Figure 2.10b (upper right image), resulting

in different binding modes of neighboring CO_2 molecules at primary adsorption sites (θ' = 66°, 71°). In both cases, the CO_2 molecules at primary adsorption sites are more aligned with the c-axis of the MOF channel than when there are no secondary sites are occupied. This effect is compounded by the CO_2 adsorbed at the secondary binding sites (θ'' = 20°) being aligned with the pore channel relative to CO_2 at primary binding sites. The change in orientation of already adsorbed CO_2 molecules and the occupation of channel-aligned sites results in a transition from a negative to a positive weighted P_2 value.

With further loading, once all of the secondary adsorption sites become occupied (there are six such sites, shown in Figure 2.10b in the lower left image) all of the primary sites are again equivalent by symmetry (θ' = 68°), as are the secondary sites (θ' = 28°). The increased occupation of channel-aligned secondary sites further increases the weighted P_2 value. The tertiary site at the channel center found at high loading is aligned with the pore channel (θ = 0°), giving the maximum (positive) P_2 value (1.00), and shown schematically in Figure 2.10b, lower right.

We note that the transition from a negative to a positive P_2 value — indicated by both the experimentally measured lineshape and the DFT-predicted structures — occurs around a loading of one CO_2 molecule per metal site in both cases, although by experiment this transition occurs at slightly lower loading than we predict using DFT. A P_2 value of zero results in a narrower symmetric resonance, observed at intermediate loadings (0.93 – 1.01 CO_2/metal) in Figure 2.6. The loading levels over which we observe a transition from negative to positive are also broader (a less sharp transition) in theory than experiment. We attribute these differences to thermal disorder of bound CO_2 molecules and the dynamic sampling of some secondary sites at loadings below one CO_2 per metal. We note that we have determined our estimates of experimental CO_2

loading from experimentally measured adsorption isotherms, so any uncertainty in those isotherms will directly translate to uncertainty in our estimates of loading.

2.2.2 Static Variable Temperature ^{13}C NMR Studies

Variable temperature ^{13}C NMR was measured to investigate changes to the lineshape on a sample with a high loading of $^{13}CO_2$ (~1.1 molecules of CO_2/metal). There are three regimes to consider: a low temperature regime where the CO_2 is immobile, an intermediate regime where the CO_2 motion is on the order of the NMR timescale (during the data acquisition), and the high temperature (fast motion) regime where the gas molecule is able to dynamically sample available binding sites. These regimes all exhibit different lineshapes, and the fast motion regime will be discussed first. The fast motion regime (at higher temperatures) has been introduced above in the context of multiple loading levels. At 295 K there is evidence of unbound CO_2, seen as an isotropic narrow Lorentzian CO_2 gas peak at 124.5 ppm overlapping another lineshape with a characteristic axially-symmetric CSA pattern (see Figure 2.11, bottom right spectrum, labelled

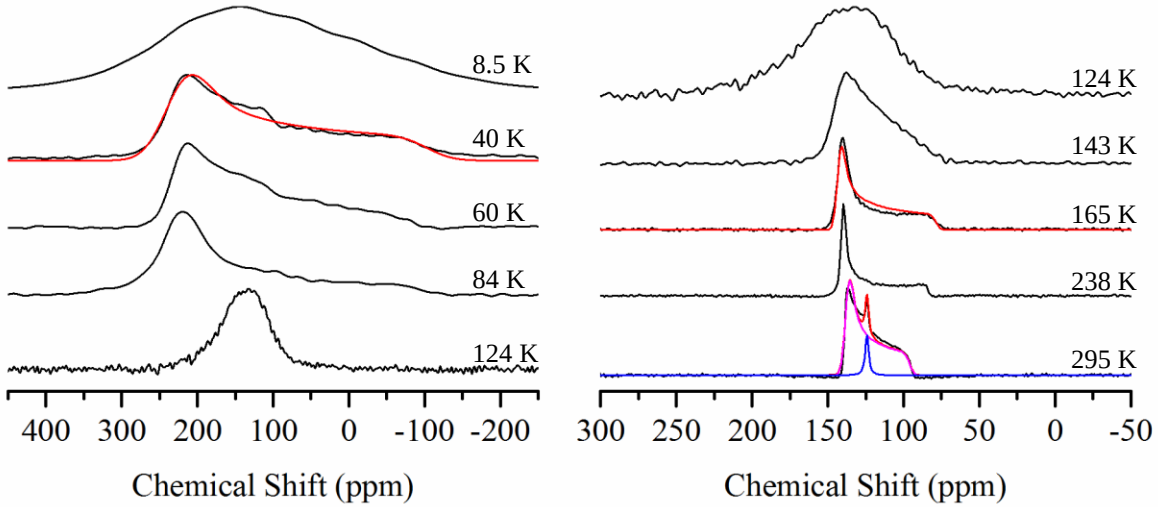

Figure 2.11: Static variable temperature ^{13}C NMR spectra of Mg-MOF-74 loaded with 1.1 molecules of $^{13}CO_2$ per metal site. Spectra were recorded at the indicated temperatures ranging from 8.5 to 295 K. Individual fits are in blue and magenta, and the sum of the fits are shown in red. Note the difference in chemical shift scale, between left and right sides.

"295 K"). The CSA pattern "flipping" (where the CSA changes sign from negative to positive) reported previously in related studies[9,10] is not observed in this highly CO_2-loaded Mg-MOF-74 sample as we change temperatures. We have confirmed that this finding is sensitive to the CO_2 loading by reproducing the findings in the earlier work[9,10], at a lower loading of CO_2 in a separate set of experiments (Figure 2.12), which finds the expected effects (note the appearance of the 295K lineshape). Here, in this analysis of high loadings of CO_2, the molecules are more crowded in the channels and adopt an orientation resulting in a positive P_2 value, in agreement with the schematic picture provided by DFT calculations shown in Figure 2.10. As we cool the sample, the persistence of the axially-symmetric pattern shows that the origin of broadening is

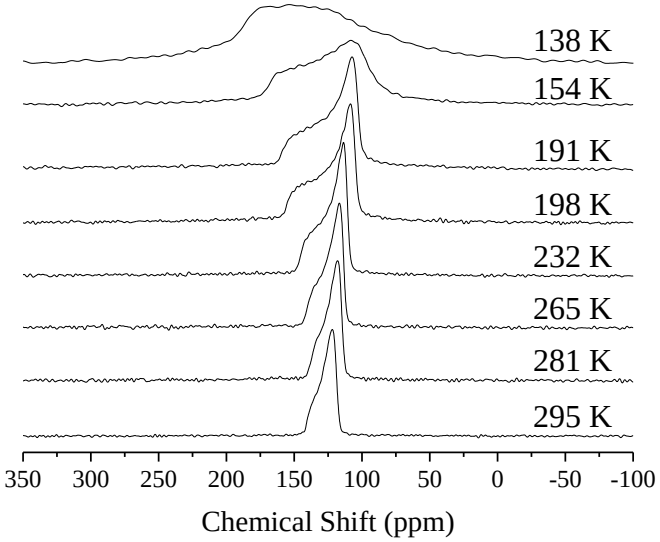

Figure 2.12: Variable temperature ^{13}C NMR of Mg-MOF-74 loaded with 0.2 atm of $^{13}CO_2$. At higher temperatures the sample exhibits a positive CSA lineshape. At the lowest temperature, it is evident that the CSA lineshape has "flipped" and begins to exhibit a negative CSA.

dominantly chemical shift anisotropy.

At this level of (high) loading, an isotropically-averaged narrow resonance is seen at the center of the room temperature spectrum, likely from CO_2 gas that is outside of the 1-dimensional channels of the MOF structure, such as the interparticle spaces in the powder where it is not in

exchange with other sites at the metal centers filling the channel. The spectral lineshapes were modelled using the Dmfit program[38], and an asymmetry parameter of zero ($\eta = 0$) consistent with an axially-symmetric CSA was used for all lineshapes (unless indicated otherwise). Notably, all isotropic chemical shifts (extracted from fits to each of the lineshapes) are approximately 124.5 ± 2 ppm, which is the isotropic chemical shift of free CO_2 gas.[39]

CO_2 motion over a wide range of temperatures is evident from the narrowing of the CSA pattern from 143 to 295 K. If the CO_2 hopping was arrested at any point in this range (from oversaturation of CO_2 on the most favorable sites), lacking any exchange at these higher temperatures, we would expect to see broad lineshapes like those observed at and below 60 K (shown in Figure 2.11).

At 143 K in Figure 2.11, the start of a transitional regime is evident as the sample is cooled further. As the temperature continues to decrease, the sample enters a regime where CO_2 hopping is a rare event on the NMR timescale.[10] At 124 K, the signal-to-noise ratio is noticeably worse than that of other spectra, despite the fact that more scans (number of transients) were acquired at this temperature. Such attenuation of the signal occurs because the correlation time of the CO_2 motion is on the order of the NMR pulse sequence spin echo delay time—here 180 μs. Thus, at the start of the acquisition, the CO_2 molecule is likely to be positioned on one site, and at the end of the acquisition on a different site, thereby changing both its orientation and its frequency, resulting in imperfect refocusing of the magnetization.

Cooling the sample further, the CSA lineshape becomes much broader, approximately 320 ppm wide. At these temperatures (≤ 84 K), most of the CO_2 molecules remain on a single site during NMR acquisition. At very low temperatures (in Figure 2.11, 84 K and lower), the linewidth of

the axially-symmetric powder pattern is unchanging, even though the spectral features are slightly broadened. These low-temperature conditions lead to the powder pattern observed here, similar in linewidth and appearance to that of fixed CO_2 in the solid (325 ppm), the rigid lattice linewidth.[36]

Notably, at 8.5 K (the lowest temperature studied) the carbon resonance becomes broad and featureless. The origin of the broadening is due to paramagnetic sites in the host that become more aligned by the magnetic field at low temperature and therefore interact more strongly with the nearby $^{13}CO_2$ molecules, leading to such a broadened, distorted resonance. An electron paramagnetic resonance (EPR) measurement of Mg-MOF-74 at 10 K confirms that paramagnetism is present at low temperatures (Figure 2.13). Paramagnetism is important to note because it can cause NMR signals to broaden or shift—so acknowledgement of an unsaturated electron in Mg-MOF-74 is chemically interesting to note.

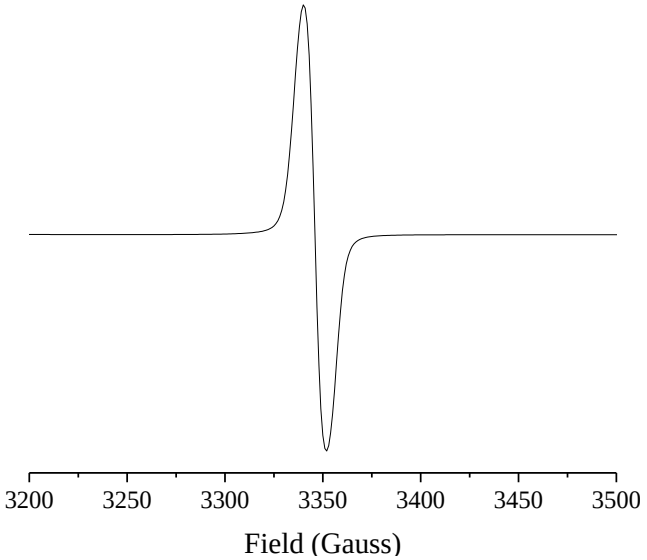

Figure 2.13: Mg-MOF-74 EPR spectrum recorded on a Bruker EMX-PLUS EPR at X-band (~9.38 GHz) frequency at 10 K. This resonance (g = 2.00256) is similar to that of a free electron (g ≈ 2.00232).

Similar VT ^{13}C NMR experiments were performed on the mixed-metal MOF-74 ($Mg_{0.77}$—$Cd_{0.23}$-MOF-74). Static VT ^{13}C NMR spectra loaded with 1 atm (at 295 K) of $^{13}CO_2$ were recorded,

from 9.5–295 K (shown in Figure 2.14). A loading of 1 atm for $Mg_{0.77}$—$Cd_{0.23}$-MOF-74 corresponds to approximately 1.00 CO_2 per metal site, based on isotherm data (Figure 2.4).

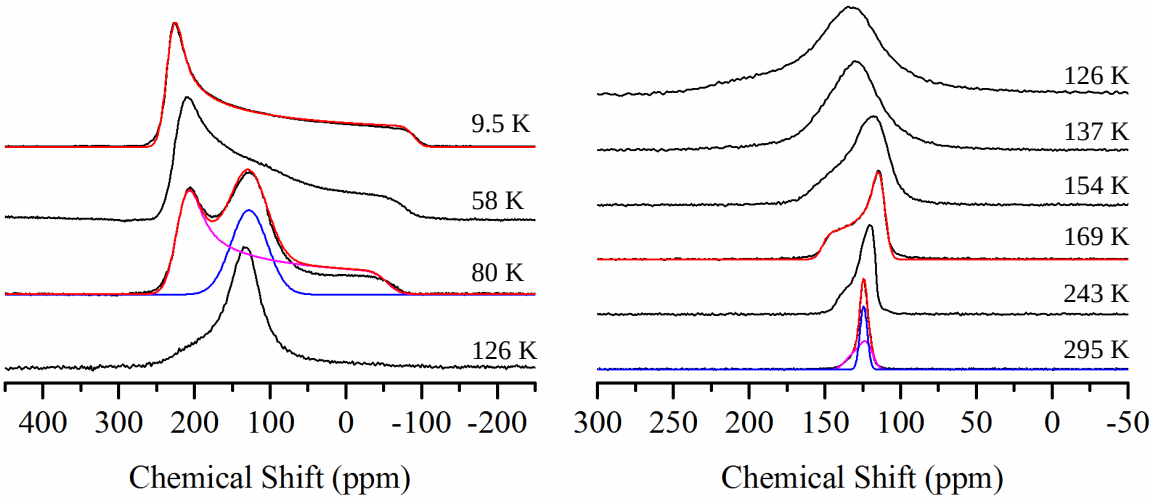

Figure 2.14: Static variable temperature ^{13}C NMR spectra of $Mg_{0.77}$-$Cd_{0.23}$-MOF-74 loaded with 1.00 molecules of $^{13}CO_2$ per metal site. Spectra were recorded at temperatures ranging from 9.5 to 295 K. Individual fits are in blue and magenta, and the sum of the fits are shown in red. Note the difference in chemical shift scale between left and right sides.

Figure 2.14 shows several ^{13}C spectra with axially-symmetric CSA lineshapes that change from a positive to a negative CSA pattern when going from high to low temperatures, respectively, *even with high loading of CO_2*, in contrast to the Mg-MOF-74 findings. The reversal ("flipping") of the most intense portion of the CSA powder pattern from one side to another is due to the change in favored orientation(s) of the CO_2 molecules relative to the c-axis of the MOF-74 host, similar to that found in low-loading Mg-MOF-74. The Mg sites have a stronger affinity for CO_2 than the Cd sites, evidenced by the isotherm data and density functional theory (DFT) calculations[22]. With nearly 1 in 4 metal sites being Cd, this composition with multiple metal sites gives CO_2 the opportunity on average to align with a negative P_2, tending toward a direction orthogonal to the c-axis. The results from Mg-MOF-74 under different loading permit us to intuit the behavior. The Cd sites, with their weaker binding of CO_2, would appear to permit the primary binding at Mg metal sites to dominate the observed binding, lessening the influence of secondary sites.

At 295 K the lineshape can be deconvoluted into two resonances: one with a CSA lineshape and one Lorentzian. In Figure 2.14, we can see that there is a significant increase in the breadth of the CSA lineshape when cooling the sample from approximately 140 to 100 K. This is the transitional regime as seen previously, where CO_2 exits the fast motion regime of hopping from site-to-site (> 140 K), and enters a regime of hindered motion (< 100 K), on the NMR timescale. At these lower temperatures in $Mg_{0.77}$—$Cd_{0.23}$-MOF-74, there is evidence at 80 K for two types of CO_2. There are CO_2 molecules contributing to the CSA-broadened powder pattern, as well as CO_2 with a Gaussian-shaped resonance, likely due to motion, which would match the reduced binding affinity offered by Cd sites. As temperature is decreased from 80 K, the CSA line width continues to broaden, and the broad Gaussian is no longer evident by 9.5 K. The span of the lineshape at 9.5 K exceeds 300 ppm, which is similar to that of solid CO_2,[36] and no evidence of broadening from interaction with paramagnetic sites was found, in contrast the pure Mg-MOF-74. The absense of such paramagnetism would be a wothwhile future study; how additional metals can prevent formation of paramagnetism.

In the higher temperature range, both types of MOF structures have similar line-narrowing changes with respect to temperature, even if one set ($Mg_{0.77}$—$Cd_{0.23}$-MOF-74) has a narrower linewidth (see Figure 2.14). At the lowest temperatures, the linewidth for CO_2 in Mg-MOF-74 is unchanging, indicating CO_2 is not moving (on the NMR timescale). In contrast, the mixed-metal $Mg_{0.77}$—$Cd_{0.23}$-MOF-74 is still undergoing line narrowing even in this low temperature regime, noting that the $^{13}CO_2$ linewidth converges to the same value at the lowest temperature recorded for the mixed-metal MOF.

2.2.3 Conclusions

The combination of NMR with DFT confirms the sensitivity of the NMR lineshape with respect to small changes in molecular orientations. CO_2 adsorbed in the MOF-74 structure is in exchange between multiple sites and has an orientational dependence dictated by the number of CO_2 molecules present in the channels (expressed as CO_2 per metal site. The molecules undergo a transition from aligning (on average) normal to the pore channel axis at low loading, to aligning with the pore channel axis upon higher loading. This phenomenon manifests in the ^{13}C NMR lineshape, wherein the CSA pattern "flips" sign from negative to positive between low and high loadings of CO_2, undergoing this transition roughly at 1 CO_2 per open metal site.

DFT calculations show that the orientation of the long axis of these molecules can be calculated as a function of loading, expressed as a value of P_2 that depends upon the angle θ with respect to the channel axis. The weighted P_2 value agrees with experimental data in the fast motion regime, showing that the occupation of secondary CO_2 adsorption sites plays a key role in affecting the structure of adsorbed CO_2 and the flip of the CSA lineshape. This finding, coupled with previous work on low CO_2 loadings, has enabled newly emergent insight into the importance of CO_2 loading in understanding qualitatively the evolution of the CSA lineshape with temperature in Mg-MOF-74.

In Mg—Cd-MOF-74, we observe different behavior at high loading and in the fast motion regime. Due to differences in CO_2 loading, the CSA lineshape for Mg—Cd-MOF-74 loaded with CO_2 is reversed in sign relative to that of pure Mg-MOF-74. This change in sign from a lower loading causes CO_2 to adopt an orientation, on average, where the CO_2 molecules align orthogonally to the channel axis. Notably, paramagnetism is absent in this mixed-metal framework. A second metal site, even at only 20% affects the CO_2 behavior in ways not

predicted by current models. This finding will stimulate additional studies into the influence of mixed-metals on structure and performance.

What is of particular significance is the demonstration in this work that NMR coupled with DFT is able to reveal, through lineshape analysis, the binding sites of CO_2, not only to the metals but also secondary and tertiary sites that are present. NMR can therefore provide such unique insights into the behavior of adsorbates in porous materials.

References

[1] K. Jiang, L. Zhang, Q. Hu, Y. Yang, W. Lin, Y. Cui, Y. Yang, G. Qian, A biocompatible Ti-based metal-organic framework for pH responsive drug delivery, Mater. Lett. 225 (2018) 142–144.

[2] T. Simon-Yarza, A. Mielcarek, P. Couvreur, C. Serre, Nanoparticles of Metal-Organic Frameworks : On the Road to In Vivo Efficacy in Biomedicine, Adv. Mater. (2018) 1–15. doi:10.1002/adma.201707365.

[3] Z.R. Herm, R. Krishna, J.R. Long, Reprint of: CO_2/CH_4,CH_4/H_2 and $CO_2/CH_4/H_2$ separations at high pressures using Mg_2(dobdc), Microporous Mesoporous Mater. 157 (2012) 94–100.

[4] B. Mu, F. Li, Y. Huang, K.S. Walton, Breathing effects of CO_2 adsorption on a flexible 3D lanthanide metal–organic framework, J. Mater. Chem. 22 (2012) 10172–10178. doi:10.1039/c2jm15721g.

[5] K.S. Walton, A.R. Millward, D. Dubbeldam, H. Frost, J.J. Low, O.M. Yaghi, R.Q. Snurr, Understanding inflections and steps in carbon dioxide adsorption isotherms in metal-organic frameworks, J. Am. Chem. Soc. 130 (2008) 406–407. doi:10.1021/ja076595g.

[6] N.C. Burtch, H. Jasuja, D. Dubbeldam, K.S. Walton, Molecular-level Insight into Unusual Low Pressure CO_2 Affinity in Pillared Metal − Organic Frameworks, J. Am. Chem. Soc. 135 (2013) 7172--7180. doi:10.1021/ja310770c.

[7] Y. Jiao, C.R. Morelock, N.C. Burtch, W.P. Mounfield, J.T. Hungerford, K.S. Walton, Tuning the Kinetic Water Stability and Adsorption Interactions of Mg-MOF-74 by Partial Substitution with Co or Ni, Ind. Eng. Chem. Res. 54 (2015) 12408–12414. doi:10.1021/acs.iecr.5b03843.

[8] J. Liu, Y. Wang, A.I. Benin, P. Jakubczak, R.R. Willis, M.D. LeVan, CO2/H2O adsorption equilibrium and rates on metal-organic frameworks: HKUST-1 and Ni/DOBDC, Langmuir. 26 (2010) 14301–14307. doi:10.1021/la102359q.

[9] X. Kong, E. Scott, W. Ding, J.A. Mason, J.R. Long, J.A. Reimer, CO_2 Dynamics in a Metal − Organic Framework with Open Metal Sites, J. Am. Chem. Soc. 134 (2012) 14341−14344. doi:10.1021/ja306822p.

[10] L.C. Lin, J. Kim, X. Kong, E. Scott, T.M. McDonald, J.R. Long, J.A. Reimer, B. Smit, Understanding CO_2 Dynamics in Metal-Organic Frameworks with Open Metal Sites, Angew. Chemie - Int. Ed. 52 (2013) 4410–4413. doi:10.1002/anie.201300446.

[11] A.O. Yazaydin, R.Q. Snurr, T.-H. Park, K. Koh, J. Liu, M.D. LeVan, A.I. Benin, P. Jakubczak, M. Lanuza, D.B. Galloway, J.J. Low, R.R. Willis, Screening of Metal - Organic Frameworks for Carbon Dioxide Capture from Flue Gas Using a Combined Experimental and Modeling Approach, J. Am. Chem. Soc. 131 (2009) 18198–18199.

[12] A.R. Millward, O.M. Yaghi, Metal Organic Frameworks with Exceptionally High Capacity for Storage of Carbon Dioxide at Room Temperature, J. Am. Chem. Soc. 127 (2005) 17998–17999. doi:doi:10.1021/ja0570032.

[13] P.D.C. Dietzel, V. Besikiotis, R. Blom, Application of metal – organic frameworks with coordinatively unsaturated metal sites in storage and separation of methane and carbon dioxide †, J. Mater. Chem. 19 (2009) 7362–7370. doi:10.1039/b911242a.

[14] H. Wu, W. Zhou, T. Yildirim, High-Capacity Methane Storage in Metal - Organic Frameworks M2(DHTP): The Important Role of Open Metal Sites, J. Am. Chem. Soc. 131 (2009) 4995–5000.

[15] X. Peng, L. Lin, W. Sun, B. Smit, Water Adsorption in Metal – Organic Frameworks with, Am. Inst. Chem. Eng. 61 (2015) 677–687. doi:10.1002/aic.

[16] Y. Zhang, B.E.G. Lucier, M. Fischer, Z. Gan, P.D. Boyle, A Multifaceted Study of Methane Adsorption in Metal – Organic Frameworks by Using Three Complementary Techniques, Chem. Eur. J. 24 (2018) 7866–7881. doi:10.1002/chem.201800424.

[17] T.G. Glover, G.W. Peterson, B.J. Schindler, D. Britt, O. Yaghi, MOF-74 building unit has a direct impact on toxic gas adsorption, Chem. Eng. Sci. 66 (2011) 163–170. doi:10.1016/j.ces.2010.10.002.

[18] G. Kresse, D. Joubert, From Ultrasoft Pseudopotentials to the Projector Augmented-Wave Method, Phys. Rev. B Condens. Matter Mater. Phys. 59 (1999) 1758–1775.

[19] P.E. Blochl, Projector Augmented-Wave Method, Phys. Rev. B Condens. Matter. 50 (1994) 17953–17979.

[20] J.P. Perdew, K. Burke, M. Ernzerhof, Generalized Gradient Approximation Made Simple,

Phys. Rev. Lett. 77 (1996) 3865–3868.

[21] S. Grimme, J. Antony, S. Ehrlich, H. Krieg, A consistent and accurate ab initio parametrization of density functional dispersion correction (DFT-D) for the 94 elements H-Pu, J. Chem. Phys. 132 (2010) 154104. doi:10.1063/1.3382344.

[22] W.L. Queen, M.R. Hudson, E.D. Bloch, J.A. Mason, M.I. Gonzalez, J.S. Lee, D. Gygi, J.D. Howe, K. Lee, T.A. Darwish, M. James, V.K. Peterson, S.J. Teat, B. Smit, J.B. Neaton, J.R. Long, C.M. Brown, Comprehensive study of carbon dioxide adsorption in the metal – organic frameworks M_2(DOBDC) (M = Mg, Mn, Fe, Co, Ni, Cu, Zn), Chem. Sci. 5 (2014) 4569–4581. doi:10.1039/C4SC02064B.

[23] K. Lee, J.D. Howe, L. Lin, B. Smit, J.B. Neaton, Small-Molecule Adsorption in Open-Site Metal − Organic Frameworks: A Systematic Density Functional Theory Study for Rational Design, Chem. Mater. 27 (2015) 668–678. doi:10.1021/cm502760q.

[24] A.C. Kizzie, A.G. Wong-Foy, A.J. Matzger, Effect of humidity on the performance of microporous coordination polymers as adsorbents for CO_2 capture, Langmuir. 27 (2011) 6368–6373. doi:10.1021/la200547k.

[25] P.M. Schoenecker, C.G. Carson, H. Jasuja, C.J.J. Flemming, K.S. Walton, Effect of Water Adsorption on Retention of Structure and Surface Area of Metal – Organic Frameworks Effect of Water Adsorption on Retention of Structure and Surface Area of Metal − Organic Frameworks, Ind. Eng. Chem. Res. 51 (2012) 6513–6519. doi:10.1021/ie202325p.

[26] E.L. Hahn, Spin echoes, Phys. Rev. 80 (1950) 580–594. doi:10.1103/PhysRev.80.580.

[27] E.-K. Jeong, Deuteron NMR of *HD* and D_2 Physically Adsorbed onto *MgO*(100) Surface, Washington University in Saint Louis, 1991.

[28] M.H. Levitt, Spin Dynamics: Basics of Nucear Magnetic Resonance, 2nd ed., John Wiley and Sons, Ltd, 2008.

[29] U. Haeberlen, J.S. Edited by Waugh, Advances in Magnetic Resonance; Suppl. 1, in: Academic Press: New York, 1976.

[30] 2002; pp 219. NMR studies at times have reported contradictory conventions. Here, chemical shifts are reported as positive to high frequency, whereas absolute shieldings are positive to low frequency. This convention is referred to in the text by Malcolm H. Levitt Spin, No Title, n.d.

[31] H. Burrows, R. Weir, J. Stohner, Pure and Applied Chemistry: The Scientific Journal of IUPAC, 1976.

[32] Recommendations for the presentation of NMR data for publication in chemical journals, Int. Union Pure Appl. Chem. 29 (1971) 627–628.

[33] M.J. Frisch, G.W. Trucks, H.B. Schlegel, G.E. Scuseria, M.A. Robb, J.R. Cheeseman, G. Scalmani, V. Barone, G.A. Petersson, H. Nakatsuji, X. Li, M. Caricato, A. V. Marenich, J. Bloino, B.G. Janesko, R. Gomperts, B. Mennucci, H.P. Hratchian, J. V. Ortiz, A.F. Izmaylov, J.L. Sonnenberg, D. Williams-Young, F. Ding, F. Lipparini, F. Egidi, J. Goings,

B. Peng, A. Petrone, T. Henderson, D. Ranasinghe, V.G. Zakrzewski, J. Gao, N. Rega, G. Zheng, W. Liang, M. Hada, M. Ehara, K. Toyota, R. Fukuda, J. Hasegawa, M. Ishida, T. Nakajima, Y. Honda, O. Kitao, H. Nakai, T. Vreven, K. Throssell, J. Montgomery, J. A., J.E. Peralta, F. Ogliaro, M.J. Bearpark, J.J. Heyd, E.N. Brothers, K.N. Kudin, V.N. Staroverov, T.A. Keith, R. Kobayashi, J. Normand, K. Raghavachari, A.P. Rendell, J.C. Burant, S.S. Iyengar, J. Tomasi, M. Cossi, J.M. Millam, M. Klene, C. Adamo, R. Cammi, J.W. Ochterski, R.L. Martin, K. Morokuma, O. Farkas, J.B. Foresman, D.J. Fox, Gaussian, (2013).

[34] S.J. Clark, M.D. Segall, C.J. Pickard, P.J. Hasnip, M.I.J. Probert, Keith Refson, First principles methods using CASTEP, Z. Krist. 220 (2005) 567–570.

[35] M. Mehring, Principles of High Resolution NMR in Solids, Springer-Verlag Berlin Heidelberg New York, 1983.

[36] S. Bin Liu, M.A. Doverspike, M.S. Conradi, Combined translation-rotation jumps in solid carbon dioxide, J. Chem. Phys. 81 (1984) 6064–6068. doi:10.1063/1.447610.

[37] K. Sillar, A. Kundu, J. Sauer, Ab Initio Adsorption Isotherms for Molecules with Lateral Interactions : CO2 in Metal − Organic Frameworks, J. Phys. Chem. C. 121 (2017) 12789–12799. doi:10.1021/acs.jpcc.7b02806.

[38] D. Massiot, F. Fayon, M. Capron, I. King, S. Le Calvé, B. Alonso, J.O. Durand, B. Bujoli, Z. Gan, G. Hoatson, Modelling one- and two-dimensional solid-state NMR spectra, Magn. Reson. Chem. 40 (2002) 70–76. doi:10.1002/mrc.984.

[39] P. V. Kortunov, M. Siskin, L.S. Baugh, D.C. Calabro, In Situ Nuclear Magnetic Resonance Mechanistic Studies of Carbon Dioxide Reactions with Liquid Amines in Non-aqueous Systems: Evidence for the Formation of Carbamic Acids and Zwitterionic Species, Energy and Fuels. 29 (2015) 5940–5966. doi:10.1021/acs.energyfuels.5b00985.

Chapter 3: Characterization of Aluminum Carbide and Related Derivatives

3.1 Characterization of Al_4C_3

With advances in NMR of quadrupolar nuclei, broad overlapping resonances can be separated with the use of high magentic fields (to reduce quadrupolar broadening interactions), high spinning frequencies (to remove multiple interactions that lead to line broadening), and expansion into a second dimension through MQ-MAS[1]. Utilizing MQ-MAS is beneficial, due to the fact that a typical MAS probe with no special modifications can be used to perform this 2-dimensional experiment. Other techniques, such as dynamic-angle spinning (DAS)[2–5], and double-rotation (DOR)[3,5,6], can also assist in the elucidation of resonances, but both require additional hardware. Applications of these methods can reveal quadrupolar broadening differences for individual sites that translate to structural details, a form of what is termed "NMR crystallography."[7] Additionally, deconvolution of complex overlapping resonances can show the presence of impurities and defects that have no long-range order and hence are not evident in X-ray diffraction (XRD).

Here we study aluminum carbide (Al_4C_3), a nonporous crystalline material that is used in diverse applications, such as construction of carbon nanostructures,[8,9] aluminum processing, for strengthening through alloy formation,[10] and as cold electron emmiters when in a 1-dimensional nanowire topology.[11,12] The Al_4C_3 crystal structure has been studied previously by XRD[13–15] and solid-state ^{27}Al NMR.[16] Al_4C_3 has an $R\bar{3}m$ space group and two crystallographically distinct (and magnetically inequivalent) aluminum sites (Figure 3.1a). Each aluminum site is coordinated to four carbon atoms, resulting in a near-tetrahedral geometry

shown in Figure 3.1 along with bond angles and different perspectives of the two sites in Figure 3.1b.

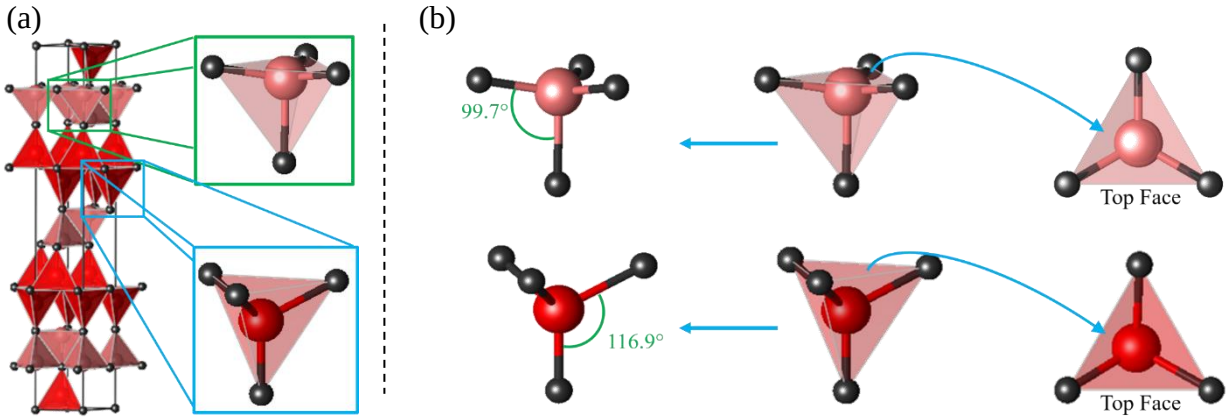

Figure 3.1: (a) Al_4C_3 unit cell with expansions of the two different predicted sites, boxed in green and blue. Dark gray atoms represent carbon sites and the pink/red atoms represent aluminum sites. (b) Depicted are the two sites of the Al_4C_3 crystal structure, where the central atom is Al and the atoms coordinated to the central atom is carbon. On top (pink Al site), the aluminum site is in approximately a trigonal pyramidal geometry and on bottom (red Al site) the aluminum site is in approximately a tetrahedral coordination. Note that the C-Al-C bond angles on the "Top Face" of the sites are all equivalent, respectively for each site.

3.1.1 Materials

Al_4C_3 was purchased from two different suppliers to compare sample variation: Strem Chemicals, Inc. and Zegen Metals & Chemicals, Ltd. Both are brown powdered solids, similar in appearance, and the samples were used as received from the manufacturers. The Al_4C_3 samples were stored in an argon glovebox, since Al_4C_3 can react with water to create alumium hydroxides and methane gas.[17]

3.1.2 NMR Studies

Data acquisition and processing were performed on a Bruker Avance III spectrometer. To ensure quantitative[18] 1-dimensional NMR spectra, a $\pi/18$ flip angle[19] was used in a "pulse-acquire" (Bloch decay) experiment. These measurements were recorded in a 17.6 T magnetic field (^{27}Al Larmor frequency of 195.5 MHz) with a 2.5 mm Bruker probe. Additional Z-filtered ^{27}Al 3Q-

MAS NMR experiments were performed to separate overlapping resonances. Last delays were 2 to 5s, and MAS rotation frequencies ranged from 30 to 46.5 kHz, depending on the experiment. ^{27}Al spectra were referenced to a 1M $Al(NO_3)_3$ solution at 0.0 ppm.

3.1.3 DFT Calculations

First-principles density functional theory (DFT) NMR calculations were performed using CASTEP 2017 software[20] on the Materials Studio platform. These DFT calculations were used to extract quadrupolar coupling constants (C_Q) for the multiple aluminum sites found in Al_4C_3. The NMR-CASTEP code uses gauge-including projector augmented wave (GIPAW) and Perdew-Burke-Ernzerhof (PBE)[21] for electronic correlation effects for the calculation of NMR parameters. A planewave basis set cutoff energy of 440 eV was used for geometry optimized calculations. After geometry optimization, the forces on the atoms were < 0.01 eV/Å.

3.1.4 Results and Discussion

Two samples of Al_4C_3 from different manufacturers were studied in order to examine sample-to-sample variation with the intent to accurately characterize the ^{27}Al tensors. Both samples have experimental powder X-ray diffraction patterns consistent with the simulated pattern of Al_4C_3, confirming the identity of the "bulk" of the samples (Figure 3.2). The 1-dimensional ^{27}Al MAS NMR spectra of each (Figure 3.3) show the presence of compositional differences between

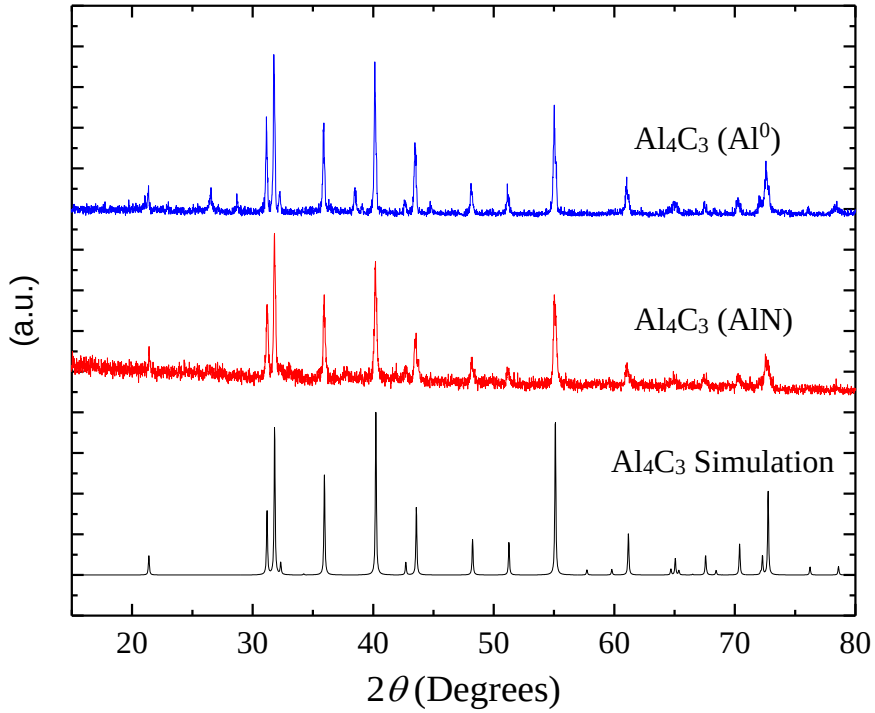

Figure 3.2: Powder X-ray diffraction (PXRD) patterns for Al_4C_3 with the metallic aluminum impurity (blue), with the aluminum nitride impurity (red), and simulation (black).

samples: the Zegen Metals sample has an obvious aluminum metal impurity at 1640 ppm (Figure 3.3, dashed red line), and the Strem Chemicals sample has an aluminum nitride impurity, seen as a very small shoulder on the high frequency side of the broad resonance in the 1-dimensional spectrum spanning approximately 0 to 150 ppm (Figure 3.3, solid black line). For ease of identification, Zegen Metals sample with the metallic aluminum impurity will appear as "Al_4C_3 (Al^0)" and the Strem Chemicals sample with the aluminum nitride impurity will be denoted as

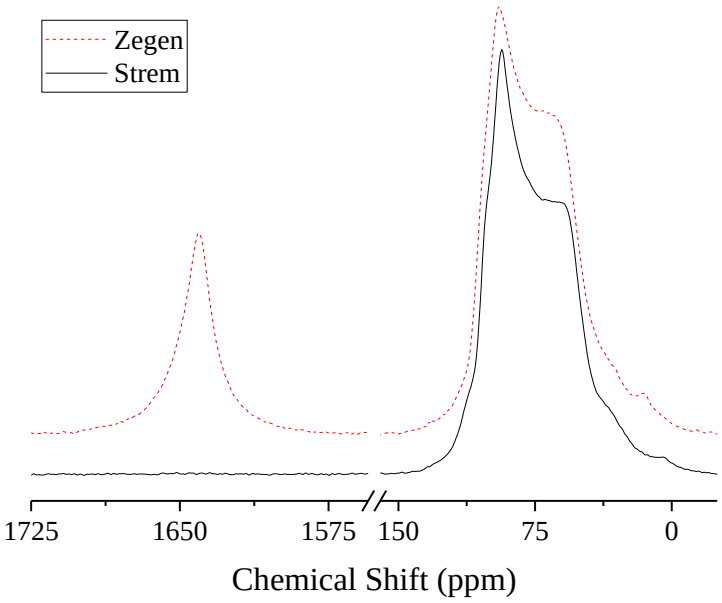

Figure 3.3: ^{27}Al MAS NMR spectra for $Al_4C_3(Al^0)$ (dashed red line) and Al_4C_3(AlN) (solid black line) displayed as expanded regions.

"Al_4C_3 (AlN)." The full spectra for Al_4C_3 (Al^0) and Al_4C_3 (AlN) are shown for reference in Figures 3.4 and 3.5.

Previously, ^{27}Al MAS NMR of Al_4C_3 was measured at a similar 17.6 T magnet field.[16] The resulting spectrum was fit to two magnetically-inequivalent sites, as predicted by the crystal structure.[13–15] Due to ^{27}Al being a quadrupolar nucleus (I = 5/2), ^{27}Al NMR spectra often have broad lineshapes, resulting in overlapping resonances, especially in 1-dimensional spectra.

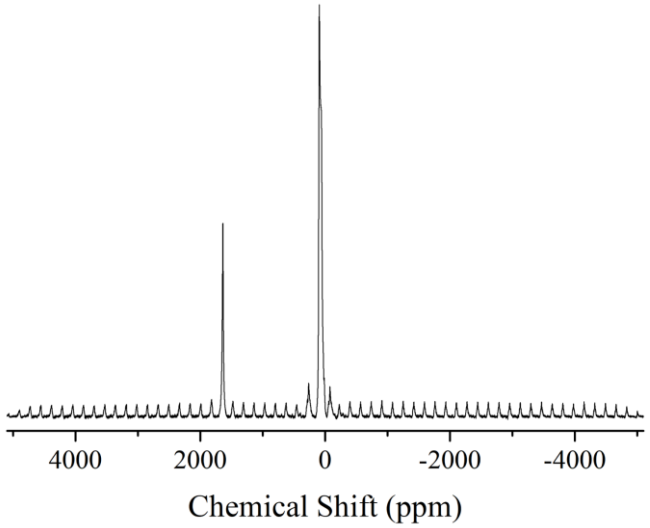

Figure 3.4: Full ^{27}Al MAS NMR spectrum for $Al_4C_3(Al^0)$ at a magnetic field strength of 17.6 T and MAS rate of 33.3 kHz.

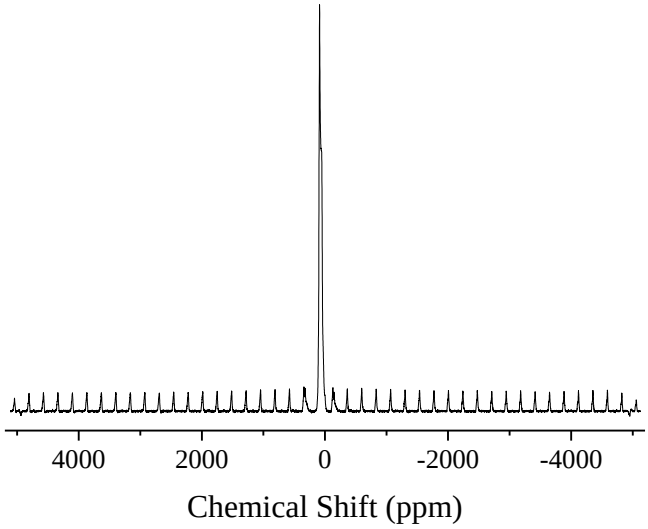

Figure 3.5: Full ^{27}Al MAS NMR spectrum for Al_4C_3 (AlN) at a magnetic field strength of 17.6 T and MAS rate of 46.5 kHz.

These overlapping resonances can make it particularly difficult to accurately deconvolute ^{27}Al NMR spectra and extract important NMR parameters, such as the quadrupolar coupling constant (C_Q), the quadrupolar asymmetry parameter (η_Q), and the isotropic chemical shift (δ_{iso}). Utilizing rapid magic-angle spinning (MAS) NMR, we can average out certain dipolar and first-order quadrupolar interactions. However, second-order quadrupolar effects cannot be completely averaged out, even with fast magic-angle spinning. Undertaking NMR in large magnetic fields

can effectively limit the relative amount of second-order quadrupolar effects that broaden resonances, because C_Q does not scale with magnetic field strength. Yet, even with higher magnetic fields, it can still be difficult to deconvolute spectra when there are multiple sites with large C_Q's.

Consequently, multiple-quantum magic-angle spinning (MQ-MAS) experiments are commonly employed to separate overlapping resonances of quadrupolar nuclei (with non-integer spin number). It is worthwhile to note, for nuclei with C_Q's larger than 8 MHz, the excitation and conversion of the triple quantum coherence can be difficult and inefficient,[22,23] which can result in unrealistic experimental times to record spectra with sufficient signal-to-noise ratios. Using strong radio frequency (RF) fields helps to excite and convert the triple-quantum coherence, which also helps with sensitivity.[24] High RF power combined with the Z-filtered 3Q-MAS sequence,[25] can then separate the overlapping resonances in the isotropic dimension.

In Figure 3.6a and 3.6c are the ^{27}Al 3Q-MAS spectra of the broad peak (spanning ~ 0 to 150 ppm). The two 3Q-MAS spectra shown in Figure 3.6, each show the multiple resonances that overlap to make up the broad peak, permitting deconvolution of the 1-dimensional ^{27}Al MAS spectra. Extracting 1- dimensional slices from the MQ-MAS data (horizontal lines in Figures 3.6a,c) we are able to identify the resonances contributing to the overall lineshape of Al_4C_3 (AlN) and Al_4C_3 (Al^0), shown in Figures 3.6b,d. Referring to the demarcated slices, the two 4-coordinate Al sites of Al_4C_3 are shown in green and blue in the isotropic dimension at approximately 148 and 165 ppm, respectively. There are two additional resonances present that are only elucidated with the help of the 2-dimensional plot, shown in purple at 115-117 ppm and

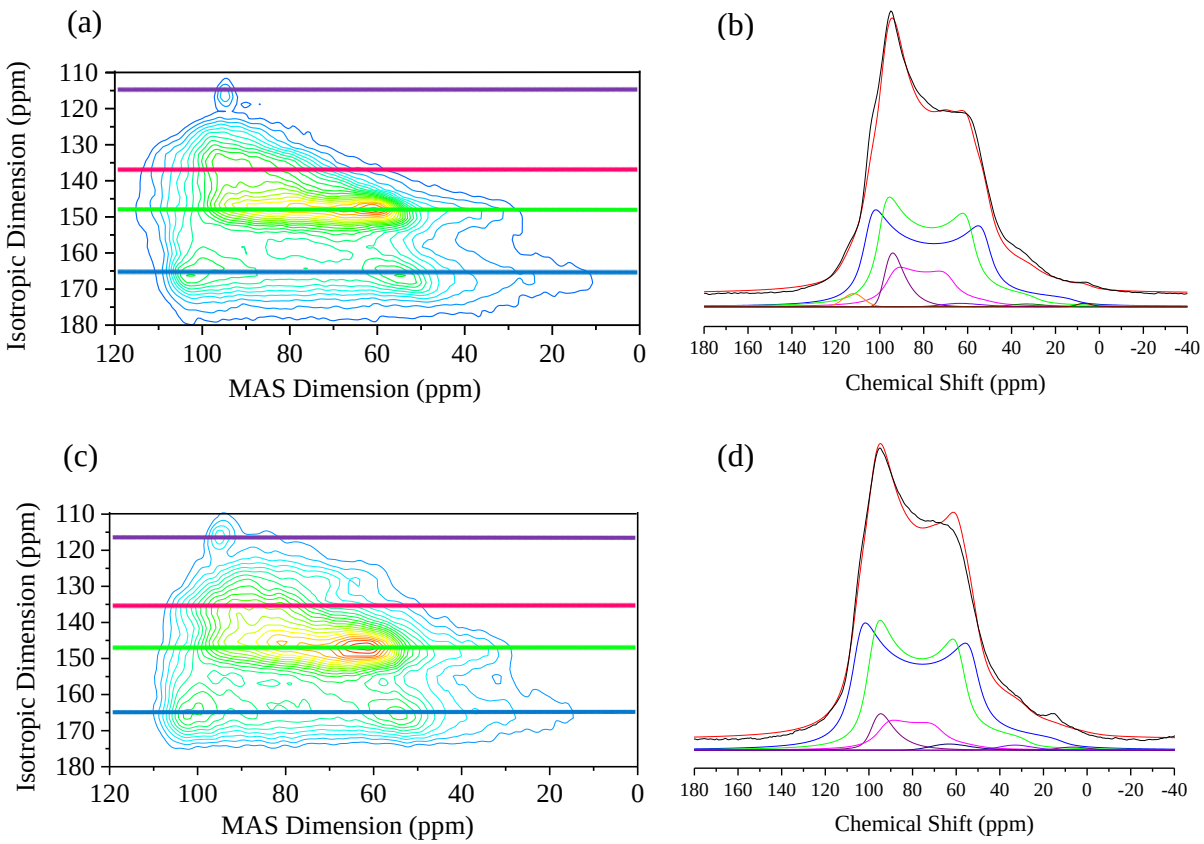

Figure 3.6: ^{27}Al NMR of Z-filtered 3Q-MAS of aluminum carbide (a) with the aluminum nitride impurity and (c) with metallic aluminum impurity. Quantitative 1D ^{27}Al spectra of aluminum carbide (b) with the aluminum nitride impurity and (d) with the metallic aluminum impurity.

magenta at 135-137 ppm (again in the isotropic dimension). These latter two sites have been assigned to aluminum-oxycarbides, as discussed below.

The four slices of the 2-dimensional spectra were modeled using the Dmfit software,[26] to extract initial values of isotropic chemical shifts and quadrupolar coupling constants. Parameters can be found in Table 3.1, along with a comparison to computed values from CASTEP-NMR (DFT) for Sites 1 and 2. Sites 3 and 4 were fit through a Dmfit deconvolution, using the estimates of the (linewidth/C_Q) from the two-dimensional slices.

DFT calculations were performed to determine the expected C_Q values for the two aluminum sites of Al_4C_3 from the geometry-optimized atomic coordinates in the crystal structure. The C_Q's

Table 3.1: Experimental and calculated NMR parameters for aluminum carbide.

	Al_4C_3 (AlN)			Al_4C_3 (Al^0)			DFT
Site	δ_{iso} (ppm)	C_Q (MHz)	η_Q	δ_{iso} (ppm)	C_Q (MHz)	η_Q	C_Q (MHz)
1	120.5	16.7	0.0	120.5	16.7	0.0	16.74
2	110.1	14.4	0.0	110.0	14.5	0.0	-14.57
3	102.0	11.7	0.0	100.0	11.3	0.0	-
4	98.0	6.0	-	98.0	6.0	-	-

predicted from DFT are in excellent agreement with the experimental results (Table 3.1) for the two sites. Both of the manufacturers' Al_4C_3 samples studied have aluminum sites with C_Q's of approximately 16.7 and 14.5 MHz that correspond to the 4-coordinate Al, as expected. Notably, DFT does calculate a negative C_Q value of -14.57 MHz for one of the sites; as is well known, the sign of C_Q is not evident in the NMR spectrum of the central transition since the terms in the Hamiltonian that contain C_Q are squared. Conventional Bloch decay experiments do not have sufficient information for determining the sign of C_Q, which is why it is often reported (by default) as a value bearing no particular sign.

These individual ^{27}Al resonances were then used in the deconvolution of the 1-dimensional ^{27}Al MAS spectra to yield the remaining aluminum sites present in the broad lineshape. Sites 3 and 4 in Table 3.1 correspond to the broader magenta and narrower, asymmetric purple resonances, respectively, depicted in Figure 3.6b and 3.6d. Table 3.1 gives their deconvoluted values for C_Q: 11.3 to 11.7 MHz for Site 3, and 6.0 MHz for Site 4.

This deconvolution yields the presence of a small symmetric resonance for Al_4C_3 (AlN), drawn in orange (at 113 ppm in Figure 3.6b) that is not present in the other sample. This resonance is effectively a 5^{th} aluminum site and is assigned to an AlN impurity that appears as a high-frequency shoulder of the broad peak. The AlN resonance does not show up in the 3Q-MAS spectrum, likely because AlN has a small C_Q and therefore, is not triple-quantum filtered. It is

unsurprising that aluminum nitride (AlN) can form. Reduction of aluminum oxide in the presence of nitrogen gas has been shown to form AlN.[27,28]

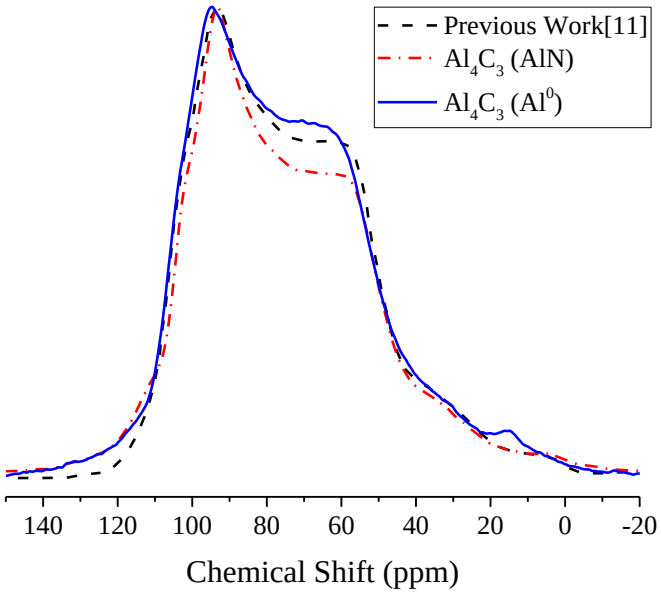

Figure 3.7: Comparison of quantitative 1-dimensional ^{27}Al MAS NMR spectra of Al_4C_3. The black dashed line was adapted from previous work[16].

A comparison of the 1-dimensional MAS spectra of the samples from this study, and for the Al_4C_3 sample studied by NMR previously[16] can be graphed together, and these show good agreement with each other (Figure 3.7). While the spectra are similar in appearance, they show crucial sample-to-sample variations.

These two aluminum carbide materials studied here were synthesized by carbothermal reduction with different starting materials,[29–32] either Al_2O_3 combined with graphite, or metallic aluminum (Al^0) combined with graphite. The unexpected resonances found (that are not consistent with the two 4-coordinate aluminum carbide sites, Sites 1 and 2) likely arise from

impurities introduced during the synthesis of the carbide, such as oxycarbides. Oxycarbides ($Al_4(O,C)_3$ units) are 4-coordinate aluminum species where the central metal is coordinate to both carbon and oxygen atoms.[33–35] In good agreement with a previous study,[36] the values extracted for Sites 3 and 4 have similar isotropic chemical shifts and quadrupolar coupling constants to those of Al_4O_4C and Al_2OC.

What we observe therefore in Figure 3.7 is the high degree of similarity of multiple samples — here two samples with impurities present, detected by 3Q-MAS — shown in red and blue. Comparison to the published Al_4C_3 ^{27}Al MAS NMR lineshape shown in black in Figure 3.7 (notably, at an identical external magnetic field strength of 17.6 T) suggests that the previously-published ^{27}Al tensor (C_Q and δ_{iso}) values for the two Al_4C_3 sites require some revision, owing to the new interpretation of impurities being present.

Subtracting Sites 3 and 4 (and the AlN impurity from the Strem Chemicals sample), we are able to obtain an "idealized" lineshape for Al_4C_3. The deconvolution enabled by 3Q-MAS allows us

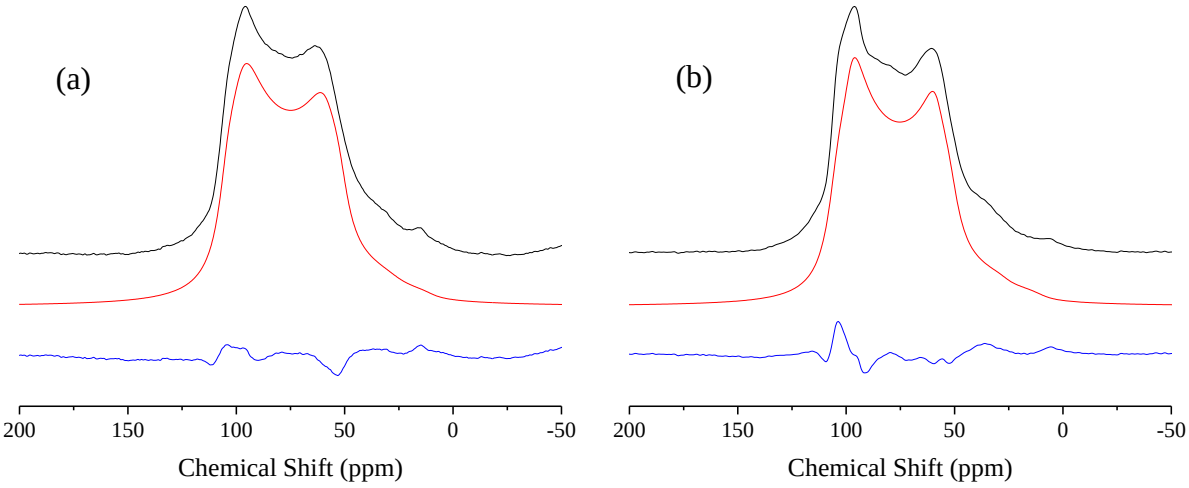

Figure 3.8: (a) ^{27}Al MAS NMR spectrum for Al_4C_3 (Al^0) with the oxycarbide impurities removes (black), simulation using DFT predicted C_Q values (red), and the residual of the experimental and simulation (blue). (b) ^{27}Al MAS NMR spectrum for Al_4C_3 (AlN) with the oxycarbide and AlN impurities removes (black), simulation using DFT predicted C_Q values (red), and the residual of the experimental and simulation (blue).

to predict the theoretical 1-dimensional ^{27}Al MAS Al_4C_3 lineshape and overlay that with the DFT-computed one (Figure 3.8). The good agreement between the two can be seen in the residual plotted beneath the lineshapes in the same figure.

3.1.5 ^{13}C-^{27}Al Correlations

Additional ^{27}Al-{^{13}C} *D*-HMQC experiments were performed to examine the couplings between aluminum and carbon within the aluminum carbide matrix. Similar to the aluminum sites, there was predicted to be only two magnetically inequivalent sites with a occupancy of 2:1. The *D*-HMQC spectra show similar spectra as well, corraborating the hypothesis that these "additional" sites are intrinsic to the aluminum carbide structure and not impurities. These spectra show the existence of more than two types of magnetically inequivalent carbon sites.

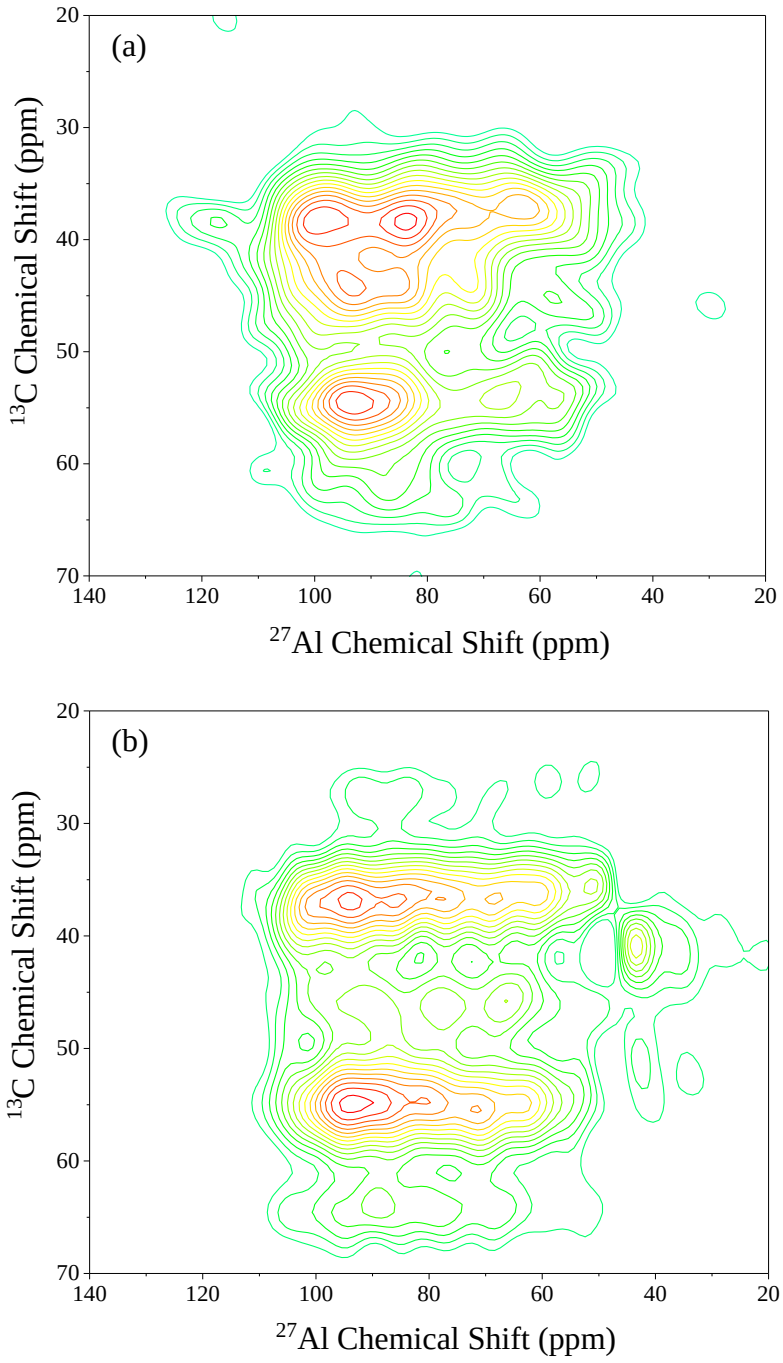

Figure 3.9 ^{27}Al-{^{13}C} *D*-HMQC correlations for (a) Al_4C_3 (AlN) and (b) Al_4C_3 (met-Al). ^{27}Al-{^{13}C} dipolar heteronuclear multiple quantum correlation (*D*-HMQC, with $\nu_o(^{13}C)$ = 188.6 MHz, $\nu_o(^{27}Al)$ = 195.4 MHz) experiments were performed at 17.6 T. The *D*-HMQC experiments utilized a REDOR Box (NMR Service), because this box allows for 2D heteronuclear correlations for nuclei with close Larmor frequencies, such as ^{13}C and ^{27}Al. ^{13}C and ^{27}Al spectra were referenced to TMS and 1M $Al(NO_3)_3$, respectively, at 0.0 ppm.

3.1.6 Conclusions

Despite having highly crystalline materials, second-order quadrupolar broadened resonances can obscure impurities. There are instrumental techniques to overcome broad resonances, but at times it can be difficult to obtain access to high magnetic field strengths or special probes, such as a DOR probe. Implementing 3Q-MAS helps to overcome these instrumental needs, but using a standard MAS probe. To precisely deconvolute resonances contributing to the overall lineshape, accurate ^{27}Al tensors are needed. The accuracy of these values is critically important to confidently deconvolute the ^{27}Al NMR spectrum for Al_4C_3, but can also be crucial for materials that use Al_4C_3 as a starting material in synthetic chemistry (such as the materials described in section 3.2). Performing 3Q-MAS on Al_4C_3 from two different manufactures, we have slightly revised the values of C_Q and δ_{iso} for two ^{27}Al sites. The bulk Al_4C_3 is largely unaffected by the Al^0 and AlN impurities, evidenced by the similarities in the 1-dimensional and 3Q-MAS spectra.

3.2 MIL-53(Al) from Al_4C_3

These materials were synthesized as part of a collaborative project by Colton Moran and Jay Joshi from Prof. Krista Walton's group (Georgia Institute of Technology). Aluminum terephthalate, MIL-53(Al), is a MOF comprised of a series of infinite trans chains of corner sharing octahedral metal centers [$AlO_4(OH)_2$] connected with μ_2-OH groups and bridged by terephthalic acid linkers to create a 1D rhombohedral structure[37]. The aluminum carbide used for these syntheses is the same carbide with the aluminum nitride impurity from section 3.1.2. Generally, MOFs are synthesized from solvothermal reactions, where an inorganic metal salt that dissociates in the solution is used. Using metal salts as the metal source can complicate solvent recycling since salt removal from waste water is costly, and it can create corrosive environments from nitrate and chloride anions[38]. Using metal oxides can reduce the complications for the

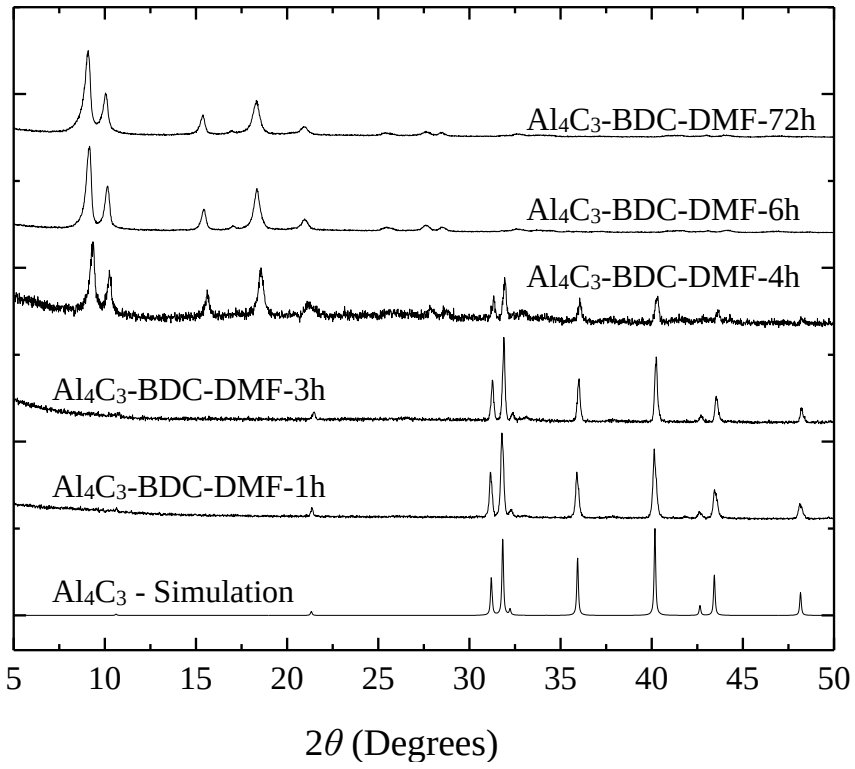

Figure 3.10: PXRD of Al_4C_3-BDC-DMF-XXh with reaction times ranging from 1 – 72h. The bottom pattern is a simulation of Al_4C_3.

previous concerns mentioned, and provide a cost-effect strategy for MOF production. These syntheses were carried out by adding Al_4C_3 and terephthalic acid (benzene dicarboxylate, BDC) to dimethyl formamide (DMF) and placed in an isothermal oven preheated to 220 °C. To explore the synthetic route of MIL-53(Al) production, this reaction mixture was allowed to react for various times (0.5 – 72h), where at short times (< 4h) there was no MIL-53(Al) production and at longer times (≥ 4h) the presence of MIL-53(Al) was detectable from PXRD (performed by Colton Moran and Jay Joshi) and ^{27}Al NMR. PXRD measurements (shown in Figure 3.10) show that Al_4C_3 is still present up until 4h of reaction, which is also where the first detection of MIL-53(Al) is observed.

3.2.1 ^{27}Al NMR of MIL-53(Al) from Al_4C_3

No pretreatment of the samples was done before taking NMR measurements. Samples were stored and packed in 2.5 mm MAS rotors under N_2. ^{27}Al MAS NMR measurements were carried out for all samples at a magnetic field strength of 13.9 T and an MAS spinning frequency of 25 kHz. All spectra were referenced to a 1 M solution of $Al(NO_3)_3$ at 0.0 ppm. The ^{27}Al spectra were recorded using a Larmor frequency of 153.7 MHz. Measurements were recorded using a "pulse-acquire" (Bloch decay) experiment utilizing a radio-frequency pulse with a flip angle of $\pi/18$ (pulse width of 0.3 µs) to ensure quantitative 1D spectra were recorded[18,39]. Liquid-state ^{27}Al NMR was performed on a 4.74 T magnet, using a carrier frequency of 52.7 MHz. Measurements were recorded utilizing a home-built spectrometer and probe with an 8 mm coil. Dmfit was used for all simulated NMR spectra[26].

^{27}Al solid-state NMR offers the opportunity to analyze structure for both crystalline and amorphous content, elucidating the coexistence of multiple species in mixtures as seen here, as a function of the reaction duration. What is shown in Figure 3.11 is a combination of resonances from Al_4C_3; multiple aluminum oxide sites corresponding to 4-, 5-, and 6-coordinate aluminum environments; a characteristic resonance from the MIL-53(Al) product; and an aluminum nitride impurity (at ~115ppm). The ^{27}Al solid-state MAS NMR of the Al_4C_3-BDC-DMF-XXh materials reveals the disappearance of the Al_4C_3 over time and the emergence of MIL-53(Al), in agreement with PXRD patterns in Figure 3.10.

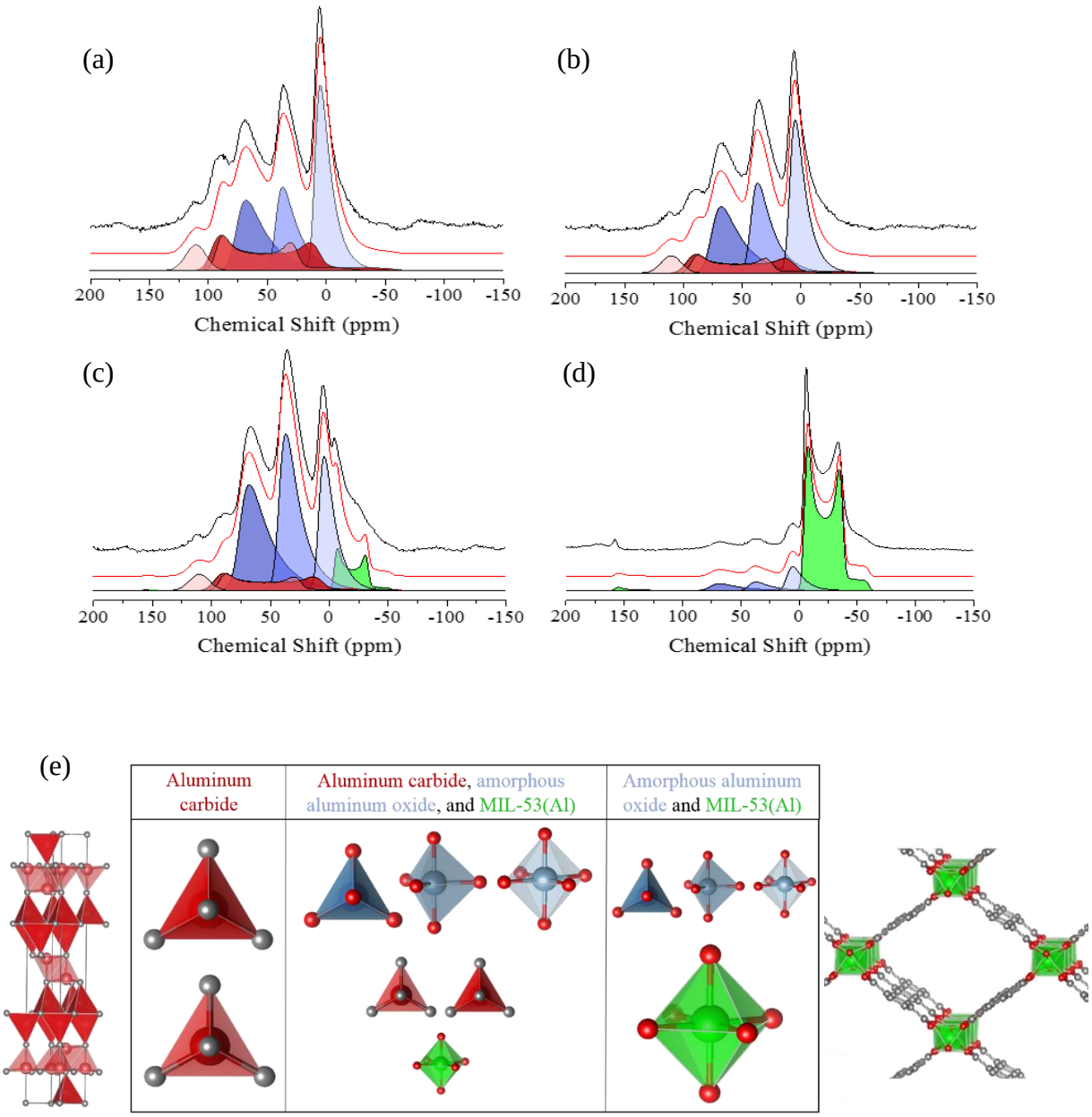

Figure 3.11: ^{27}Al MAS NMR of Al_4C_3-BDC-XXh for reaction times of (a) 0.5h, (b) 3h, (c) 4h, (d) 72h. (e) Color coded polyhedral representation from 4-coordinate Al_4C_3 to 6-coordinate MIL-53(Al) serves as a legend to the spectra. The size of the polyhedra is meant to represent the major/minor components during the reaction.

Lineshapes for the two 4-coordinate aluminum sites of Al_4C_3 have been published previously, with quadrupolar coupling constants (C_Q) of 15.58 and 15.83 MHz. However, from multiple-quantum magic-angle spinning (MQMAS) data (section 3.1.4), we find C_Q values for Al_4C_3 are

16.7 and 14.45 MHz, which are important parameters for the deconvolution of complex overlapping resonances shown in Figure 3.11. The simulation of the MIL-53(Al) resonance reports an isotropic chemical shift of 4.1 ppm and a C_Q of 10 MHz. The aluminum oxide resonances are fit with the Czjzek distribution[40,41] with $\overline{C_Q}$ values for the 4-, 5-, and 6-coordinate Al-O sites of 8.1, 6.8, and 5.8 MHz, respectively. Note: resonances fit with the Czjzek model have a distribution of C_Q values, thus the reported value is an average of the distribution, which is why $\overline{C_Q}$ is used instead of C_Q. The C_Q values are the same for each reaction time, indicating that the amorphous aluminum oxide is structurally similar throughout the reaction, when it is present.

After 30 minutes, multiple aluminum oxide resonances are present. These resonances become more prominent at 3 hours. The emergence of MIL-53(Al) is not detectable until 4 hours of reaction. At 72 hours, the sample is primarily MIL-53(Al), with trace amounts of aluminum oxide present.

The absence of any detectable ^{27}Al signal from liquid-state NMR of the supernatant liquid from Al4C3-BDC-4h provides evidence of minimal or no aluminum ions (approximately < μM concentrations) present in the bulk solution. This result corroborates the idea that the aluminum from Al_4C_3 never goes into a solution phase as MIL-53(Al) is being synthesized.

3.2.2 ^{27}Al NMR Under Water-Controlled Conditions

The previous ^{27}Al NMR study (section 3.2.1) showed that amorphous aluminum oxide was formed at the time of the ^{27}Al NMR measurement, and appears to be an intermediate of the reaction. However, the origin of the aluminum oxide is not completely clear since another pathway to aluminum oxide formation is the degradation of Al_4C_3. Water can react with Al_4C_3 to form aluminum oxides and methane gas. The handling of these materials before and after

synthesis can introduce water into the system. Potential sources of water include, but are not limited to: atmospheric exposure before and after the reaction, “wet” DMF solvent, or surfaces that come in contact with the material.

Materials synthesized in this study were done in a similar fashion as described in section 3.2.1. Controlled synthesis of the materials was executed to mitigate water exposure to the precursors and solvent. Samples studied here were reacted for several designated amounts of time, ranging from 0.5 to 4h. Once the reaction vessel (Teflon-lined Parr reactor) reacted for the pre-determined amount of time, it was removed from the isothermal oven and allowed to cool to room temperature. After cooling, the reaction vessel was placed in a nitrogen environment where it could be safely opened. To filter off excess DMF from the reaction, filter paper was placed in a funnel and pre-soaked with dry DMF so that any water that might have adsorbed into the paper would drain into the collection beaker. After soaking the filter paper, the contents of the vessel were poured onto the filter paper. The materials were allowed to dry until the majority of DMF was in the collection beaker. There was no washing of the materials to dissolve excess (unreacted) BDC left over from the reaction. This was to eliminate potential sources of water from coming in contact with the materials. The samples were transferred in a closed, nitrogen-filled, apparatus that can couple to a gas manifold equipped with a roughing vacuum pump. To completely dry the samples, the materials were heated to 150 °C for 1h while under vacuum. While still under vacuum, the samples were transferred back to the nitrogen environment where they were subsequently packed into a 2.5 mm MAS rotor. The packed 2.5 mm rotor was only removed from its nitrogen environment when it was ready to be immediately placed in the 13.9 T magnet. ^{27}Al MAS NMR measurements were recorded with the same parameters as described in section 3.2.1. The ^{27}Al NMR spectra were deconvoluted using the Dmfit software[26]. Initial

fitting parameters were based on values reported on previously. However, due to the low S/N, there is likely some error in the optimized values. The absence of a washing step to dissolve the excess BDC linker resulted in the majority of the material packed in the 2.5 mm rotor being BDC, causing poor S/N. Acquisitions were recorded for 1-8h to have enough S/N to determine sample evolution.

The proposed reaction scheme for Al_4C_3 to be synthesized into MIL-53(Al) involves a step where amorphous aluminum oxide is formed as an intermediate. Notably, when no MIL-53(Al) has been synthesized, ex situ measurements of the reaction shows the presence of aluminum oxide, where the most intense resonance comes from the 6-coordinate aluminum oxide resonance ($Al^{[6]}$). However, the first indication of MIL-53(Al) formation results in the partial depletion of the $Al^{[6]}$ resonance. This is likely the $Al^{[6]}$ transforming from independent binding units into an extended framework of multiple binding units (i.e. MIL-53(Al)). Without knowledge of how the oxide forms, whether it be an intermediate of the reaction, or merely decomposition of Al_4C_3, it is difficult to determine how and why the oxide forms. The previous measurements in section 3.2.1 were performed on samples that were handled in ambient conditions, likely resulting in the residual Al_4C_3 decomposing. The ^{27}Al NMR results presented here, where materials were protected from moisture, show no significant formation of aluminum oxide at early times (Figure 3.12a). When the sample mixture reacted for 30 min. at 220 °C, there was no significant oxide formation, such that the resonances were easily discernable in the ^{27}Al NMR spectrum. The spectrum at 30 min. can be deconvoluted into the two main sites from Al_4C_3 using second-order quadrupolar broadened lineshapes under MAS conditions, and an additional site to higher frequency due to the aluminum nitride impurity. However, longer reaction times ($\geq$ 2h), there is an obvious formation of aluminum oxide that is formed (resonances for the aluminum oxides are

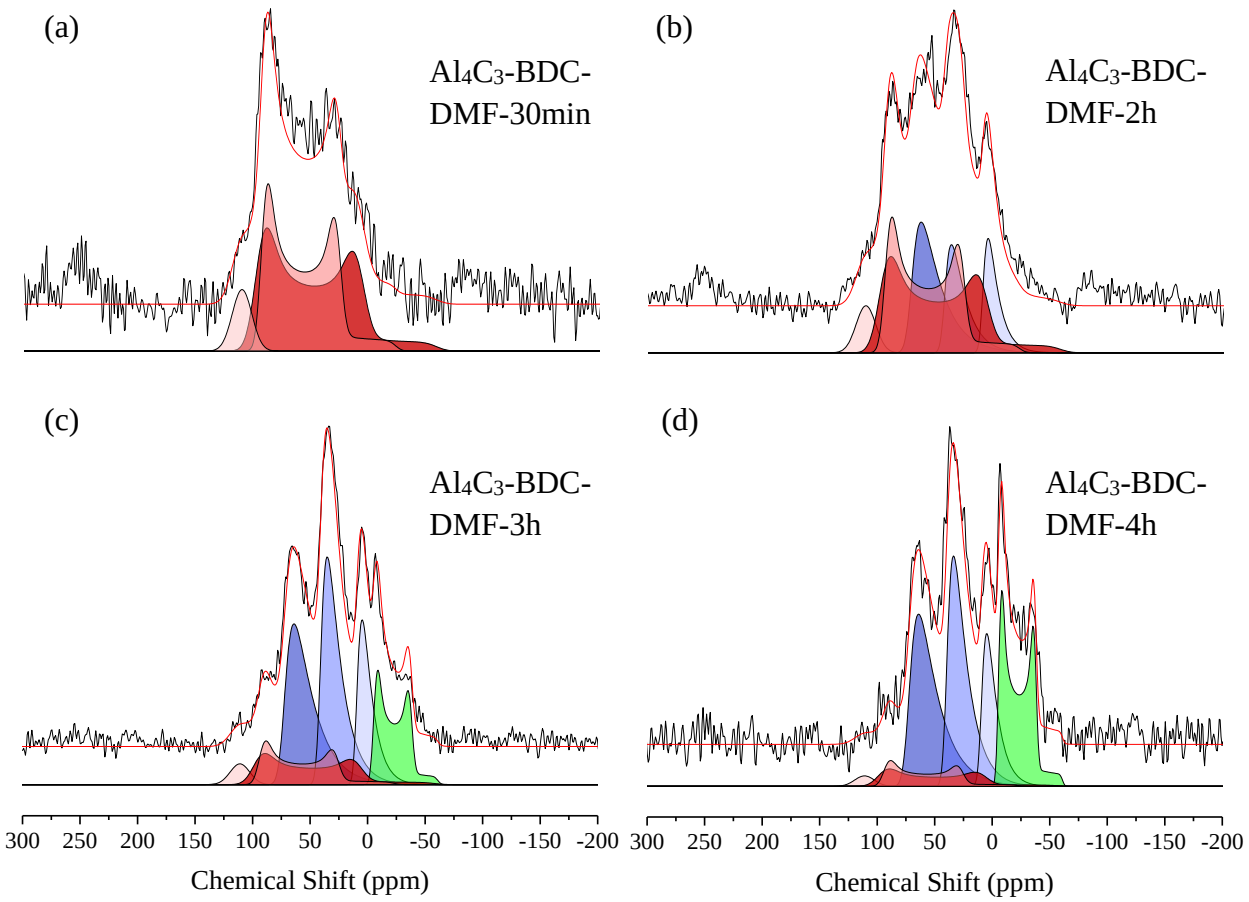

Figure 3.12: ^{27}Al MAS NMR of intermediate reaction times of (a) 30 min., (b) 2h, (c) 3h, and (d) 4h during the synthesis of MIL-53(Al).

shaded in colors of blue in Figures 3.12b,c,d). This formation under controlled conditions supports the idea that aluminum oxide is an intermediate in the synthesis of MIL-53(Al), and not simply the decomposition of Al_4C_3. An additional experiment was performed as a control to determine if Al_4C_3 would degrade in the same synthesis conditions (inside a Parr reactor for 4h in DMF at 220 °C), but in the absence of the BDC linker (Figure 3.13). This result shows no significant degradation of Al_4C_3 into an aluminum oxide, compared to the result in Figure 3.12d. The spectrum in Figure 3.13 has significantly better S/N due to the lack of BDC in the reaction mixture. The coordination of oxygen to aluminum in the MIL-53(Al) structure shows two distinct types of oxygens. One of the oxygens is originating from the carbonyl group on the BDC linker, and the other oxygen is a bridging hydroxide. The first source of oxygen simply comes

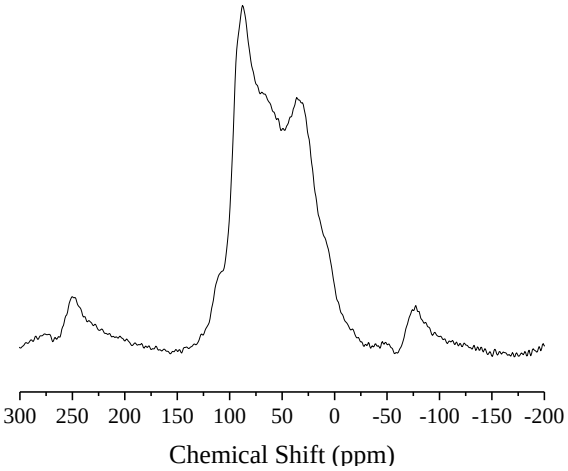

Figure 3.13: ^{27}Al MAS NMR of Al_4C_3 after being placed in DMF for 4h at 220 °C.

from the BDC linker being a starting material for the synthesis. The second source of oxygen likely originates from decomposed DMF reacting with BDC to liberate hydroxyl groups and form *N, N, N', N'*-tetramethylterephthalamide. This reaction would enable the incorporation of bridging hydroxyl groups in the MIL-53(Al) framework.

Synthesis of MIL-53(Al) was accomplished using the insoluable precursor, aluminum carbide. The resulting synthesis lead to some ambiguity about the origin of the aluminum oxides that formed during the synthesis. Through careful preparation of the materials and using ^{27}Al NMR to monitor intermediate formation, we have shown that the amorphous aluminum oxide forms as a result of the synthesis, and not merely the degradation of Al_4C_3.

3.3 Aluminum Carbide-Derived Carbons (CDCs)

These materials were synthesized as part of a collaborative project by Colton Moran from Prof. Krista Walton's group (Georgia Institute of Technology). The aluminum carbide used for these syntheses is the same carbide with the aluminum nitride impurity from section 3.1.2. Aluminum carbide-derived carbons (CDCs) are prepared by flowing chlorine gas at a rate of 40 mL min^{-1} in a stream of argon gas at a rate of 150 mL min^{-1}, over pristine aluminum carbide at the desired

temperature in the range of 300 – 900 °C. The chlorine gas etches the carbide matrix removing aluminum atoms from the structure, while leaving behind porous carbon. However, in this study, only partial etching was conducted to determine the effect of residual metal in the porous carbon[9].

3.3.1 ^{27}Al MAS NMR Measurements

No pretreatment of the samples was done before taking NMR measurements. ^{27}Al MAS NMR was carried out for all samples at a magnetic field strength of 13.9 T. A rotor synchronized (40 μs rotor period, corresponding to a spinning frequency of 25 kHz) Hahn echo pulse sequence with a central-transition selective pulse was employed (CT pulse width = 1.3 μs). All spectra were referenced to a solution of 1 M $Al(NO_3)_3$ at 0.0 ppm. The ^{27}Al spectra were recorded on a Redstone NMR spectrometer (TecMag) at a Larmor frequency of 153.7 MHz. For acquisition of the ^{27}Al spectra, a Bruker HX MAS probe with a 2.5 mm rotor was used. An additional heteronuclear multiple-quantum coherence (HMQC) measurement was recorded at a magnetic field strength of 20.0 T, a spinning frequency of 33.3 kHz to determine which ^{1}H were coupled to the ^{27}Al resonances.

3.3.2 ^{27}Al NMR of Residual Al in CDCs

^{27}Al solid-state NMR can monitor the chemical identity of species present after etching at various temperatures. As a quadrupolar nucleus, the local site symmetry can be observed in many instances in the lineshape for a specific quadrupolar broadened ^{27}Al resonance, depending on the local chemical environment. In fact, such lineshapes are seen in the structure of the Al_4C_3 starting material.

The ^{27}Al solid-state magic-angle spinning (MAS) NMR of the etched Al_4C_3-CDC samples reveals significant chemical changes as the reaction proceeds, both as a function of temperature

and etching time, showing in Figures 3.14-3.16 with NMR parameters given in Table XX. The spectrum of the Al_4C_3-CDC sample etched at 300 °C for 1h (Figure 3.14a) has a quadrupolar lineshape centered at approximately 57 ppm that appears similar to that of the oxycarbide resonance in the parent compound, and is flanked with a resonance (at low frequency) at a chemical shift with a resonance near 7.6 ppm, consistent with a 6-coordinate aluminum site. This 6-coordinate site has been fit to a lineshape with a Czjzek distribution.

Table 3.2: ^{27}Al parameters of Al_4C_3-CDCs spectra. All values correspond to lineshapes modeled in the Dmfit software.

Sample	Fit	δ_{iso} (ppm)	C_Q (MHz)	η_Q
300 °C-1hr	Czjzek	7.6	7.7	-
	Gaussian	94.4	-	-
	Gaussian	100.6	-	-
	Q MAS ½	(centered ~57)	14.5	0.0
500 °C-1hr	Czjzek	-0.9	3.1	-
	Q MAS ½	74.6	10.5	0.0
500 °C-6hr	Czjzek	-1.9	1.9	-
	Gaussian	1.2	-	-
700 °C-1hr	Gaussian	-2.7	-	-
	Quad 1st	14.2	2.38	0.0

A separate HMQC experiment (Figure 3.15) demonstrates that this 6-coordinate site is closely coupled to protons, which allows us to assign this resonance to $Al(OH)_3$. On the high frequency side of the "Q MAS ½" lineshape, there are two sharp resonances in a region where 4-coordinate aluminum is found. These solid-state resonances are both narrow (FWHM ~ 800 Hz), and the chemical shifts at 94.4 and 100.6 ppm are consistent with different $AlCl_x(OH)_y$ species, that resonate at 103 to 94 ppm[42], or potentially with that of Al_2Cl_6 (a "dimer" of $AlCl_3$). (The dimer is known to be a gaseous or molten species, that fits with a narrow linewidth for these 4-coordinate sites but would not be expected to persist in a solid-state experiment, at ambient conditions, as seen here.) However, these results suggest the amorphous and porous carbon host may allow for Al_2Cl_6 to reside in the pores. The spectrum of the sample prepared at 500 °C for 1

hour of etching (Figure 3.14b) looks remarkably different from that of the 300 °C sample. It has a small residual quadrupolar-broadened lineshape (Q MAS ½) centered at in the middle region of the spectrum (shown fit to a quadrupolar-broadened resonance, with $\eta_Q = 0.0$ and $C_Q = 10.5$ MHz), presumably sites similar to that of the remaining parent Al_4C_3. A resonance for a 6-coordinate aluminum is present, peaked at -0.9 ppm and with a Czjzek distribution. Comparison to the 500 °C 6-hour etched sample, shows the disappearance of the resonance from the parent material, and only a more symmetric pair of resonances is found—a sharp resonance (with a

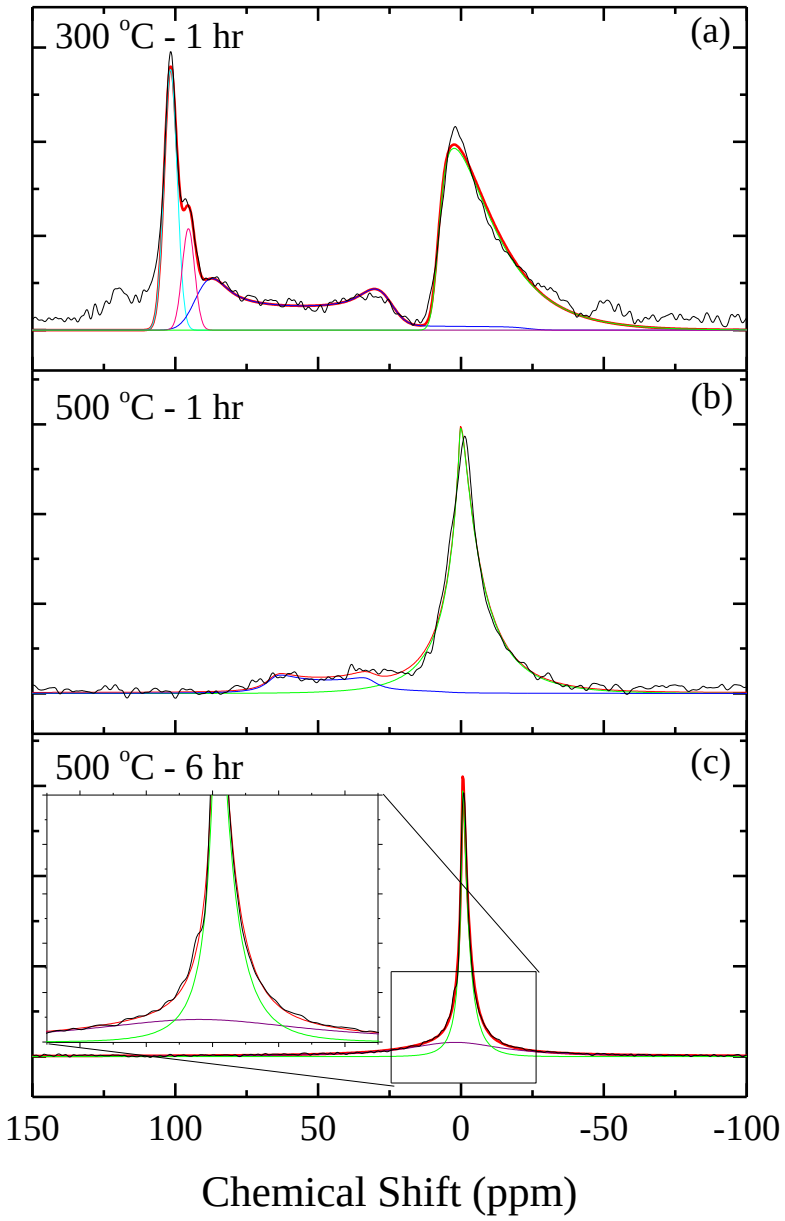

Figure 3.14: ^{27}Al MAS NMR data of Al_4C_3-CDC: (a) 300 °C for 1 hr, (b) 500 °C for 1 hr, and (c) 500 °C for 6 hrs.

relatively narrow Czjzek distribution) at -1.9 ppm superimposed on a broad resonance centered at 1.2 ppm. It is difficult to assign these specifically, as the porous carbon host is increasingly paramagnetic, however the sharp resonance at -1.9 ppm is consistent with similar spectra of $Al(H_2O)_6^{3+}$, which is formed with air exposure of the samples prior to measurement.

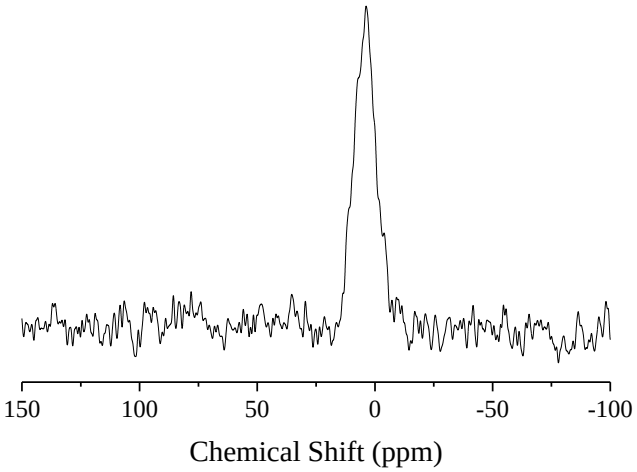

Figure 3.15: ^{27}Al MAS NMR data of Al_4C_3-CDC-300-1h using a double resonance HMQC sequence. The only peak that has nearby hydrogens is the peak around 0 ppm.

Finally, in Figure 3.16 is a ^{27}Al MAS NMR spectrum of the Al-CDC materials etched at 700 °C. For the two 6-coordinate resonances observed, the one at 14.2 ppm has a large manifold of spinning sidebands, which we assign to α-Al_2O_3[43]. Such a manifold of sidebands maps out the lineshape, which is consistent with a crystallographically well-defined state. Fitting of the spectrum in Figure

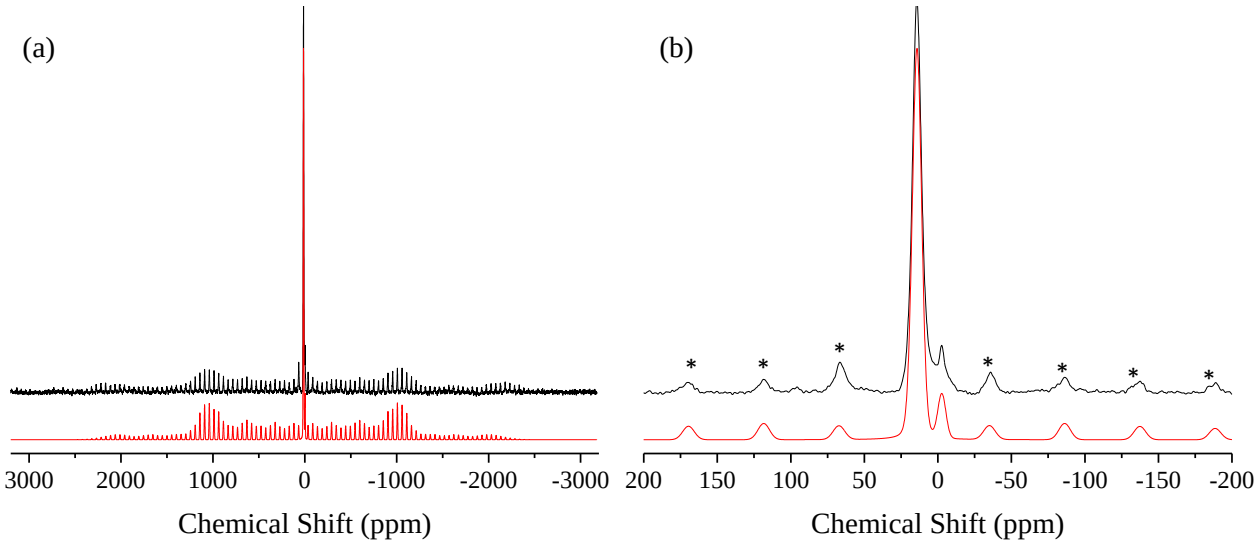

Figure 3.16: (a) ^{27}Al MAS NMR on Al_4C_3-CDC-700-1h spinning at 8 kHz (shown in black) including a fit (shown in red) utilizing previous parameters determined for α-Al_2O_3, C_Q = 2.38 MHz and η_Q = 0.0[44]. On a smaller scale (b) we can see the hydrogen-bearing aluminum peak, at -2.7 ppm, has almost been completely removed and the emergence of a new peak centered at 14.2 ppm, which corresponds to α-Al_2O_3. * refers to spinning sidebands.

3.16 was done in Dmfit and is consistent with parameters previously determined for α-Al_2O_3[26,44]. PXRD indicates the presence of α-Al_2O_3, which we confirm by NMR, but there is also a small amount of residual amorphous aluminum oxide in the 700 °C sample, evidenced by the peak at -2.7 ppm (that does not possess enough long-range order to give PXRD reflections). We cannot exclude other $AlCl_x(OH)_y$ or $AlCl_xO_y$ species from some of the unassigned peaks in Figures 3.14 and 3.16. For example, previous literature has assigned 4-coordinate resonances of $[AlCl_4]^-$ through $[Al(OH)_4]^-$ in the chemical shift range of 79 to 103 ppm, respectively[42]. Further model compounds would be needed to assign such resonances with certainty in the Al-CDC system.

The ^{13}C spectra are wholly uninformative across this series, largely because the carbon rapidly develops paramagnetic centers with etching. It is worthwhile to note that spinning the samples at etching temperatures of 500 °C and higher was difficult, owing to the carbon becoming conductive and causing resistance to MAS from the paramagnetic sites creating "drag" or impedance to spinning in a magnetic field.

3.3.3 ^{27}Al NMR of Post-Synthetic Modification of Residual Al in CDCs

No pretreatment of the samples was done before the NMR measurements. ^{27}Al MAS NMR was carried out for all samples at a magnetic field strength of 13.9 T. All spectra were referenced to a solution of 1.0 M $Al(NO_3)_3$ at 0.0 ppm. The ^{27}Al spectra were recorded on a Redstone NMR spectrometer (Tecmag) at a Larmor frequency of 153.7 MHz. For acquisition of the ^{27}Al spectra, a Bruker HX MAS probe with a 2.5 mm rotor was used. Measurements were recorded using a pulse-acquire experiment, rotation frequency of 25 kHz, a recycle delay of 3s, and a flip angle of $\pi/18$ (corresponding to a pulse width of 0.36 μs) to ensure quantitative 1D spectra[18,39].

^{27}Al solid-state NMR can distinguish different aluminum environments present in multicomponent systems. ^{27}Al is a quadrupolar nucleus (I = 5/2), where information about the local site symmetry can manifest itself in the NMR spectrum. The parent material from which CDCs are derived is a nonporous crystalline material, Al_4C_3, which possesses two magnetically-inequivalent aluminum sites, each coordinated to four carbon atoms[13–15]. As shown previously, after etching for the designated time and temperature, the resulting Al_4C_3-CDC is composed of a combination of multiple polymorphs of BAC/PAC, and amorphous aluminum oxide, unreacted Al_4C_3, and a trace amount of aluminum nitride (an impurity in the starting material)[9]. Both methods for post-synthetic modification of Al_4C_3-CDC involve H_2O, which reacts with Al_4C_3 to produce methane, aluminum hydroxides, and aluminum oxide[45]. Residual Al_4C_3 should not be present since both modifications involve H_2O exposure for at least 24h.

The ^{27}Al solid-state magic-angle spinning (MAS) NMR spectra of the modified Al_4C_3-CDC materials show the existence of similar resonances for BACs (and PACs) and aluminum oxides in all of the materials, but in different proportions. All fits of the spectra were performed with the Dmfit program[26]. Notably, a resonance at 113 ppm is found in all spectra, arising from aluminum nitride, an impurity originating in the Al_4C_3 precursor (as supplied from the manufacturer). In the range of 75 to -20 ppm, there are several resonances fitting a Czjzek distribution that are commonly associated with amorphous aluminum oxides. These resonances are attributed to 4-, 5-, and 6-coordinate aluminum oxides. Notably, there are two 6-coordinate resonances that appear in this range: we attribute the the higher frequency resonance (~ 10 ppm) to 6-coordinate $Al(OH)_3$, based on related studies[9,46], and the lower frequency resonance (~ -2 ppm) to 6-coordinate aluminum sites in BAC/PAC and aluminum oxide[47], that cannot be further resolved or deconvoluted. In the range of 105 – 75 ppm, there is a ^{27}Al NMR signal intensity present (above the baseline) that

we attribute to a distribution of 4-coordinate sites of $[AlCl_4]^-$ through $[Al(OH)_4]^-$, based on the chemical shift range. This range of 4-coordinate sites is shown in Figure 3.17 with a pound symbol above a bracket (indicating the range). As a result of the chlorination and subsequent post-synthetic modification, it is unsurprising that a range of 4-coordinate sites would be found. Finally, at approximately 10 ppm, there is a spinning sideband from the external transitions.

All four spectra shown in Figure 3.17 display these resonances described above, but in different proportions. The comparison of one preparation (i.e., H_2O) at two different temperatures shows a

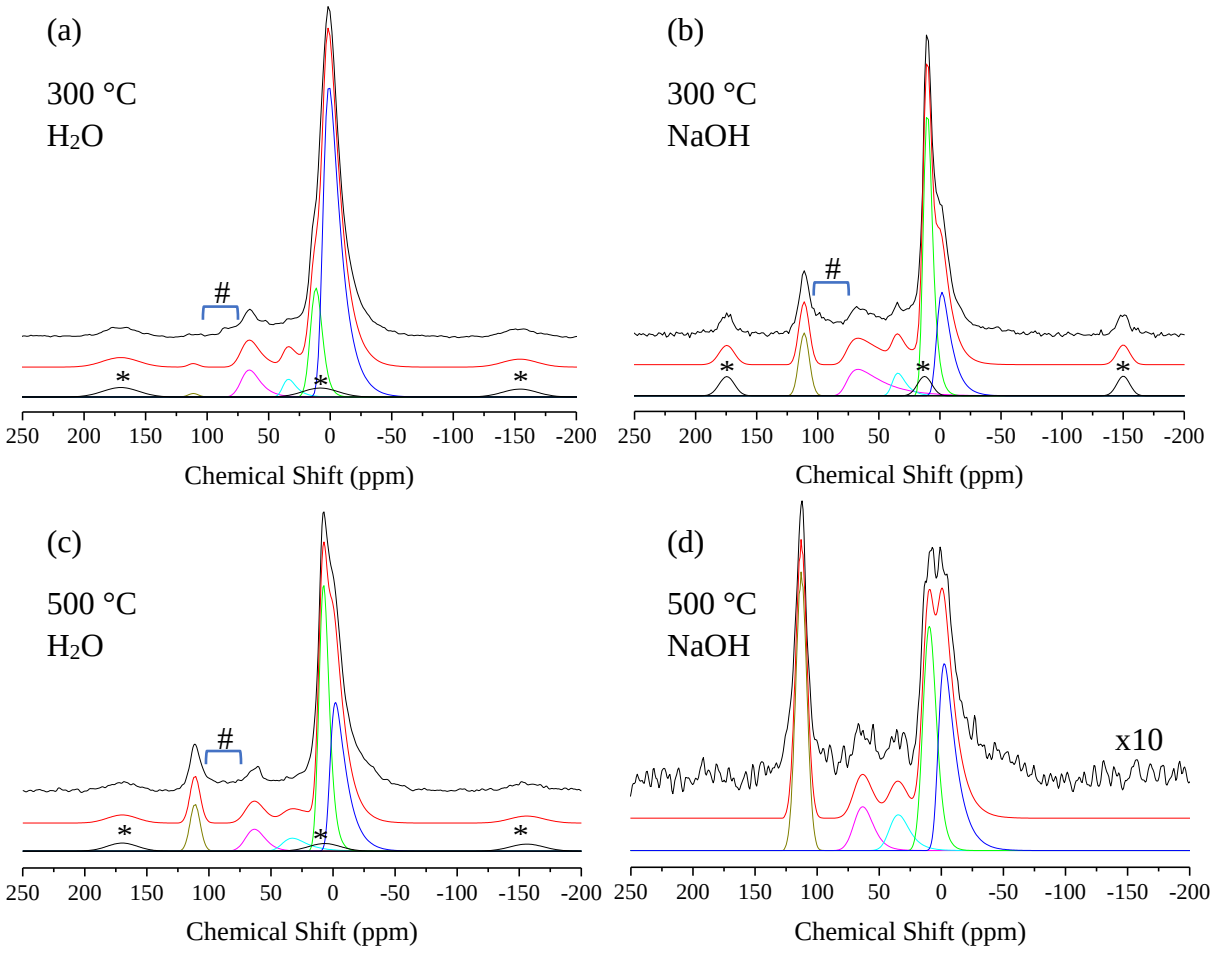

Figure 3.17: ^{27}Al MAS NMR spectra of (a) Al_4C_3-CDC-300-1h-24h-H_2O (b) Al_4C_3-CDC-300-1h-24h-NaOH (c) Al_4C_3-CDC-500-1h-24h-H_2O (d) Al_4C_3-CDC-500-1h-24h-NaOH. The asterisks (*) denote the spinning sidebands from external transitions. The external transitions were simulated with a Gaussian, and the intensities and widths were based on the n ± 1 spinning sidebands.

dramatic change in the amount of [$Al(OH)_3$] present. Similarly, comparing a single temperature (i.e., 300 °C) with two different preparations also shows a dramatic increase in the resonance corresponding to [$Al(OH)_3$]. For the 500 °C NaOH preparation, the signal-to-noise ratio becomes very poor, complicating the comparison between it and other spectra. It is worthwhile to note, the Al_4C_3-CDC materials have less aluminum than the Al_4C_3 precursor as a result of the etching process. The materials etched at 300 °C and 500 °C are expected to have 18% and 8% of the original aluminum content, respectively.[9] Due to the difference in aluminum content between the different etching temperatures, the samples prepared at 500 °C required double the number of NMR transients acquired, compared to the samples prepared at 300 °C. In addition to these differences, there is a reduction in the aluminum content due to leaching during the post-synthetic modification. In agreement with the TGA results, it appears that the NaOH solution removes more aluminum than the H_2O modification., evidenced by both sets of spectra (comparing Figure 3.17 a versus b, and c versus d), there is poorer signal-to-noise ratios for the ^{27}Al NMR, for those samples that have gone through NaOH treatment.

References

[1] R.E. Wasylishen, S.E. Ashbrook, S. Wimperis, eds., NMR of Quadrupolar Nuclei in Solid Materials, John Wiley and Sons, Ltd, West Sussex, 2012.

[2] A. Llor, J. Virlet, TOWARDS HIGH-RESOLUTION NMR OF MORE NUCLEI IN SOLIDS: SAMPLE SPINNING WITH TIME-DEPENDENT SPINNER AXIS ANGLE, Chem. Phys. Lett. 152 (1988) 248–253.

[3] B.F. Chmelka, K.T. Mueller, A. Pines, J. Stebbins, Y. Wu, J.W. Zwanziger, Oxygen-17 NMR in solids by dynamic-angle spinning and double rotation, Nature. 339 (1989) 42–43. doi:10.1038/339042a0.

[4] K.. Mueller, B.. Sun, G.. Chingas, J.. Zwanziger, T. Terao, A. Pines, Dynamic-angle spinning of quadrupolar nuclei, J. Magn. Reson. 86 (1990) 470–487. doi:10.1016/0022-2364(90)90025-5.

[5] K.T. Mueller, Y. Wu, B.F. Chmelka, J. Stebbins, A. Pines, High-resolution oxygen-17 NMR of solid silicates, J. Am. Chem. Soc. 113 (1991) 32–38. doi:10.1021/ja00001a006.

[6] A. Samoson, E. Lippmaa, A. Pines, High resolution solid-state N.M.R., Mol. Phys. 65 (1988) 1013–1018. doi:10.1080/00268978800101571.

[7] J.C. Facelli, D.M. Grant, Determination of molecular symmetry in crystalline naphthalene using solid-state NMR, Nature. 365 (1993) 325–327. doi:10.1038/365325a0.

[8] J. Leis, A. Perkson, M. Arulepp, M. Käärik, G. Svensson, Carbon nanostructures produced by chlorinating aluminium carbide, Carbon N. Y. 39 (2001) 2043–2048. doi:10.1016/S0008-6223(01)00020-3.

[9] C.M. Moran, R.M. Marti, S.E. Hayes, K.S. Walton, Synthesis and characterization of aluminum carbide-derived carbon with residual aluminum-based nanoparticles, Carbon N. Y. 114 (2017) 482–495. doi:10.1016/j.carbon.2016.11.083.

[10] F. Fariaut, C. Boulmer-Leborgne, E. Le Menn, T. Sauvage, C. Andreazza-Vignolle, P. Andreazza, C. Langlade, Excimer laser induced plasma for aluminum alloys surface carburizing, Appl. Surf. Sci. 186 (2002) 105–110.

[11] Y. Sun, H. Cui, L. Gong, J. Chen, J. She, Y. Ma, P. Shen, C. Wang, Carbon-in-Al4C3 Nanowire Superstructures for Field Emitters, ACS Nano. 5 (2011) 932–941. doi:10.1021/nn102173b.

[12] Y. Sun, H. Cui, L. Gong, J. Chen, P.K. Shen, C.X. Wang, Field nanoemitter: One-dimension Al4C3ceramics, Nanoscale. 3 (2011) 2978–2982. doi:10.1039/c1nr10194c.

[13] M. von Stackelberg, E. Schnorrenberg, The Structure of Aluminum Carbide, Al_4C_3, Zeitschrift Für Phys. Chemie. B27 (1934) 37–49.

[14] G.A. Jeffrey, V. Wu, The structure of the aluminum carbonitrides. II, Acta Crystallogr. 20 (1966) 538–547. doi:10.1107/S0365110X66001208.

[15] T.M. Gesing, W. Jeitschko, The Crystal Structure and Chemical Properties of $U_2Al_3C_4$ and Structure Refinement of Al_4C_3, Z. Naturforsch. B. 50 (1995) 196–200.

[16] T. Bräuniger, C.V. Chandran, U. Wedig, M. Jansen, NMR chemical shift and quadrupolar interaction parameters of carbon-coordinated 27Al in aluminium carbide, Al4C 3, Zeitschrift Fur Anorg. Und Allg. Chemie. 637 (2011) 530–535. doi:10.1002/zaac.201000445.

[17] J.E. House, K.A. House, Descriptive Inorganic Chemistry, Third, Elsevier, London, 2016.

[18] D. Fenzke, D. Freude, T. Fröhlich, J. Haase, NMR Intensity Measurements of Half-Integer Quadrupole Nuclei, Chem. Phys. Lett. 111 (1984) 171–175.

[19] D. Müller, W. Gessner, A. Samoson, E. Lippmaa, G. Scheler, Solid-state 27Al NMR studies on polycrystalline aluminates of the system CaO-Al2O3, Polyhedron. 5 (1986) 779–785. doi:10.1016/S0277-5387(00)84437-X.

[20] S.J. Clark, M.D. Segall, C.J. Pickard, P.J. Hasnip, M.I.J. Probert, Keith Refson, First principles methods using CASTEP, Z. Krist. 220 (2005) 567–570.

[21] J.P. Perdew, K. Burke, M. Ernzerhof, Generalized Gradient Approximation Made Simple, Phys. Rev. Lett. 77 (1996) 3865–3868.

[22] J.-P. Amoureux, M. Pruski, Encyc. Nucl. Magn. Reson., (2002).

[23] J.P. Amoureux, C. Fernandez, L. Frydman, Optimized multiple-quantum magic-angle spinning NMR experiments on half-integer quadrupoles, Chem. Phys. Lett. 259 (1996) 347–355. doi:10.1016/0009-2614(96)00809-3.

[24] J.P. Amoureux, M. Pruski, D.P. Lang, C. Fernandez, The Effect of RF Power and Spinning Speed on MQMAS NMR, J. Magn. Reson. 131 (1998) 170–175. doi:10.1006/jmre.1997.1275.

[25] J.-P. Amoureux, C. Fernandez, S. Steuernagel, Z Filtering in MQMAS NMR, J. Magn. Reson. Ser. A. 123 (1996) 116–118. doi:10.1006/jmra.1996.0221.

[26] D. Massiot, F. Fayon, M. Capron, I. King, S. Le Calvé, B. Alonso, J.O. Durand, B. Bujoli,

Z. Gan, G. Hoatson, Modelling one- and two-dimensional solid-state NMR spectra, Magn. Reson. Chem. 40 (2002) 70–76. doi:10.1002/mrc.984.

[27] P. Lefort, M. Billy, Mechanism of AlN Formation through the Carbothermal Reduction of Al_2O_3 in a Flowing N_2 Atmosphere, J. Am. Ceram. Soc. 76 (1993) 2295–2299. doi:10.1111/j.1151-2916.1993.tb07767.x.

[28] P. Wei, Y. Qing, C. Juan, Mechanism of carbothermal synthesis of aluminium nitride, Thermochim. Acta. 325 (1999) 89–93. doi:10.1016/S0040-6031(98)00562-0.

[29] A.N. Streletskii, I. V. Kolbanev, A.B. Borunova, A. V. Leonov, P.Y. Butyagin, Mechanochemical activation of aluminum: 1. Joint grinding of aluminum and graphite, Colloid J. 66 (2004) 729–735. doi:10.1007/s10595-005-0068-6.

[30] A.N. Streletskii, I. V Povstugar, A.B. Borunova, S.F. Lomaeva, P.Y. Butyagin, Mechanochemical Activation of Aluminum: 4. Kinetics of Mechanochemical Synthesis of Aluminum Carbide, Colloid J. 68 (2006) 470–480. doi:10.1134/S1061933X06040119.

[31] A.N. Streletskii, S.N. Mudretsova, I. V Povstugar, P.Y. Butyagin, Mechanochemical Activation of Aluminum: 5. Formation of Aluminum Carbide upon Heating of Activated Mixtures, Colloid J. 68 (2006) 623–631. doi:10.1134/S1061933X06040119.

[32] J. Li, G. Zhang, D. Liu, O. Ostrovski, Low-temperature Synthesis of Aluminium Carbide, ISIJ Int. 51 (2011) 870–877. doi:10.2355/isijinternational.51.870.

[33] L.M. Foster, G. Long, M.S. Hunter, Reactions Between Aluminum Oxide and Carbon. The Al_2O_3-Al_4C_3 Phase Diagram, J. Am. Ceram. Soc. 39 (1956) 1–11. doi:10.1016/0022-4596(78)90152-4.

[34] G.A. Jeffrey, M. Slaughter, The Structure of Aluminum Tetroxycarbide, Acta Crystallogr. 16 (1963) 177–184. doi:10.1107/S0365110X63000451.

[35] Y. NAKASHIMA, T. SHIRAI, C. TAKAI, M. FUJI, Synthesis of aluminum oxycarbide (Al_2OC) by selective microwave heating, J. Ceram. Soc. Japan. 124 (2016) 122–124. doi:10.2109/jcersj2.15200.

[36] L. Baggetto, V. Sarou-Kanian, P. Florian, A.N. Gleizes, D. Massiot, C. Vahlas, Atomic scale structure of amorphous aluminum oxyhydroxide, oxide and oxycarbide films probed by very high field ^{27} Al nuclear magnetic resonance, Phys. Chem. Chem. Phys. 19 (2017) 8101–8110. doi:10.1039/C6CP07937G.

[37] T. Loiseau, C. Serre, C. Huguenard, G. Fink, F. Taulelle, M. Henry, T. Bataille, G. Férey, A Rationale for the Large Breathing of the Porous Aluminum Terephthalate (MIL-53) Upon Hydration, Chem. – A Eur. J. 10 (2004) 1373–1382. doi:10.1002/chem.200305413.

[38] G. Majano, J. Pérez-Ramírez, Scalable room-temperature conversion of copper(II) hydroxide into HKUST-1 ($Cu_3(btc)_2$), Adv. Mater. 25 (2013) 1052–1057. doi:10.1002/adma.201203664.

[39] E. Lippmaa, A. Samoson, M. Magi, High-Resolution 27Al NMR of Aluminosilicates, J. Am. Chem. Soc. 108 (1986) 1730–1735.

[40] G. Czjzek, J. Fink, F. Götz, H. Schmidt, Atomic coordination and the distribution of electric field gradients in amorphous solids, Phys. Rev. B. 23 (1981) 2513–2530.

[41] J. Espinose, D. Lacaillerie, C. Fretigny, D. Massiot, MAS NMR spectra of quadrupolar nuclei in disordered solids : The Czjzek model, J. Magn. Reson. 192 (2008) 244–251.

doi:10.1016/j.jmr.2008.03.001.

[42] Z. Černý, J. Macháček, J. Fusek, B. Čásenský, O. Kříž, D.G. Tuck, Aluminum-27 and ^{71}Ga NMR studies of the solution chemistry of Ga[$AlCl_4$] and related compounds, J. Chem. Socienty, Dalt. Trans. Inorg. Chem. (1998) 1439–1446.

[43] H.J. Jakobsen, J. Skibsted, H. Bildsoe, N.C. Nielsen, Magic-Angle Spinning Nmr-Spectra of Satellite Transitions for Quadrupolar Nuclei in Solids, J. Magn. Reson. 85 (1989) 173–180. doi:Doi 10.1016/0022-2364(89)90333-8.

[44] L.A. O'Dell, S.L.P. Savin, A. V. Chadwick, M.E. Smith, A ^{27}Al MAS NMR study of a sol-gel produced alumina: Identification of the NMR parameters of the θ-Al_2O_3transition alumina phase, Solid State Nucl. Magn. Reson. 31 (2007) 169–173. doi:10.1016/j.ssnmr.2007.05.002.

[45] L.M. Nikolaevich, CH 8: Reaction of Aluminum Powders with Liquid Water and Steam, in: Met. Nanopowders Prod. Charact. Energ. Appl., 2014: pp. 163–197.

[46] J.Z. Hu, X. Zhang, N.R. Jaegers, C. Wan, T.R. Graham, M. Hu, C.I. Pearce, A.R. Felmy, S.B. Clark, K.M. Rosso, Transitions in Al Coordination during Gibbsite Crystallization Using High-Field ^{27}Al and ^{23}Na MAS NMR Spectroscopy, J. Phys. Chem. C. 121 (2017) 27555–27562. doi:10.1021/acs.jpcc.7b10424.

[47] K.N. Trivedi, A.B. Boricha, H.C. Bajaj, R. V. Jasra, Synthesis of Polyaluminum Chloride Using Alternative and Simple Ultrasonic Vibration System, CLEAN - Soil, Air, Water. 38 (2010) 446–451. doi:10.1002/clen.201000040.

Chapter 4: Shifted-Echo MQ-MAS

4.1 Introduction to MQ-MAS

For half-integer quadrupolar nuclei, the central transition (-1/2 ↔ 1/2) is unaffected by first-order quadrupolar broadening. The linewidth for these quadrupolar systems on the central transition is primarily dominated by second-order effects, which are typically 10^2-10^3 times smaller than first-order effects on satellite transitions (m -1 ↔ m, $m \neq 1/2$, where m is the spin quantum number)[1]. Second-order quadrupolar broadening effects on the central transition are reduced by a factor of approximately 3; in many cases this is not enough to adequately resolve multiple resonances. To combat this broadening and improve resolution, techniques such as dynamic-angle spinning (DAS)[2–5] and double-rotation (DOR)[3,5,6] NMR were created, but these require different probe hardware modifications to employ. However, the development of multiple-quantum magic-angle spinning (MQ-MAS) NMR experiments by Frydman and Harwood[7] (where it was realized that an isotopic spectrum, of quadrupolar nuclei broadened to the second-ordered, could be obtained from a skew projection of a 2-dimensional spectrum that correlates single- and triple-quantum coherences), enabled NMR spectroscopists to study quadrupolar nuclei broadened by second-order quadrupolar effects, without needing to resort to specialized techniques, such as DAS and DOR.

4.2 Shifted Echo Pulse Sequence and Δp-pathways

Initially, the MQ-MAS pulse sequence was a two-pulse technique[7] with a triple-quantum excitation pulse and a conversion pulse. Since this first experiment, many MQ-MAS sequences utilize at least three pulses, such as Z-filtered[8] and shifted-echo[9] MQ-MAS experiments. The shifted-echo pulse sequence (Figure 4.1a) uses two non-selective (high power) pulses that excite

and convert the triple-quantum coherence and one selective (low power) pulse that converts the triple-quantum coherence into a single-quantum coherence. Typically, this sequence is executed

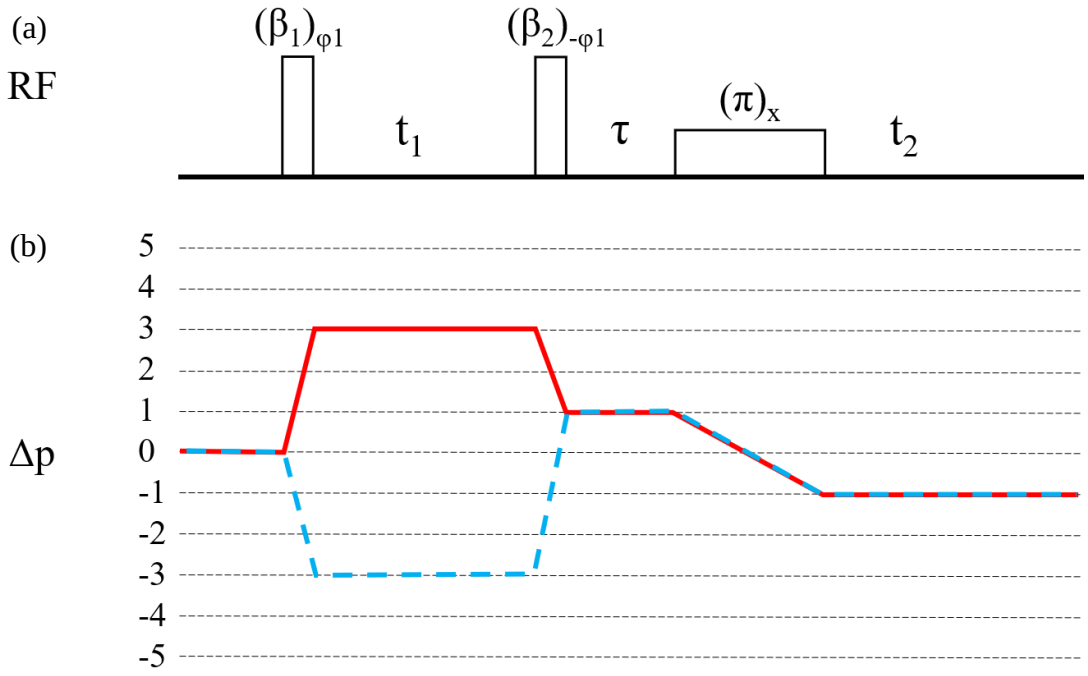

Figure 4.1: (a) Shifted-echo pulse sequence where β_1 and β_2 are the optimized pulses, respectively. The phases for β_1 and β_2 are incremented by steps of 360°/16 in an additional dimension (explained in section 4.2.1). The third pulse is a soft π pulse with fixed phase and should be calibrated to excite the bandwidth of the central transition. The triple-quantum information is stored in the t_1 time-domain, the single-quantum information is stored in the t_2 time-domain, and τ determines how far out in time the echo is shifted in the t_2 time-domain. (b) The p-pathway diagram showing the generation of the triple-quantum coherence and the conversion of the triple-quantum to single-quantum coherence. The solid red pathway is the echo pathway and the dashed blue line is the anti-echo pathway for a spin-3/2 system.

using a predetermined 96-step phase cycle[9], which can cause long experimental acquisition times since n·96 acquisitions are required to complete a full phase cycle. However, shifted echo MQ-MAS was performed here by storing phase in an additional dimension, which only requires 16 steps (these details are explained below in section 4.2.1). This sequence gives rise to two signals, an anti-echo and echo (sometime referred to as a "whole-echo" experiment[9]). A benefit of the whole echo sequence is the ability to co-add the anti-echo and echo for better signal-to-noise. The two echoes do not necessarily need to be co-added for accurate MQ-MAS

spectra. This means if the anti-echo were to be truncated during the aquisition (because a large enough τ value was not selected) and unusable, the echo time-domain data should still be useable. The anti-echo "travels backwards" in time, which means the start of the whole-echo (t_1 = 0 μs) needs to be shifted far enough in time, so that the anti-echo signal does not get truncated in the time-domain. However, depending on the transverse relaxation, it may be beneficial to use a short τ in order to avoid attenuation of the echo signal. Figure 4.1b shows the Δp-pathway for the coherences, where $\Delta p = m_f - m_i$, and m_f is the final state after the transition from an RF pulse, and m_i the initial state.

4.2.1 Incrementing Phase

Storing phase in an additional dimension is incorporated into the shifted-echo MQ-MAS sequence to exploit a Fourier relationship between phase (φ) and the coherences (Δp) created from the pulses, and is as follows[10,11],

$$s(\Delta p) = \int_0^{2\pi} s(\varphi) e^{i\Delta p \varphi} d\varphi. \quad (4.1)$$

Where s(Δp) is a function of coherence and s(φ) is a function of phase. The integral covers the range of 0 to 2π, because this range covers the entirety of possible phases for the pulse. The number of Δp-pathways is dictated by the increment of phase. For example, if the phase was incremented in steps of four (360°/4), there would be five total pathways: four for ±1 and ±2 from incrementing our phase by 360°/4, and a Δp = 0 for coherences that add to zero or do not have transitions. For the shifted-echo MQ-MAS sequence, the phase is incremented by 16 steps, so that the total range of Δp-pathways ranges from +8 to -8 (see Figure 4.2). In Figure 4.1a, the phase for the first pulse is φ_1, and the phase for the second pulse is $-\varphi_1$, for simplicity. Otherwise, if we stored phase into two separate dimensions so that the phase for the first pulse was φ_1 and the phase for the second pulse was φ_2, then an additional dimension would need to be

incorporated into the sequence. This would result the regular 2-dimensional MQ-MAS shifted-echo sequence to have four dimensions. However, because of the Δp-pathway, the second phase can be set to the negative of the first phase. Doing so results in the addition of only one extra dimension, making the shifted-echo MQ-MAS sequence into a 3-dimensional sequence. When using one phase dimension for two or more pulses, the resulting coherence is in the *accumulated* Δp-pathway, shown in Equation 4.2. For the shifted-echo MQ-MAS sequence shown in Figure

$$\Delta p_1\varphi_1 + \Delta p_2(-\varphi_1) = (\Delta p_1 - \Delta p_2)\varphi_1 = \Delta p_{accumulated}\varphi_1. \quad (4.2)$$

4.1a, this means anti-echo will appear in the [(-3) (φ_1) + (+4)(-φ_1)]/ φ_1 = [-7φ_1]/ φ_1 = -7 Δp-pathway and the echo will appear in the +5 Δp-pathway, as seen in Figure 4.2. This is why

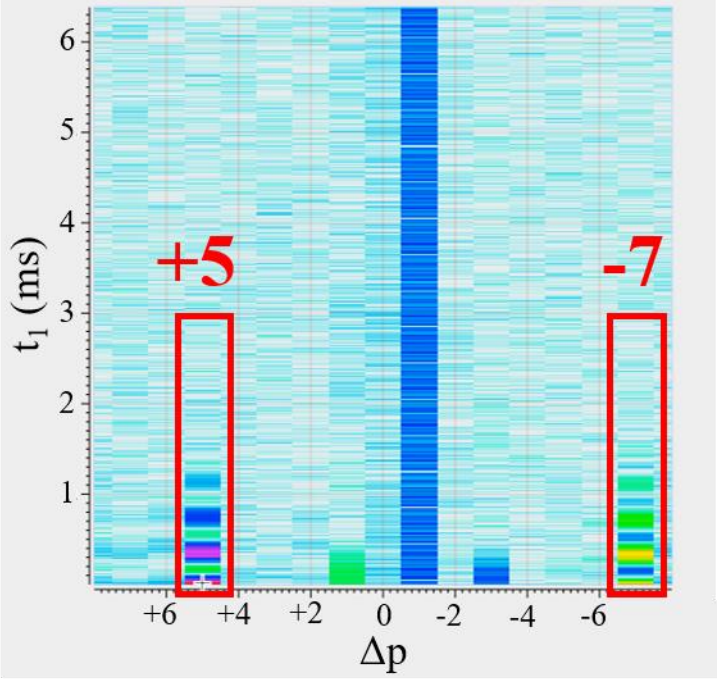

Figure 4.2: x-axis is the Fourier transform of the phase dimension and the y-axis is the t_1 dimension of the shifted-echo MQ-MAS sequence. Note, the t_2 dimension is not visible here, because it is stored in the "depth" of this depiction. This shifted-echo MQ-MAS data is from ^{87}Rb NMR of $RbNO_3$ at 13.9 T.

increments of 16 for the phase is needed, otherwise if a smaller increment were used (i.e. 8 increments), the coherences would alias to a different Δp-pathway. If the shifted-echo MQ-MAS sequence has been properly optimized, the coherences for the anti-echo and echo will appear in

the -7 and +5 Δp-pathways, respectively, which is shown in Figure 4.2. Extracting the -7 and +5 slices from this data will give the 2-dimensional time-domain data, as seen in Figure 4.3.

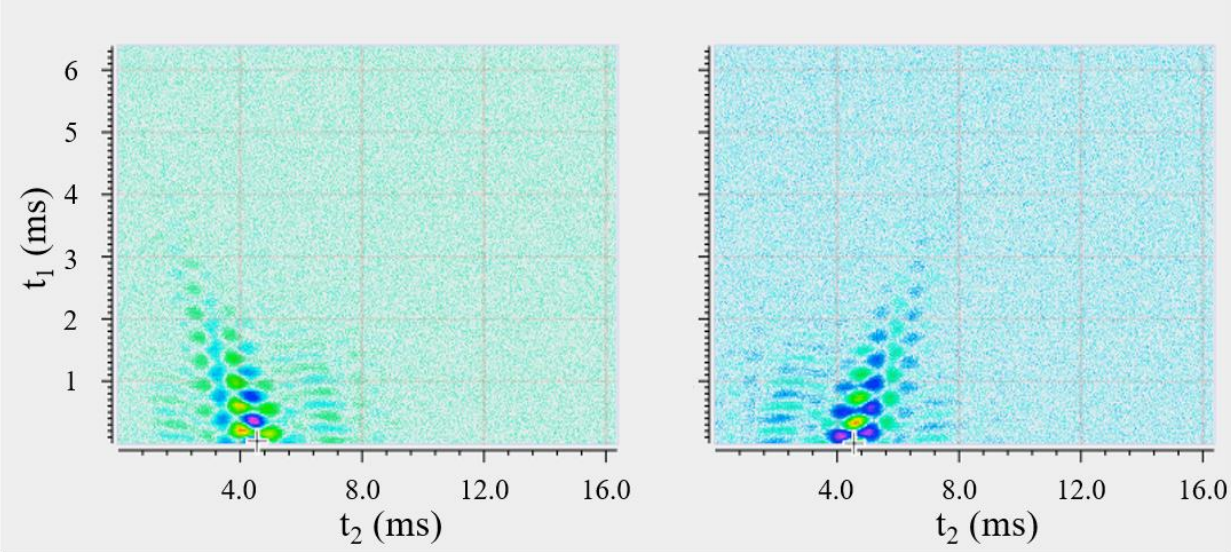

Figure 4.3: Slices from Figure 4.2 for the 2-dimensional time-domain data for the -7 (anti-echo, left side of this figure) and +5 (echo, right side of this figure) Δp-pathways.

There are a couple of ways to program this pulse sequence (Figure 4.1a) with a phase dimension. The first dimension will always be for t_2 time-domain (conventional 1-dimensional acquisition). The second dimension can be set to either the phase dimension (in a 1D-2D-3D scheme, this would be t_2-φ-t_1) or the t_1 time-domain (t_2-t_1-φ), and the third dimension would be set to the option not selected for the second dimension. Both setups will work and will take the same amount of time to *complete* a full MQ-MAS dataset, which works if the pulses are already optimized. For this reason, the way to program the pulse sequence for optimization, (to "check" which Δp-pathways the coherences are going to) is to unconventionally set the phase dimension as the second dimension and the t_1 time-domain as the third dimension (the t_2-φ-t_1 scheme). This means for every completed t_1 point, there will be a full phase cycle dimension completed, which means shorter experiments can be performed to determine which Δp-pathways the coherences are going to while optimizing the first two pulses. Otherwise, if the sequence is programed the

other way (t_1 time-domain for the second dimension and phase dimension as the third dimension), then the entirety of the MQ-MAS experiment must finish before checking if the coherences are in the correct Δp-pathways.

4.3 Optimizing Shifted-Echo MQ-MAS for *I* = 3/2

For the best excitation of the resonances of interest, the carrier frequency from the spectrometer is centered in the middle of the entire resonance. Next, the highest possible RF power that is safe for the probe (no arcing) should be used, since this helps with the efficiency of the multiple-

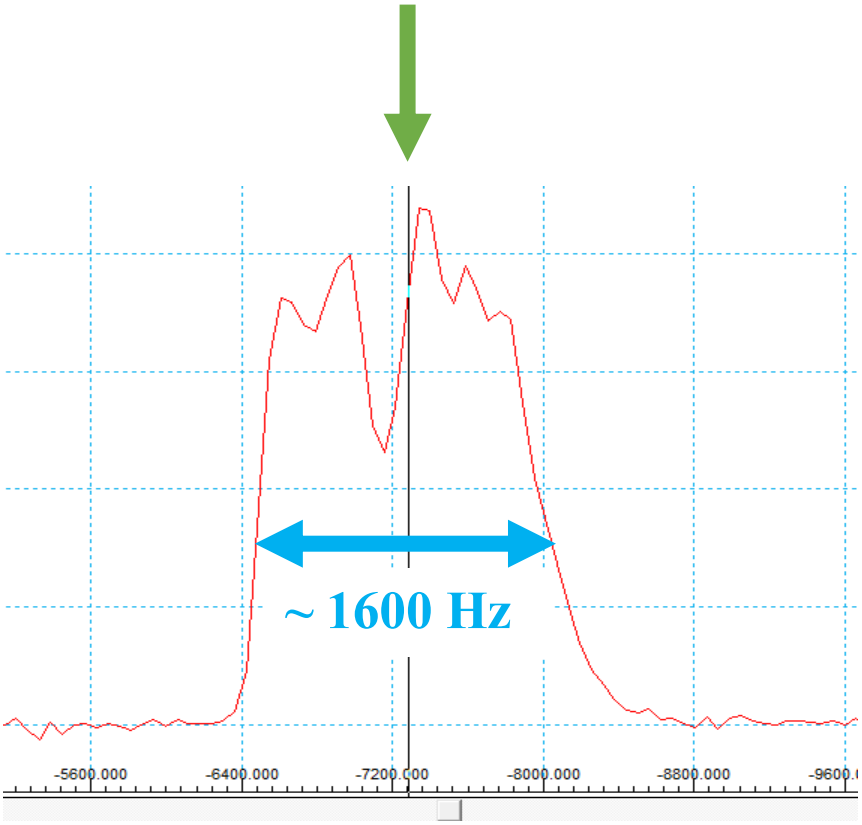

Figure 4.4: 1-dimensional ^{87}Rb MAS NMR spectrum of $RbNO_3$ at 13.9 T. The carrier frequency is shifted by -7286.6 Hz (from the 0.0 ppm reference) to place the carrier frequency (green arrow) at the same frequency of the resonances.

quantum excitation and conversion, which helps with sensitivity[12]. These parameters will be important for the first two non-selective (high power) pulses. Then a low power pulse (typically 15 – 20 kHz of RF strength) should be calibrated that is capable of exciting the bandwidth of the

central transition. This selective (low power) setting is used for the π pulse, to transfer the Δp = 1 to a Δp = -1 coherence. Assuming the T_1 relaxation time is known, pulse optimization is then started. For a spin-3/2 system, a good guess for the first pulse is 10% of the rotor period used. To limit the amount of single-quantum coherence generated, a pulse width that is close to a 2π pulse width and 10% of the rotor period is used. The second pulse exploits the use of the rotation-induced adiabatic coherence transfer (RIACT)[13] mechanism, which efficiently transfers triple-quantum coherence to single-quantum coherence; the concept of triple- to single-quantum coherence transfer was described by Vega[14]. The second pulse duration is calibrated to be approximately 25% of the rotor period, which yields good coherence transfer.

4.3.1 Processing 3Q-MAS Data

Once the data have been successfully acquired, and the time-domain data has been extracted (Figure 4.3), the data can be processed. All of the data processing was performed using Philip Grandinetti's RMN program. The t_2 time-domain data is Fourier transformed first; this is the MAS dimension. The projection of this (now ω_2) should look similar to the 1-dimensional MAS

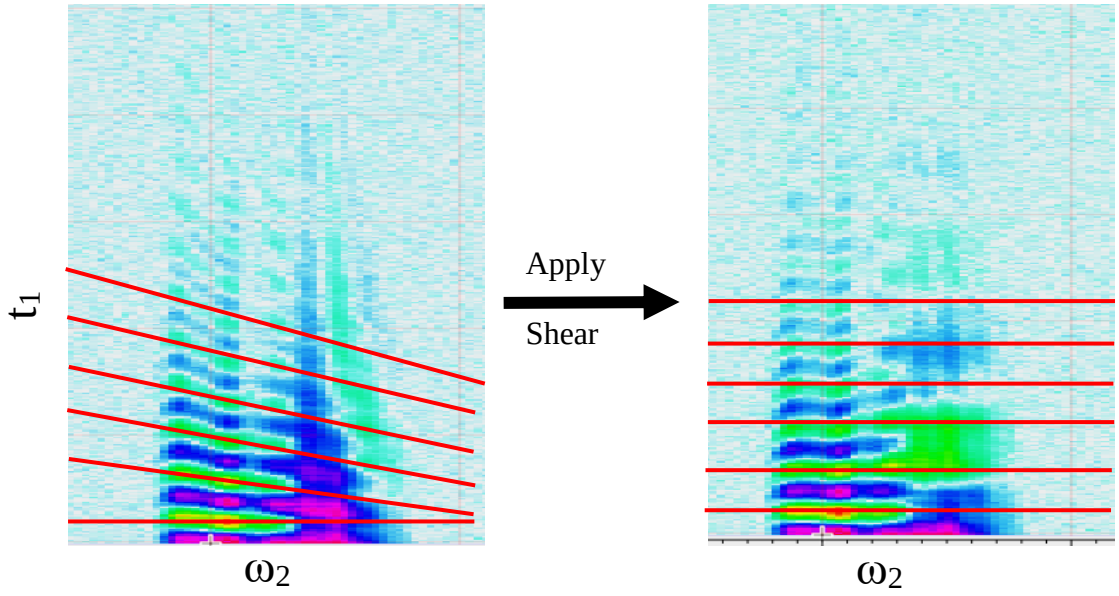

Figure 4.5: Unsheared ^{87}Rb NMR of $RbNO_3$ data is shown on the left, and the result of shearing is shown on the right. The red lines serve as a guide to the eye.

data. The data will have a slight tilt in the t_1 time-domain, which is corrected by applying a shear factor. The shear factor is based on the spin quantum number. For I = 3/2, the shear factor is 7/9 and for I = 5/2, the shear factor is 19/12. ^{87}Rb is a spin-3/2 system, therefore, the data were sheared using the 7/9 shear factor (Figure 4.5).

Now the t_1 dwell time needs to be corrected because of the application of the shear factor. The new t_1 will be denoted at t_1' and is calculated by $t_1' = t_1(1 + 7/9)$, for I = 3/2. For example, if the original t_1 = 16 μs, then t_1' = 28.4 μs. After the dwell has been adjusted, the t_1' time-domain is Fourier transformed, and the processing of 2-dimensional MQ-MAS data is completed, shown in Figure 4.6 (left).

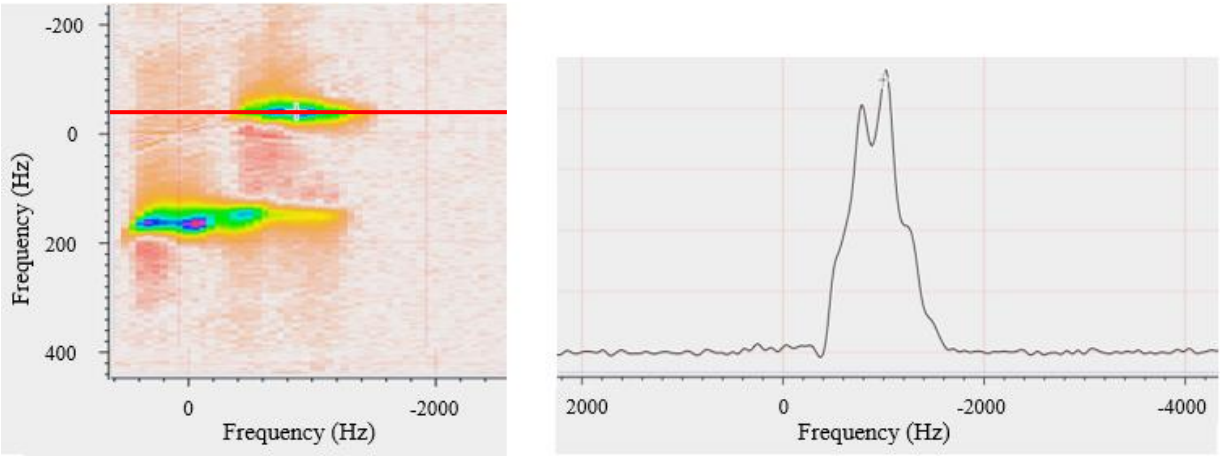

Figure 4.6: On the left is a ^{87}Rb MQ-MAS spectrum. On the right is a 1-dimensional slice of the MQ-MAS data (slice is taken from red line on left).

Finally, extracting 1-dimensional slices from the 2-dimensional data (Figure 4.6) allowed for individual fitting of specific sites. The fitting parameters from these sites could then be used in the quantitative 1-dimensional spectra collected for accurate determination of each site's quadrupolar parameters, critical for deconvolutions.

References

[1] R.E. Wasylishen, S.E. Ashbrook, S. Wimperis, eds., NMR of Quadrupolar Nuclei in Solid Materials, John Wiley and Sons, Ltd, West Sussex, 2012.

[2] A. Llor, J. Virlet, TOWARDS HIGH-RESOLUTION NMR OF MORE NUCLEI IN SOLIDS: SAMPLE SPINNING WITH TIME-DEPENDENT SPINNER AXIS ANGLE, Chem. Phys. Lett. 152 (1988) 248–253.

[3] B.F. Chmelka, K.T. Mueller, A. Pines, J. Stebbins, Y. Wu, J.W. Zwanziger, Oxygen-17 NMR in solids by dynamic-angle spinning and double rotation, Nature. 339 (1989) 42–43. doi:10.1038/339042a0.

[4] K.. Mueller, B.. Sun, G.. Chingas, J.. Zwanziger, T. Terao, A. Pines, Dynamic-angle spinning of quadrupolar nuclei, J. Magn. Reson. 86 (1990) 470–487. doi:10.1016/0022-2364(90)90025-5.

[5] K.T. Mueller, Y. Wu, B.F. Chmelka, J. Stebbins, A. Pines, High-resolution oxygen-17 NMR of solid silicates, J. Am. Chem. Soc. 113 (1991) 32–38. doi:10.1021/ja00001a006.

[6] A. Samoson, E. Lippmaa, A. Pines, High resolution solid-state N.M.R., Mol. Phys. 65 (1988) 1013–1018. doi:10.1080/00268978800101571.

[7] L. Frydman, J.S. Harwood, Isotropic Spectra of Half-Integer Quadrupolar Spins from Bidimensional Magic-Angle Spinning NMR, J. Am. Chem. Soc. 117 (1995) 5367–5368. doi:10.1021/ja00124a023.

[8] J.-P. Amoureux, C. Fernandez, S. Steuernagel, Z Filtering in MQMAS NMR, J. Magn. Reson. Ser. A. 123 (1996) 116–118. doi:10.1006/jmra.1996.0221.

[9] D. Massiot, B. Touzo, D. Trumeau, J.P. Coutures, J. Virlet, P. Florian, P.J. Grandinetti, Two-dimensional magic-angle spinning isotropic reconstruction sequences for quadrupolar nuclei, Solid State Nucl. Magn. Reson. 6 (1996) 73–83. doi:10.1016/0926-2040(95)01210-9.

[10] A. Wokaun, R.R. Ernst, Selective Detection of Multiple Quantum Transitions in NMR by Two-Dimensional Spectroscopy, Chem. Phys. Lett. 52 (1977) 407–412.

[11] G. Drobny, A. Pines, S. Sinton, D.P. Weitekamp, D. Wemmer, Fourier transform multiple quantum nuclear magnetic resonance, Faraday Symp. Chem. Soc. 13 (1978) 49–55. doi:10.1039/fs9781300049.

[12] J.P. Amoureux, M. Pruski, D.P. Lang, C. Fernandez, The Effect of RF Power and Spinning Speed on MQMAS NMR, J. Magn. Reson. 131 (1998) 170–175. doi:10.1006/jmre.1997.1275.

[13] G. Wu, D. Rovnyak, R.G. Griffin, Quantitative Multiple-Quantum Magic-Angle-Spinning NMR Spectroscopy of Quadrupolar Nuclei in Solids, J. Am. Chem. Soc. 118 (1996) 9326–9332. doi:10.1021/JA9614676.

[14] A.J. Vega, MAS NMR spin locking of half-integer quadrupolar nuclei, J. Magn. Reson. 96 (1992) 50–68. doi:10.1016/0022-2364(92)90287-H.

Chapter 5: Future Directions

5.1 Future Directions

The utility of NMR proves itself time and time again for a wide range of applications, such as (but not limited to) diffusion, dynamics, structural characterization, and imaging. Additionally, a basic understanding of the information to be gained from static or MAS experiments is important to understanding certain dynamics. These experiments were made possible by the use of special cryogenic equipment along with high magnetic fields.

Understanding CO_2 dynamics in the MOF-74 system lead us to a better understanding of how CO_2 organizes itself within the channels as a function of CO_2 loading, described by the second Legendre Polynomial, P_2. This understanding could possibly translate to similar CO_2 loading vs P_2 plots for other MOF systems used for CO_2 capture, and how pore size might play a crucial role in the adsorption characteristics. Other aspects to be investigated include the study of competitive binding between CO_2 and an additional guest molecule in a porous framework, or how CO_2 interacts with its porous host in the presence of a non-interacting inert gas, such as N_2 since N_2 is a large component of flue gas as well.

Extracting accurate parameters for the aluminum sites in aluminum carbide and the discovery of oxycarbides is crucial to accurately deconvolute other complicated spectra, such as the aluminum carbide-derived MIL-53(Al) materials. Similar to the MIL-53(Al) deconvolution, having accurate quadrupolar tensors for the two aluminum sites can be important for deconvolution of more complex lineshapes that have overlapping resonances. Knowing about impurities in aluminum carbide is important for syntheses that require high purity starting materials.

MQ-MAS has been around since the mid-nineties, and employed by many labs around the world to characterized a multitude of samples. However, there has not been a guide to discuss how to setup and optimized the MQ-MAS experiment. The ^{87}Rb NMR of $RbNO_3$ is a good standard sample for optimizing a spin-3/2 system, as discussed in this thesis. However, spin systems with larger half-integer spin quantum numbers (spin-5/2 and larger) are also very important. Having a fundamental guide that explains the experimental parameters to optimize these larger spin systems (spin-5/2 and larger) is a field of interest to many people and will benefit researchers across the globe. There is more that can be explored for optimizing the efficiency of the non-selective, high powered, pulses for excitation and conversion of the triple-quantum coherences.

ROBERT M. MARTI

Graduate Student Researcher Phone: (314) 565-5576
Department of Chemistry, Washington University in St. Louis
1 Brookings Drive, Campus Box 1134 E-mail: RMarti0615@gmail.com
St. Louis, Missouri 63130

Professional Positions

2018- Research Chemist – Specialty Coatings and Materials, PPG Industries, Inc.

2013-2018 Graduate student researcher, Washington Univ.

2010-2013 Resident Advisor, Westminster College

Education

2018 Ph. D., Chemistry, Washington University in St. Louis with Prof. Sophia E. Hayes. Thesis title: *An NMR Study of CO_2 Dynamics and Structural Characterization of Porous Materials*

2013 B.A., Chemistry and Mathematics, Westminster College

Awards and Honors

2018 Winner of Graduate Student Symposium competition (3rd place)

2017 Student and Post-Doctorate Team Science Award

Research Interests

Development and implementation of specialized NMR hardware to execute studies relevant to carbon dioxide capture materials. Experimental apparatuses include glassware and probes that allow for convenient variable gas loadings, including mixed gases. Additional setups for variable temperature NMR from 8 – 450 K for dynamics studies.

Solid-state NMR of quadrupolar nuclei in materials, such as metal-organic frameworks (MOFs), engineered for carbon dioxide capture. Elucidation of structural motifs yields insight to the functionality of the system. Many quadrupolar systems are dominated by second-order quadrupolar broadening, which encodes information about local structure for some crystalline materials.

Publications (* indicates corresponding author)

8. Wilson, Brendan; **Marti, Robert M.**; Sun, He; Hayes, Sophia E.; *Grandinetti, Philip J. "A Student's Guide to MQ-MAS of Quadrupolar Nuclei in Solids" In Preparation
7. **Marti, Robert M.**; Moran, Colton M.; Joshi, Jayraj N.; Walton, Krista S.; *Hayes, Sophia E. "Insight to MIL-53 Synthesis with ^{27}Al NMR" In Preparation
6. **Marti, Robert M.**; Sarou-Kanian, Vincent; Moran, Colton M.; Walton, Krista S.; *Hayes, Sophia E. "MQ-MAS NMR Reveals Quadrupolar Tensors and Impurities of Aluminum Carbide" In Preparation

5. Moran, Colton M.; **Marti, Robert M.**; Hayes, Sophia E.; *Walton, Krista S. "Tunable Nanoparticles in Aluminum Carbide-Derived Carbon for Enhanced Acid Gas Adsorption" In Preparation
4. Moran, Colton M.; Joshi, Jayraj N.; **Marti, Robert M.**; Hayes, Sophia E.; *Walton, Krista S. "Structured Growth of Metal-Organic Framework MIL-53(Al) from Solid Aluminum Carbide Precursor" *J. Am. Chem. Soc.* **2018** *140,* 9148-9153. DOI: 10.1021/jacs.8b04369
3. Moore, Jeremy, K.; **Marti, Robert M.**; Guiver, Michael D.; Du, Naiying; Conradi, Mark S.; *Hayes, Sophia E. "CO_2 Adsorption on PIMs Studied with ^{13}C NMR Spectroscopy" *J. Phys. Chem. C* **2018** *122,* 4403-4408. DOI: 10.1021/acs.jpcc.7b12312
2. **Marti, Robert M.**; Howe, Joshua D.; Morelock, Cody R.; Conradi, Mark S.; Walton, Krista S.; Sholl, David S.; *Hayes, Sophia E. "CO_2 Dynamics in Pure and Mixed-Metal MOFs with Open Metal Sites" *J. Phys. Chem. C* **2017** *121,* 25778-25787. DOI: 10.1021/acs.jpcc.7b07179
   Cover art, https://pubs.acs.org/toc/jpccck/121/46
1. Moran, Colton M.; **Marti, Robert M.**; Hayes, Sophia E.; *Walton, Krista S. "Synthesis and characterization of aluminum carbide-derived carbon with residual aluminum-based nanoparticles" *Carbon* **2017** *114,* 482-495. DOI: 10.1016/j.carbon.2016.11.083

Posters/Presentations

7. Experimental NMR Conference, Orlando, FL, May 2018, "Carbon Dioxide Capture Materials and Dynamics" **(poster)**
6. Graduate Student Symposium, Saint Louis, MO (Washington University in St. Louis), February 2018, "CO_2 Adsorption in MOF-74 and Characterization of MIL-53(Al) from Aluminum Carbide" **(poster)**
5. Missouri Inorganic Day, Saint Louis, MO (Saint Louis University), May 2017, "CO_2 Dynamics in Pure and Mixed-Metal MOFs with Open Metal Sites" **(talk)**
4. EFRC-Hub-CMS PI Meeting, Washington, D.C. (Department of Energy), July 2017, "Understanding Structure and Dynamics of CO_2 Adsorbed in Open-Site Metal-Organic Frameworks" **(talk)**
3. 10^{th} Alpine Conference on Solid-state NMR, Chamonix, France, September 2017, "CO_2 Dynamics in Pure and Mixed-Metal MOFs with Open Metal Sites" **(round table discussion)**
2. Chicago Area NMR Discussion Group, Lake Forest, IL (Pfizer), November 2017, "CO_2 Dynamics in Pure and Mixed-Metal MOFs with Open Metal Sites" **(talk)**
1. 58^{th} Annual Rocky Mountain Conference on Magnetic Resonance, Breckenridge, CO, July 2016, "Solid-state NMR as a Probe for CO_2 Dynamics in Metal-Organic Framework (MOF) Materials and Characterization of Aluminum Carbide-Derived Carbons" **(poster)**

Teaching Assistance Experience

***Chemistry 111,* General Chemistry I:** Taught three recitation sections every week focused on recent topics taught in the course, enrollment of 20-30.

***Chemistry 151,* General Chemistry Lab II:** Taught one section of chemistry laboratory per week, which focused on developing scientific skills, enrollment of 16-20.